Low Energy Ion-Surface Interaction and Epitaxial Growth in the SiGe System

Thesis by

Cho-Jen Tsai

In Partial Fulfillment of the Requirements

for the Degree of

Doctor of Philosophy

California Institute of Technology

Pasadena, California

1992

(Submitted April, 1992)

Acknowledgments

During my five years of graduate study, I have benefited from the excellent scientific environment at Caltech. Of course, the most important element of a scientific environment is the people in it. Upon all these people, I would like to express my deep gratitude to Professor H.A. Atwater whose advice and support of my research are extremely valuable and crucial to the finishing of this thesis. The tireless pursuit of scientific knowledge by Dr. Atwater also inspired me to broaden my view in science, which is a priceless lesson. I am equally indebted to Professor T. Vreeland, Jr., from whom I learned both the real spirit of research and life. The encouragement from Prof. Vreeland also played an essential role in establishing my confidence in independent research.

I would also like to thank professor M.-A. Nicolet who supported me in my early graduate study and introduced me to Rutherford backscattering spectroscopy. I also appreciated the opportunity to interact with Dr. A. Dommann in the early stages of construction of the high-resolution X-ray diffractometer in Keck 222 which was delightful and fruitful in both social and scientific aspects. Special thanks to Dr. A. Mutz who helped me in many aspects of my graduate study and gave me many useful suggestions, Dr. S. Nikzard for many helpful discussions and previewing this thesis, and Dr. B. Nielsen at Brookhaven National Laboratory for performing positron annihilation measurements on some of my samples. I also benefited from the courses taught by Professor W.L. Johnson and Professor B. Fultz.

I am grateful to have had the chance to meet the following persons, Dr. B. Kruger, Dr. C. Ahn, Dr. F. Xiong, Dr. G. Bai, Dr. J. Im, Dr. B. Park, C. Garland, R. Murty, J.S. Chen, J. Yang, J. Shin, I. Hashin, S. Wong, D. Lie, W.S. Liu and L. Lowry at JPL, who have also provided help in one way or another and friendship. Finally, I would like to mention the support of my family which is the most important driving force for me in pursuing graduate study.

Abstract

The structure of a growing epitaxial film is controlled by the relative rate of different surface processes. Low energy ion beams (50-500 eV) can be used to provide energy to adatoms on the surface and atoms in the near-surface region of a growing film. Thus, a low energy ion beam can be employed as a tool to modify surface kinetics. The study of the effects of the beam-induced defects on the epitaxial growth can also provide valuable insights into intrinsic growth processes by altering the relative rate of various surface kinetics. The work contained in this thesis is focused on the role of defects produced by low energy ion bombardment in modification of epitaxial growth of Si, Ge, and SiGe alloy films.

In the first two chapters, theoretical and technical aspects of X-ray rocking curve diffractometry which is one of the principal analytic methods used in this thesis is discussed. The high-resolution X-ray diffractometer built at Caltech and the dynamical theory of X-ray diffraction are briefly discussed. The last four chapters are focused on the manner in which low energy ion beam bombardment affect the structural properties and growth kinetics of epitaxial films. One of the most important factors determining the changes that occur in ion-assisted epitaxy is the ion energy used to stimulate the growth processes, which determines the relative number of surface displacements and bulk displacements. The effect of bulk displacement defects on an epitaxial film structure is discussed in Chapter 3. In Chapter 4, a simple moving boundary diffusion model in conjunction with thermal spike activated kinetics is presented to describe the bulk defect incorporation process. The moving boundary diffusion model has also been used to describe the adatom concentration on the vicinal Si surface and the low energy dopant incorporation processes. Surface displacements produced by low energy ion bombardment has a dramatic effect on the growth mode of epitaxial Ge films on Si(100); this is the main theme of Chapter 5. In the initial stages of Ge growth on Si, a layer-by-layer growth followed by island growth was observed in conventional (thermal) molecular beam epitaxial growth. Island formation

is inhibited by low energy ion bombardment during epitaxial growth which can prolong the layer-by-layer growth mode to greater thicknesses than for thermal growth. In Chapter 6, the effect of the low energy ion bombardment on the misfit accommodation of the lattice mismatched system is discussed. The point defects injected by the low energy ion bombardment impede dislocation motion in the growing epitaxial film and cause misfit strain to be accommodated by the threading dislocations which greatly enhances the misorientation between a film and its substrate.

Contents

List of Figures

List of Tables

List of Publications

Parts of this thesis have been, or will be published under the following titles:

1) T. Vreeland, A. Dommann, C.J. Tsai, and M.A. Nicolet; "X-ray Determination of Stresses in Thin Films"; Mat. Res. Soc. Symp. Proc. **130**, 3 (1989).

2) C.J. Tsai, H.A. Atwater, and T. Vreeland; "Strain Modification in Coherent Ge and Si_xGe_{1-x} Epitaxial Films by Ion-Assisted Molecular Beam Epitaxy"; Appl. Phys. Lett. **57**, 2305 (1990).

3) C.J. Tsai, A. Dommann, M.A. Nicolet, and T. Vreeland; "Self-Consistent Determination of the Perpendicular Strain Profile of Implanted Si by Analysis of X-ray Rocking Curves"; J. Appl. Phys. **69**, 2076 (1991).

4) C.J. Tsai, P. Rozenak, H.A. Atwater, and T. Vreeland; "Strain Modification by Ion-Assisted Molecular Beam Epitaxy in the Si_xGe_{1-x} Alloy System : a Kinetic Analysis"; J. Crystal growth **111**, 931 (1991).

5) C. J. Tsai, H.A. Atwater, and T. Vreeland; "Strain Modification and Thermal Stability of Si_xGe_{1-x} Films Grown by Ion-Assisted Molecular Beam Epitaxy"; Mat. Res. Soc. Sym. Proc., **201**, 57, 1990.

6) C.J. Tsai, T. Vreeland, and H.A. Atwater; "Defect Formation and Diffusion Mechanism in Ion-Assisted Molecular Beam Epitaxy"; submitted to Phys. Rev. B., Nov. 1991.

7) C.J. Tsai and H.A. Atwater; "Kinetic Inhibition of Island Formation during Ge Epitaxy on Si (001)"; in preparation.

8) C.J. Tsai, T. Vreeland, Jr., and H.A. Atwater; " Misorientation of Ge Epitaxial Films on Si (001) Grown by Ion-Assisted Molecular Beam Epitaxy"; in preparation.

9) C.J. Tsai, T. Vreeland, Jr., and H.A. Atwater; "Strain Measurements of Low Energy Ion Beam Sputtered Si (001) by X-ray Interference"; in preparation.

Chapter 1
X-Ray Rocking Curve Theory and Setup

1.1 Introduction

In the early 19th century, a delightful discovery was made of an unknown light that could see through an "opaque" object. The light was named "X-ray". Since its discovery, scientists have used it to study "opaque" objects and its usefulness has expanded in many scientific fields. Diffraction is one of the most important methods in X-ray applications for characterizing crystal structure, imperfections, and deformations of materials.

In the 1970's, the double crystal X-ray rocking curve (XRC) diffractometry was developed and put into practices. In the 1980's, extensive use was made of XRC diffractometry for studies of strain and damage profiles in ion-implanted crystals, epitaxial layers, and superlattices [1-7]. The term "double crystal" implies that the system contains two crystals : (i) a monochromating crystal and (ii) a sample crystal to be analyzed. The monochromating crystal is a high quality single crystal semiconductor substrate,(e.g., Si or GaAs wafer). The chromatic selection of the K_α line of an X-ray source is achieved by diffraction from the crystal monochromator. The procedure yields a beam made up of the two wavelengths of the K_α doublet, $K_{\alpha 1}$ and $K_{\alpha 2}$. Because of the slight difference in wavelengths between $K_{\alpha 1}$ and $K_{\alpha 2}$, there is a small difference in the Bragg angles corresponding for these two wavelengths. A slit is used to take advantage of the small difference in the Bragg angles to cut off the $K_{\alpha 2}$ line. A more detailed description of the double crystal X-ray diffractometer can be found in ref. [7, 8]. Due to the simplicity of the theoretical analysis [2, 9] and the experimental setup, XRC became one of the most important non-destructive tools in characterizing epitaxial thin films. However, the limitation of double crystal XRC diffractometry is that sharp diffraction peaks of the samples can only occur when the Bragg angle of the sample crystal is close to the Bragg angle of the monochromating crystal. As early as 1943, DuMond [10] had already discussed this issue and suggested that a monochromator consisting of four identical crystals could be used to overcome this problem. It was only in 1983 that Bartels [11] re-addressed this issue and used a four-crystal monochromator diffractometer to analyze epitaxial films. The X-ray diffractometer with a four-crystal monochromator was called a high resolution X-ray diffractometer.

In the following, we will discuss the dynamical theory of X-ray diffraction which is the basis for the analysis of the XRC diffraction data as well as the multi-purpose high resolution X-ray diffractometer built at Caltech. The applications of XRC will be discussed in the next chapter.

1.2 Multi-purpose High Resolution X-ray Diffractometer

A typical X-ray diffractometer setup for rocking curve measurements has been briefly discussed by Vreeland et al., [7, 8]. The major parts of the system consist of (i) an X-ray source, (ii) a monochromator, (iii) slits between the monochromator and the sample, (iv) the goniometer, (v) X-ray detector, and (vi) computer control system. Figure 1.1 shows the schematic arrangement of the high-resolution X-ray diffractometer that was built at Caltech. Here, we focus on the major differences between a double crystal XRC diffractometer system and a high resolution XRC diffractometer system, i.e., the monochromator, and goniometer. The schematic diagram of the electrical connection of the high resolution XRC diffractometer system built at Caltech is briefly described in the appendix A.

1.2.1 X-ray Monochromator

One of the most important features that distinguishes a high resolution XRC system from a double crystal XRC system is the monochromator. In a double crystal XRC system, sharp diffraction peaks from a sample crystal can only be obtained when the Bragg angle, θ_B, of the sample crystal is close to the Bragg angle of the

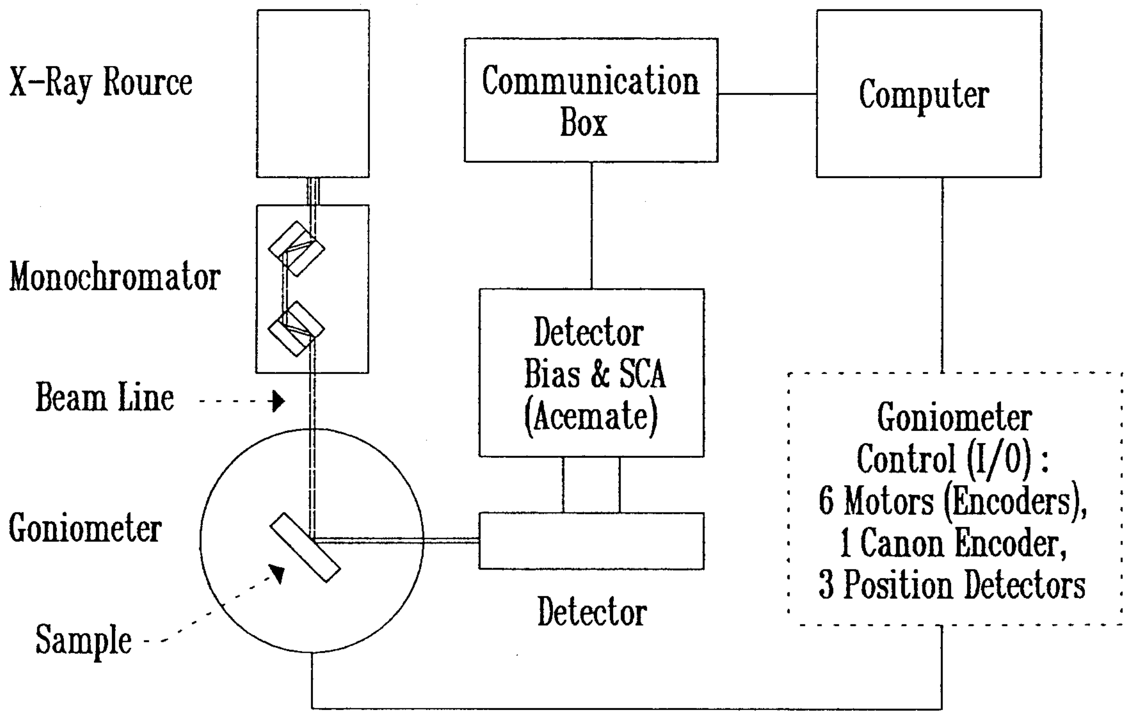

Figure 1.1 Schematic of the high-resolution X-ray diffractometer built at Caltech.

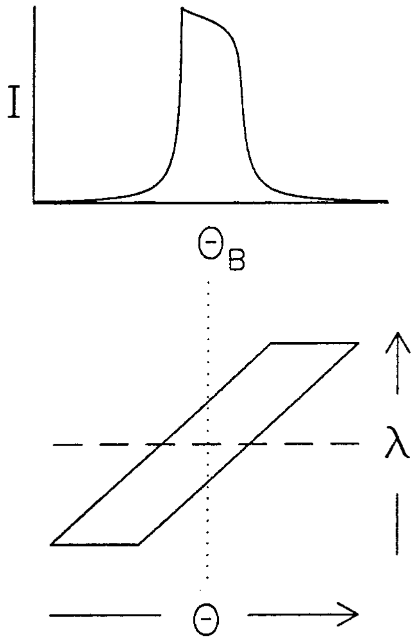

Figure 1.2 Relation between the X-ray wavelength and diffraction angle. For an ideal X-ray source, the diffraction spectrum shown at the upper part of the figure can be calculated with the dynamical theory of X-ray diffraction. For a finite divergence of the source, the beam profile is represented by the intensity band at the lower part of the figure.

single crystal monochromator, while a multiple crystals monochromator will allow sharp diffraction peaks to occur at any Bragg angle. We use the diagram proposed by DuMond [10] to illustrate this point. Consider an ideal X-ray source with a single X-ray wavelength, λ. After Bragg diffraction from a single crystal, we find that the intensity profile is actually narrow but of finite width as calculated from the dynamical theory of X-ray diffraction. Now if we include the finite wavelength spread of the X-ray source, we can represent the relation between the X-ray wavelength and diffraction angle as a band shown in Fig. 1.2. When a sample crystal is analyzed, we construct another intensity band to represent the diffraction intensity profile and slide this intensity band through the first band representing the monochromator crystal to find the diffraction profile. Figure 1.3 shows two geometries of a sample crystal, in (+ +) and (+ -) settings with respect to the monochromator crystal and the corresponding intensity bands to obtain a diffraction profile. It is clear that the final

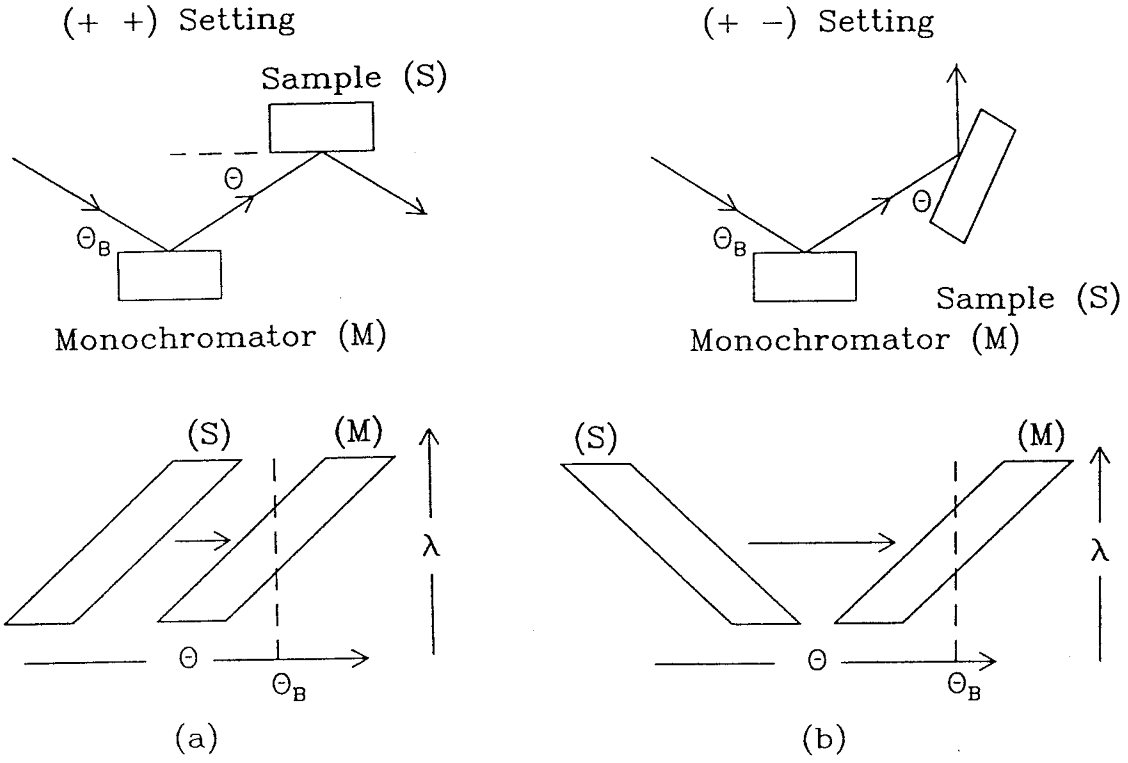

Figure 1.3 Two geometries for a sample crystal, in (a) (+ +) and (b) (+ -) settings with respect to the monochromator crystal and the corresponding intensity bands to obtain a diffraction profile.

intensity profile is insensitive to the wavelength spread only when the Bragg angle of the sample crystal is close to that of the monochromator crystal and the two diffraction planes are parallel to each other (+ +).

A four-crystal monochromator can be represented by two crossed intensity bands shown in Fig. 1.4 which further eliminates the wavelength spread and the angular spread of the X-ray source, at the expense of a reduced final beam intensity. Each intensity band represents a set of crystals in parallel position. The advantage of a four-crystal monochromator is that the resulting intensity profile which is represented by the cross-hatched area in Fig. 1.4 is almost symmetric in angular space, which will allow absolute lattice constant measurements using the Bond method [12] because sharp diffraction peaks can be obtained in both settings of a sample crystal.

Figure 1.5 shows two dynamical calculations of the intrinsic broadening of (022) diffraction peaks for Si and Ge (which will be discussed in the next section). Since the (022) diffraction peak of Si is sharper than that of Ge, the arrangement of one channel cut Si crystal and one channel cut Ge crystal was used, a compromise of the intensity for sharpness of the final beam profile.

1.2.2 Goniometer

The versatility of the high-resolution XRC system built at Caltech is enabled by the independent degrees of freedom of movement in sample goniometer which is controlled by five D.C. motors. Figure 1.6 shows four of the movements of the motors which control the goniometer. In addition, the θ motion (rotation about z axis) is controlled by a microstepping motor, and a D.C. motor controls the detector position (2θ). The θ position is read by a laser rotary encoder combined with an encoder interpolator which is directly mounted to the main rotary stage rather than to the θ motor, thus eliminating the angular uncertainties produced by motor backlash. The independent control of the θ and 2θ motors allows asymmetric diffraction to be taken. The side-translation motor (translation along y axis) can be used to determine the

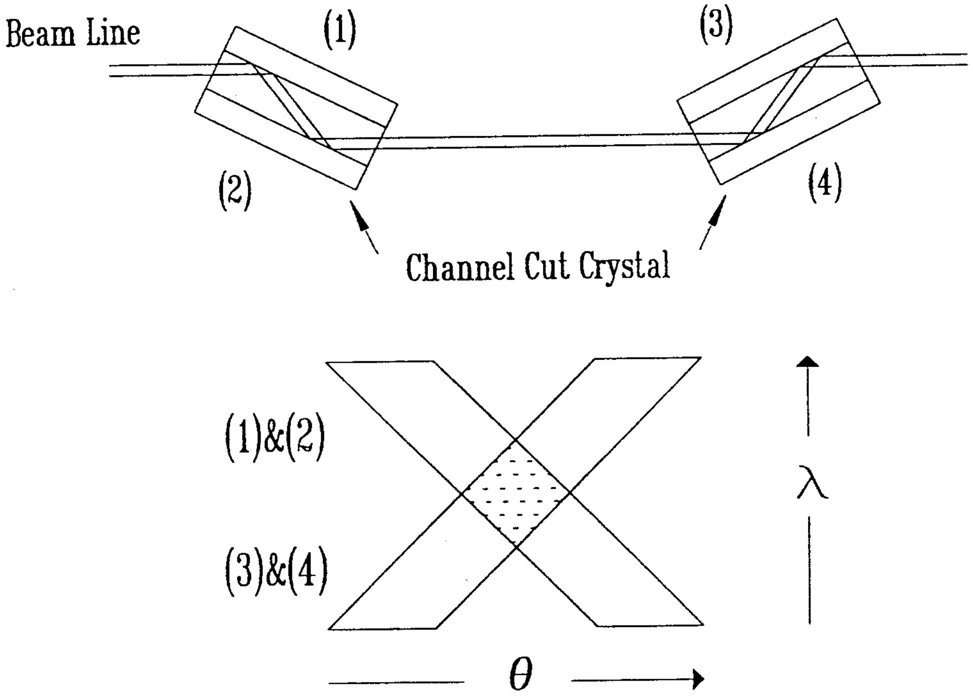

Figure 1.4 A four-crystal monochromator and the resulting beam profile which is represented by the cross-hatched area.

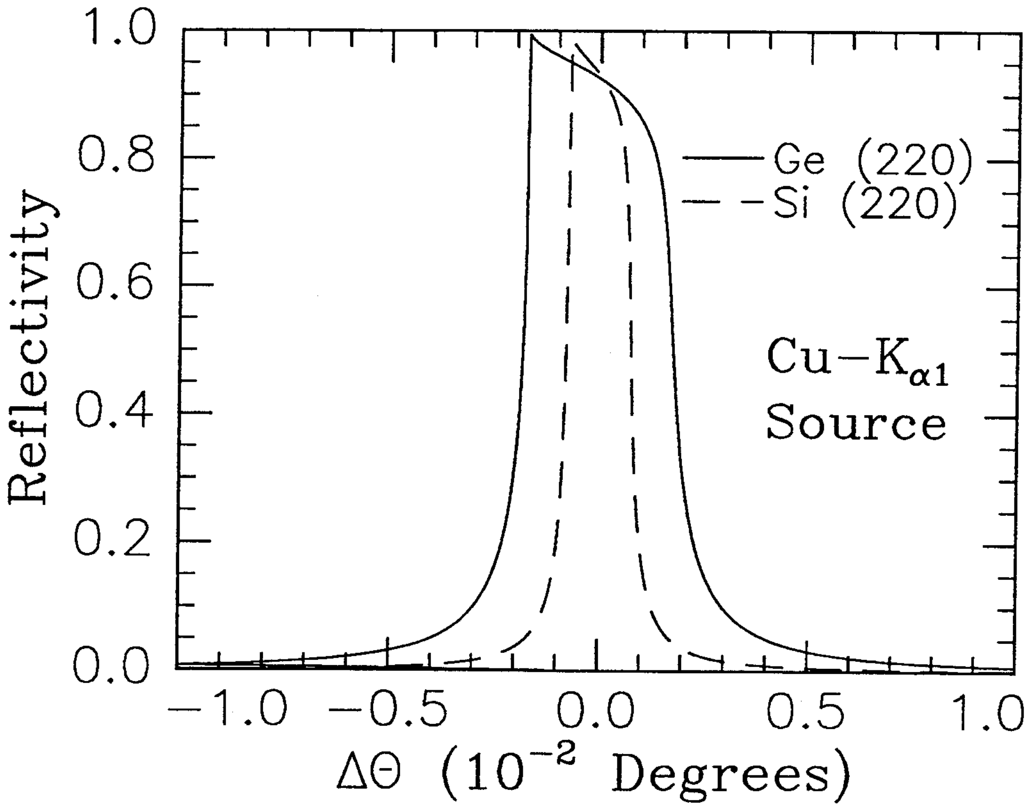

Figure 1.5 The intrinsic broadening of (022) diffraction peaks for Si and Ge calculated using dynamical theory of X-ray diffraction.

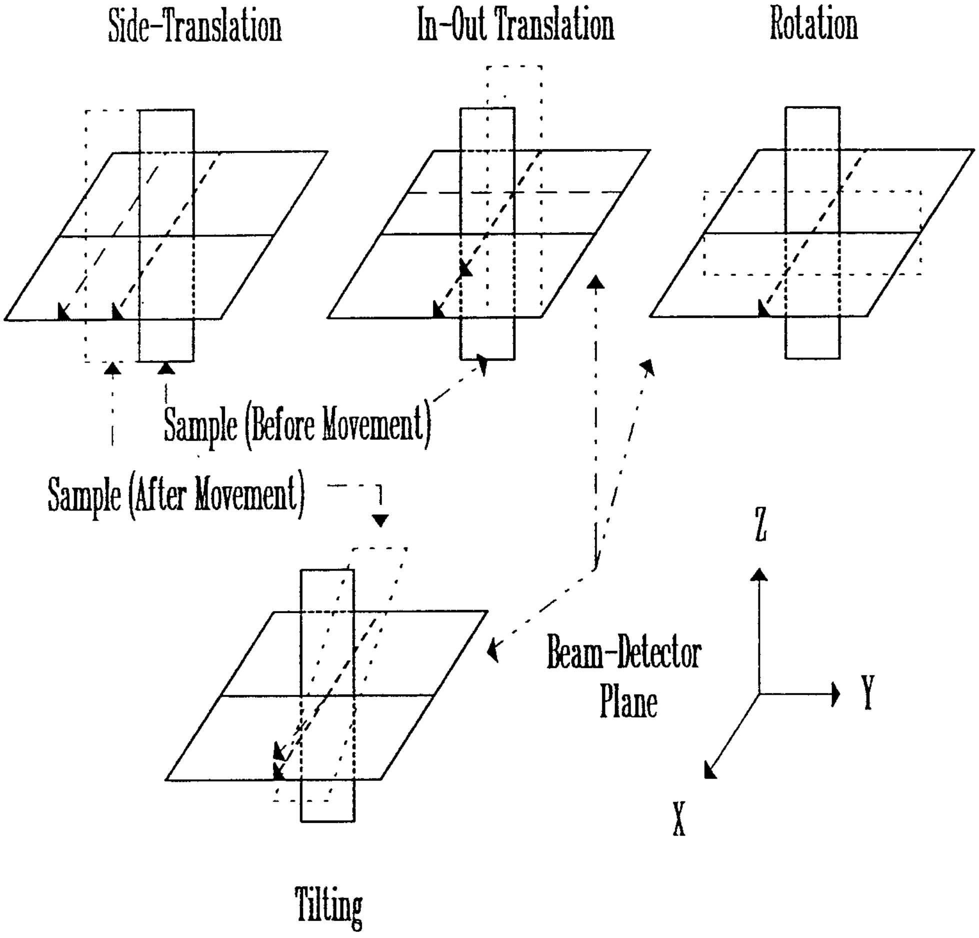

Figure 1.6 Four of the movements available in the XRC diffractometer goniometer built at Caltech.

overall curvature of a single crystal wafer. The rotation motor (rotation about x axis) can be used to measure the misorientation between an epitaxial film and its substrate. The combination of rotation and tilting motor (rotation about y) can be used to present an asymmetric diffraction plane normal to the beam-detector plane.

1.3 Dynamical Theory of X-ray Diffraction

The two principal X-ray scattering theories used in XRC are the kinematical theory and the dynamical theory. Generally speaking, the kinematical theory neglects the absorption and extinction effects and has the advantage of less computing time, while the dynamical theory, which takes into account absorption and extinction of a plane wave field in a crystal, is more rigorous than the kinematical theory. However, there are certain situations for which the dynamical theory is necessary : (i) when the thickness of the epitaxial film is sufficiently thick so that the X-ray absorption can no longer be neglected, and (ii) when the interference of the wave fields between an epitaxial film and its substrate is important (which will be discussed in the next chapter). Descriptions of the dynamical theory of X-ray diffraction can be found in the texts written by W.H. Zachariasen [13] and by R.W. James [14]. We briefly follow the simpler phenomenological description (optical approach) of the theory developed by Darwin [15] and modified by Prins [16] in ref. [14] and show that the results derived from the optical approach are the same as the dynamical theory developed in terms of a continuous charge distribution [9, 13]. We concentrate only on the symmetric diffraction case for the following exposition.

The complex amplitude, q_H, of a wave reflected by an infinite plane sheet of atoms from the Fresnel construction (normalized to the amplitude of the incident wave) is given by

$$-iq_H = +iNaf(H)\frac{\lambda}{sin\theta}\frac{e^2}{mc^2}, \tag{1}$$

where N is the number of atoms per unit volume, a is the distance between two successive planes, $f(H)$ is the atomic scattering factor of an atom in the direction of

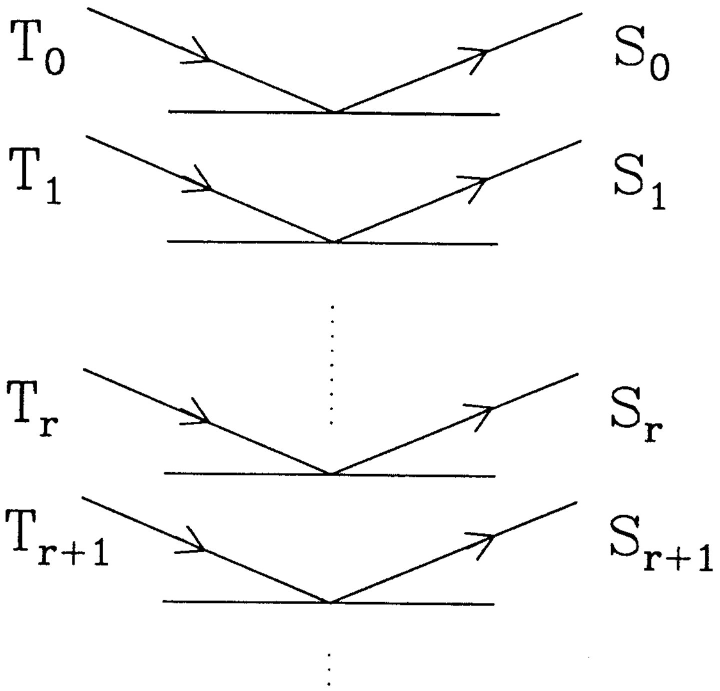

Figure 1.7 Definition of transmitted and reflected amplitude. The incident beam amplitude is T_0 and the final reflected beam amplitude is S_0.

the reflected wave, θ is the incident angle, and e^2/mc^2 is the classical electron radius. Similarly, the amplitude of a transmitted wave , q_0 is written as

$$-iq_0 = +iNaf(0)\frac{\lambda}{sin\theta}\frac{e^2}{mc^2}, \tag{2}$$

where $f(0)$, is the atomic scattering factor in the direction of the incident wave. Now consider an array of N lattice planes shown in Fig. 1.7. The parameters T_r and S_r represent respectively the incident and reflected wave at the rth plane. By matching the boundary conditions at each plane, we obtain the following equations

$$\begin{aligned} S_r &= -iq_H T_r + (1 - iq_0)e^{-i\phi}S_{r+1} \\ T_{r+1} &= (1 - iq_0)e^{-i\phi}T_r - iq_H^{'}e^{-2i\phi}S_{r+1}, \end{aligned} \tag{3}$$

where $q_H^{'} = q_{-H}$ is the reflection coefficient from the lower side of the plane, and $\phi = 2\pi asin\theta/\lambda$ is the phase difference for two successive planes with incident beam angle θ. The coupled equations can be written in matrix form

$$\begin{pmatrix} S_0 \\ T_0 \end{pmatrix} = \frac{1}{1-iq_0} \begin{pmatrix} [(1-iq_0)^2 + q_H q_H^{'}]e^{-i\phi} & iq_H e^{i\phi} \\ iq_H^{'} e^{-i\phi} & e^{i\phi}) \end{pmatrix} \begin{pmatrix} S_r \\ T_r \end{pmatrix}. \tag{4}$$

In the limit of an infinite number of planes, $N \rightarrow \infty$, and neglecting the square of small quantities, the reflectivity in the vicinity of the Bragg angle can be expressed as [14, 17]

$$R_0 = \frac{S_0}{T_0} = \frac{1 + iB/A}{\eta - i\beta/A + \sqrt{(\eta - i\beta/A)^2 - (1 + iB/A)^2}}, \tag{5}$$

where $k = 2\pi/\lambda$, $2asin\theta_B = m\lambda$, $\delta + i\beta = -(q_0 sin\theta_B)/(ka)$, assuming $q_H = q_H^{'}$, $A + iB = -(q_H sin\theta_B)/(ka)$, and $\eta = (-2\delta + sin(2\theta_B)\Delta\theta)/(2A)$. This solution is the same as the solution derived from the dynamical theory in terms of a continuous charge distribution [13, 9] for a perfect semi-infinite crystal.

For layers with a finite thickness,t, the discrete description of Darwin's reflection will introduce errors since eqns. (1) and (2) only account for the scattering and interference at the scattering plane [18]. The discretization error can be eliminated by subdividing a layer into an infinite number of slices and re-calculating the matrix. The procedure changes the discrete description to a description in terms of a continuous charge distribution for Darwin's reflection. The result is [18]

$$L = \begin{pmatrix} cos(sd) + icos(w)sin(sd) & sin(w)sin(sd) \\ -sin(w)sin(sd) & cos(sd) - icos(w)sin(sd) \end{pmatrix}, \tag{6}$$

where

$$\begin{aligned} sin(w) &= i(1 + iB/A)/s \\ cos(w) &= (\eta - i\beta/A)/s \\ s &= \sqrt{(\eta - i\beta/A)^2 - (1 + iB/A)^2} \\ d &= \frac{kAt}{sin\theta_B}. \end{aligned}$$

For a crystal with a lattice constant different from the reference crystal the X-ray strain can be taken into account by replacing $\Delta\theta$ in the expression of η with

$\Delta\theta + tan(\theta_B)\epsilon$ where ϵ is the X-ray strain of the crystal with respect to the reference crystal. Thus for N layers on top of a thick substrate, the reflection and transmission amplitude can be expressed as

$$\begin{pmatrix} S_0 \\ T_0 \end{pmatrix} = L_{(1)}L_{(2)}L_{(3)}\cdots L_{(N)}\begin{pmatrix} R_0 \\ 1 \end{pmatrix}. \tag{7}$$

Since we are only interested in the S_0/T_0, we define the reflected and transmitted complex amplitude to be R_0 and 1 at substrate surface, where R_0 is the solution for a perfect semi-infinite crystal. Hence the quantity S_0/T_0 for a layer with a thickness d on top of a thick substrate can be written in a recursion relation as

$$R' = \frac{sR_0 + i(b + cR_0)tan(sd)}{s - i(c + bR_0)tan(sd)}. \tag{8}$$

For a crystal with a given structure, we modify $Nf(0)$ and $Nf(H)$ to the structure factor per unit volume, $F(0)/V$ and $F(H)/V$. This recursion relation and the solution for an infinite thick substrate are the same as the relations developed from the dynamical theory in terms of a continuous charge distribution, for the symmetric diffraction case discussed in ref. [9, 13] and can be easily extended to the asymmetric diffraction case.

In applying the theory to simulate the X-ray diffraction curves of damaged crystals, a Debye-Waller factor due to the static atomic displacement is introduced. The standard deviation of displacements, u, assuming that the atoms displaced from normal lattice positions follow a spherically symmetric Gaussian distribution in a specific layer reduces the structure factor, F_H, of the undamaged layer to [2]

$$F_H exp\{-(8\pi^2 sin^2\theta_B/\lambda^2)u^2\}. \tag{9}$$

The matrix representation has the advantage of reducing calculating time for superlattice samples. For a superlattice structure with layer types 1 and 2 grown on a substrate of type 3 with the sequence 12121212123 = $(12)^5 3$, we can calculate the (12) structure first, then apply the method developed by Abeles [17, 19]. Thus, for a superlattice structure with N periods and each period consisting of two layers, 1 and 2, the matrix representation can be written as

$$L_{(12)}^{N} = \begin{pmatrix} (P+iQ)Z_N - Z_{N-1} & (T+iU)Z_N \\ (-T+iU)Z_N & (P-iQ)Z_N - Z_{N-1} \end{pmatrix}, \tag{10}$$

where

$$\begin{aligned} P &= cos(s_1d_1)cos(s_2d_2) - sin(s_1d_1)sin(s_2d_2)cos(w_1+w_2) \\ Q &= cos(w_1)sin(s_1d_1)cos(s_2d_2) + cos(w_2)sin(s_2d_2)cos(s_1d_1) \\ T &= cos(s_1d_1)sin(w_2)sin(s_2d_2) + cos(s_2d_2)sin(w_1)sin(s_1d_1) \\ U &= sin(s_1d_1)sin(s_2d_2)sin(w_2-w_1). \\ Z_N &= \sin[N\cos^{-1}P]. \end{aligned}$$

The kinematical theory of X-ray diffraction can be obtained by assigning $B = \beta = 0$ for all the equations above. To illustrate the applicability of the kinematical theory, Figure 1.8 shows the maximum reflectivity as a function of Si(001) film thickness calculating from kinematical and dynamical theory with an (004) diffraction plane and Cu-$K_{\alpha 1}$ wavelength. As the thickness of the film increases, the absorption factor become important. The kinematical theory is a good approximation in the region of $kAt/sin(\theta_B) < 1$ for this specific case. For an asymmetric diffraction, the traveling distance of the wave inside a crystal may increase significantly, the maximum thickness for which kinematical theory will be applicable is reduced quickly. Figure 1.9 shows a typical XRC spectrum and the parameters, strain and static displacements, involved in the spectrum. The diffraction peak shift between a film and its substrate is given by (for $\Delta\theta \ll 1$)

$$\Delta\theta = K_1\epsilon_{\perp} + K_2\epsilon_{||}, \tag{11}$$

where

$$\begin{aligned} K_1 &= \cos^2\phi\tan\theta_B \pm \sin\phi\cos\phi \\ K_2 &= \sin^2\phi\tan\theta_B \mp \sin\phi\cos\phi, \end{aligned}$$

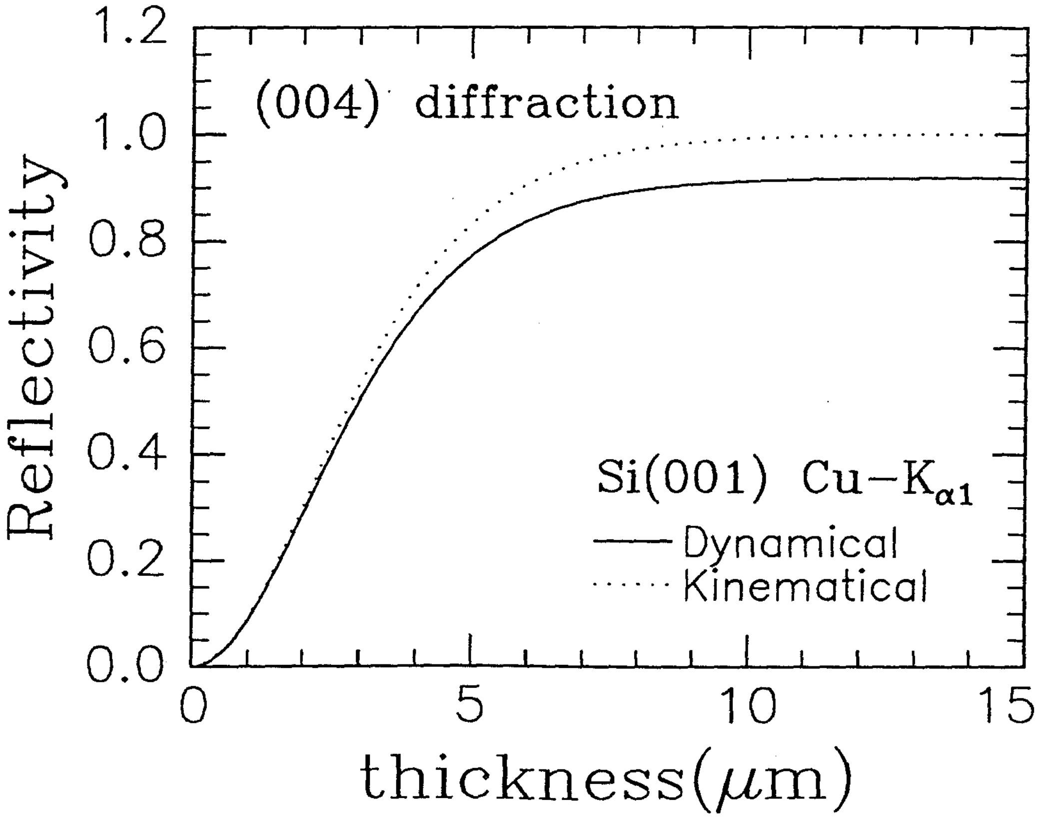

Figure 1.8 The maximum reflectivity as a function of Si(001) film thickness calculating from kinematical and dynamical theory with (004) diffraction plane and Cu-$K_{\alpha 1}$ wavelength.

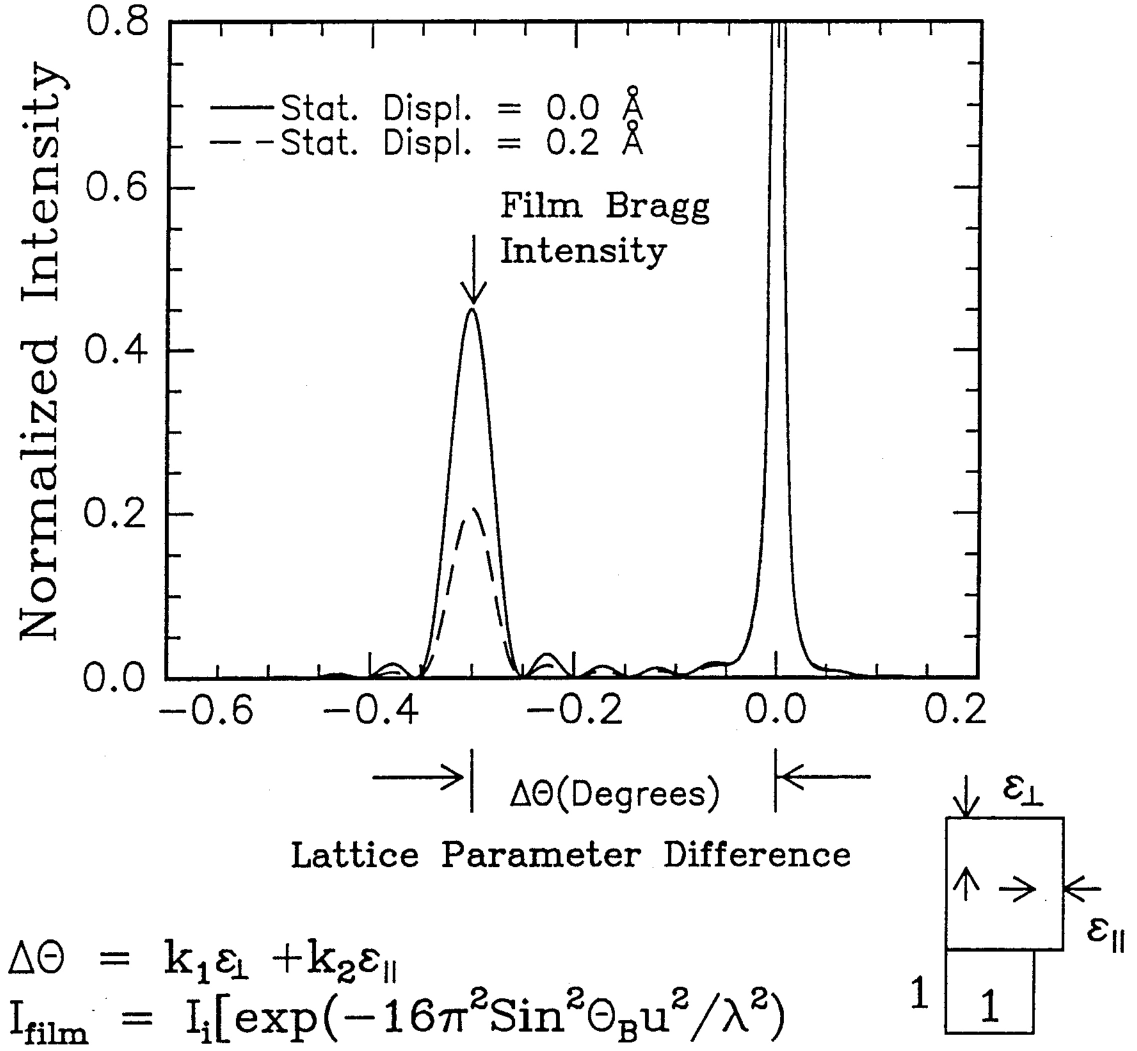

$$\Delta\Theta = k_1\varepsilon_\perp + k_2\varepsilon_\parallel$$

$$I_{film} = I_i[\exp(-16\pi^2 \mathrm{Sin}^2\Theta_B u^2/\lambda^2)$$

Figure 1.9 Illustration of the dependence of the X-ray spectrum on the strain and static displacements.

and ϕ is the angle between the diffraction plane and the sample surface. The upper sign in K_1 and K_2 is for the incident angle of $\theta_B - \phi$ with respect to the sample surface, while the lower sign in the K_1 and K_2 expressions is for the incident angle of $\theta_B + \phi$ with respect to the sample surface. The strain perpendicular to the sample surface is $\epsilon_\perp$ and $\epsilon_{||}$ is strain parallel to the sample surface [6, 9].

References

[1] B.E. MacNeal and V.S. Speriosu, J. Appl. Phys. **52**, 3935 (1981).

[2] V.S. Speriosu, J. Appl. Phys. **52**, 6094 (1981).

[3] B.M. Paine and V.S. Speriosu, J. Appl. Phys. **62**, 1704 (1987).

[4] G.W. Arnold, S.T. Picraux, P.S. Peercy, D.R. Myers, and L.R. Dawson, Appl. Phys. Lett. **45**, 382 (1984).

[5] V.S. Speriosu, M.A. Nicolet, S.T. Picraux, and R.M.Biefeld, Appl. Phys. Lett. **45**, 223 (1984).

[6] V.S. Speriosu and T. Vreeland, Jr., J. Appl. Phys. **56**, 1591 (1984).

[7] T. Vreeland, Jr. and B.M. Paine, J. Vac. Sci. Technol. A **4** 3153 (1986).

[8] T.Vreeland, A. Dommann, C.J. Tsai, and M.-A. Nicolet, Mat. Res. Soc. Symp. Proc. **130**, 3 (1989).

[9] C.R. Wie, T. Tombrello, and T. Vreeland, Jr., J. Appl. Phys. **56**, 1591 (1986).

[10] J.W.M. DuMond, Phys. Rev. **52**, 812 (1937).

[11] W.J. Bartels, J.Vac. Sci. Technol. **B1**, 338 (1983).

[12] W.L. Bond, Acta Cryst. **13**, 814 (1960).

[13] W.H. Zachariasen,"Theory of X-Ray Diffraction in Crystal"; (John Wiley & Sons, Inc., 1945).

[14] R.W. James, "The Optical Principles of the Diffraction of X-ray"; (Cornell University, Ithaca, New York, 1965).

[15] C.G. Darwin, Phil. Mag. **27**, 315 (1914); **27**, 675 (1914).

[16] J.A. Prins, Zeit. f. Physik. **63**, 477 (1930).

[17] R.T. Perkins and L.V. Knight, Acta. Cryst. **A40**, 617 (1984).

[18] M.A. Hollander and B.J. Thijsse, J. Less-Common Metals **140**, 33 (1988).

[19] F. Abeles, Ann. Phys. (Leipsig) **5**, 596 (1950).

Chapter 2
Applications of X-Ray Rocking Curve Diffractometry

2.1 Introduction

The X-ray rocking curve diffractometry has been extensively used to determine strain profiles in heteroepitaxial films and ion-implanted semiconductors. The strain profile in a thin film is determined by matching the experimental X-ray spectrum with the calculation of an assumed profile. The parameters for fitting include thickness, strain, and damage. Thus, it is difficult to verify the uniqueness of the assumed profile with a single XRC measurement. This issue will be discussed in the next section. Aside from the determination of strain using the diffraction peak shift produced by the lattice parameter change (in an epitaxial thin film), the average stress in the plane (for a polycrystalline or amorphous film) can also be determined from the bending of a single crystal caused by this stress (curvature measurement). An example of this application can be found in reference [1]. Since we have not applied this method to the research on the low energy ion-surface interaction during epitaxial growth discussed in this thesis, no further detail will be given here.

For a very thin epitaxial film (0.1-10 nm thickness range), on a typical wafer (substrate) 0.1 mm thick or larger, the diffraction intensity from the film using a XRC system with a low intensity X-ray source (sealed tube) is too small to be detected. In this case, we can use high intensity X-ray source (synchrotron source) to measure the peak shift for a very thin film and find out the strain of the film. Another alternative method for measuring the thickness and strain of very thin films on a typical substrate using a low intensity X-ray source makes use of the X-ray interference effect. However, the X-ray interference requires a reasonably good quality epitaxial layer on top of the very thin film composed of the same material as the layer beneath the very thin film. This constraint restricts the application of the method only to materials for which high quality epitaxial films can be grown. The average strain in a thin layer subject to low energy ion bombardment and the coherency of thin Ge films were studied using this method. Finally, the misorientation between an epitaxial film and its substrate can also be measured using an XRC system.

2.2 Unique Strain Profile Determination of Ion-Implanted Si

The strain sensitivity of the X-ray rocking curve method is limited by the instrument broadening of the diffraction peaks and by broadening due to crystal defects. In cases where the thicknesses of the strained layers are thin so that the kinematical theory of X-ray diffraction is applicable (i.e., absorption can be neglected), the difference between the X-ray rocking curves of two strained layers A and B observed in the stacking order AB and BA is difficult to detect, since the rocking curve can be considered as a simple superposition of the diffraction peaks of the two layers and the substrate peak. In the case when the strained layers are thick so that the dynamical theory of X-ray diffraction should be applied, crystal defects and instrumental broadening may still lead to the same problem. Figure 2.1 shows the two rocking curves for samples with the two layer sequence AB and BA calculated with the dynamical theory for Si(400) diffraction using Fe-$K_{\alpha 1}$ ($\lambda = 0.1936$ nm) incident beam. The calculated rocking curves were convoluted with a Lorentzian function of 6 arcsec full-width half-maximum to account for instrument broadening. In Fig. 2.1(c), we can see only a small difference in the two curves. As the broadening increases, the difference becomes smaller and smaller. Complicated strain profiles such as those of ion-implanted crystals must therefore be carefully analyzed to determine the actual strain profile. Speriosu and co-workers [2] have employed a sequential etching process to assure the correctness of the strain and damage distributions in ion-implanted magnetic bubble materials using X-ray rocking curves and the kinematical theory of X-ray diffraction. Here, a combination of sequential etching, transmission electron microscopy (TEM), and computer simulation (TRIM) is used to determine a unique strain and damage profiles of a 250 KeV Ar$^+$ implanted sample.

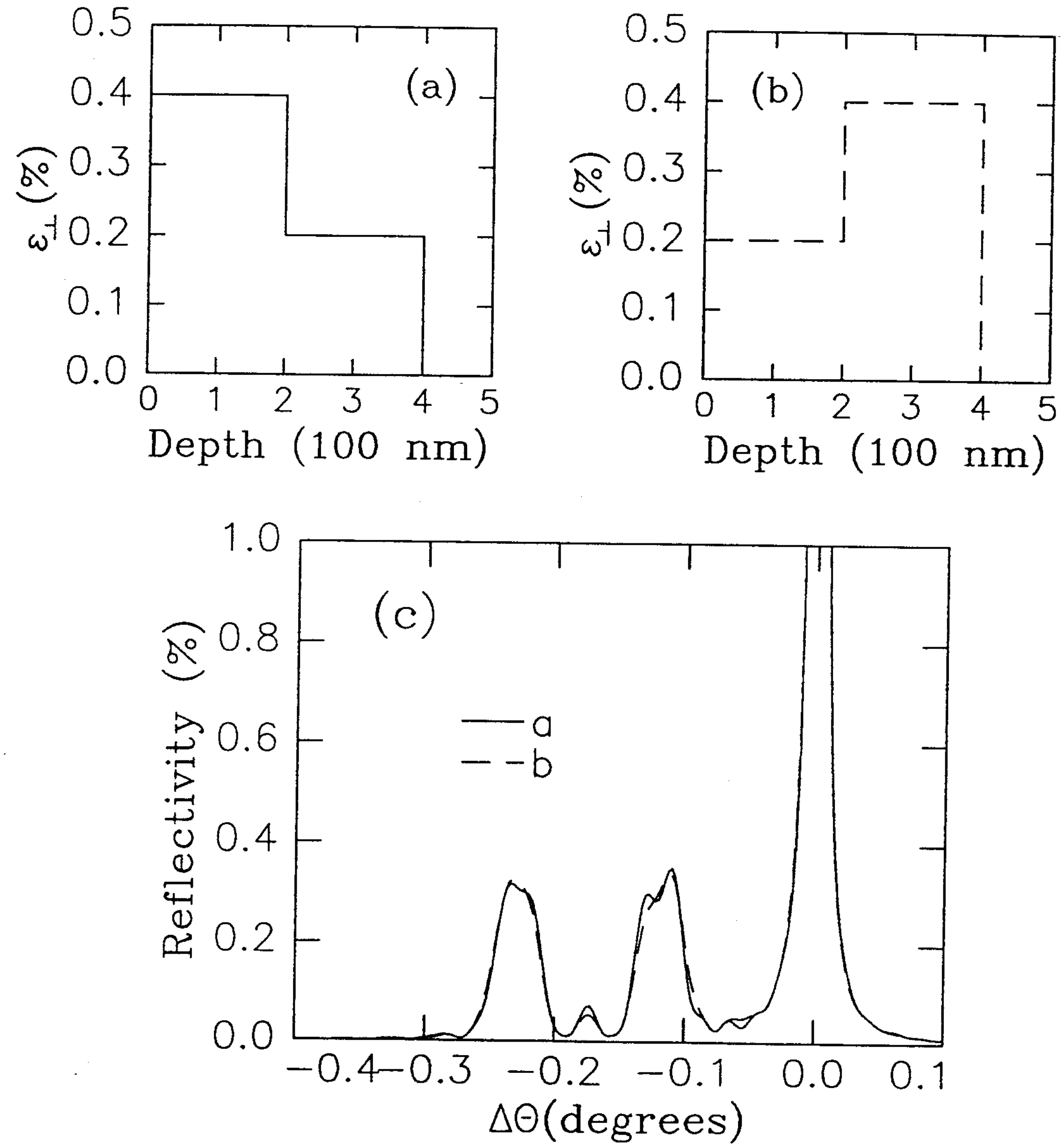

Figure 2.1 Calculated Fe-$K_{\alpha 1}$ (004) rocking curves for (001) Si with the strain distribution shown in (a) and (b).

A (001) silicon wafer of 0.4 mm thickness was irradiated on its polished side at 77K with 250 KeV Ar^+ ions with a beam flux of < 100 nA/cm^2 in a vacuum of $< 10^{-6}$ Torr to a dose of 4×10^{13} ions/cm^2. The sample was tilted 7° to minimize the ion channeling. The implanted sample was stored at room temperature for one month to minimize further room temperature annealing during X-ray analysis. X-ray rocking curves using (001) reflections were then taken. The sample was then etched in diluted CP4(5 HNO_3 :3 HF:3 CH_3COOH:44 H_2O) for 2 s in five steps. Other samples with larger doses of 250 KeV Ar^+, up to 5×10^{16} ions/cm^2, were used to find the range of strain and damage. The highest dose was sufficient to amorphize all of the damaged region. The thickness of this amorphized layer, determined using cross-section transmission electron microscopy (XTEM), marked the extent of the strained and damaged region. Contrast in XTEM micrographs of a sample given a dose of 5×10^{13} ions/cm^2, resulting from defects, marked the region of highest damage (Fig. 2.2).

Although the influence of strain on the etching rate is unknown, we assume that the thickness of the removed layer at each etching step is the same. The X-ray rocking curves taken after each etching step are shown in Fig. 2.3(a). Note that the first etch step reduces the reflectivity at small angular shift from the substrate peak (from 0 - 0.05°), leaving the remainder of the curve almost unaffected. This result indicates that there is a region of small strain near the surface leaving the large strain region unaltered. The highest damage is known from Fig. 2.2 to be located at 120 to 240 nm below the surface. The region of maximum strain begins to be removed in the third etching step and is almost completely removed at the fifth step, as seen in Fig. 2.3(a) by the decrease in intensity of the maximum strain peak at about 0.15°. We therefore estimate that the maximum strain was located at about 180 nm, in the middle of highest damage region. This indicates the depth removed per etching step was 50 nm ± 10%. The maximum range of strain and damage is about 420 nm estimated from the amorphous layer thickness of the sample given a dose of 5×10^{16} Ar^+/cm^2. The

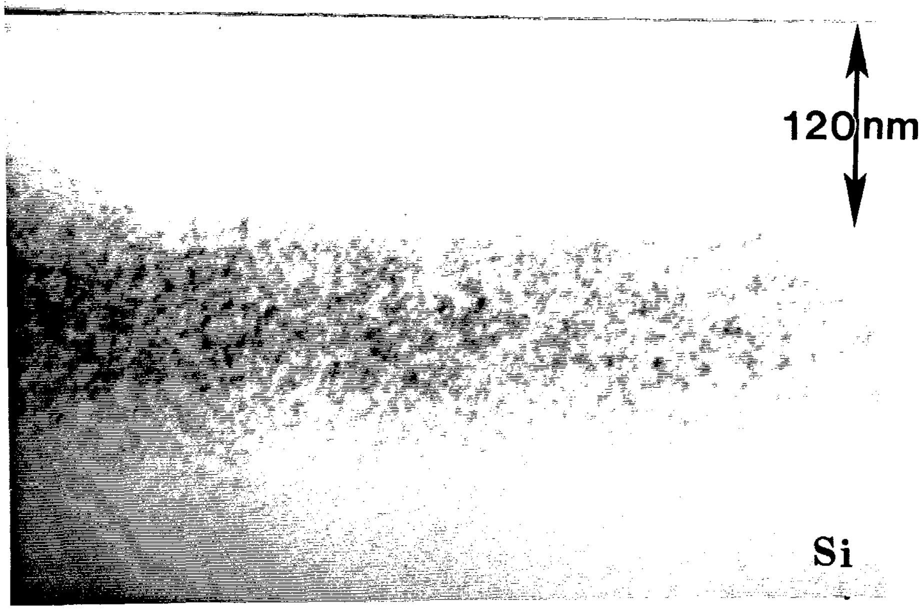

Figure 2.2 A XTEM micrograph of a (001) Si wafer implanted with 5×10^{13} Ar^+/cm^2 at 77K, revealing the region of highest damage between 120 nm and 240 nm.

thickness of the strained layer used for fitting the last rocking curve was then 170 nm (420-5×50 nm). Strain and damage profiles in this layer, following the shape of the TRIM profile [3], were then found which gave a calculated rocking curve which fit the last experimental rocking curve. For each additional 50 nm layer added to the surface of this sample, a new simulation was made with the strain and damage in only this layer being adjusted to give a best match to the corresponding experimental rocking curve. Figure 2.3(b) shows the resulting X-ray rocking curves obtained in this fashion for each etching step. Figure 2.4 shows the overlapping of the simulated rocking curve with the experimental rocking curve taken before etching. Final self-consistent strain and damage profiles for the entire implanted sample derived in this manner and $F_D(x)$, the average energy per ion per unit depth deposited by nuclear collision at depth x, from TRIM simulation are shown in Fig. 2.5.

Paine and co-worker [4] studied the strain produced by low-dose room-temperature

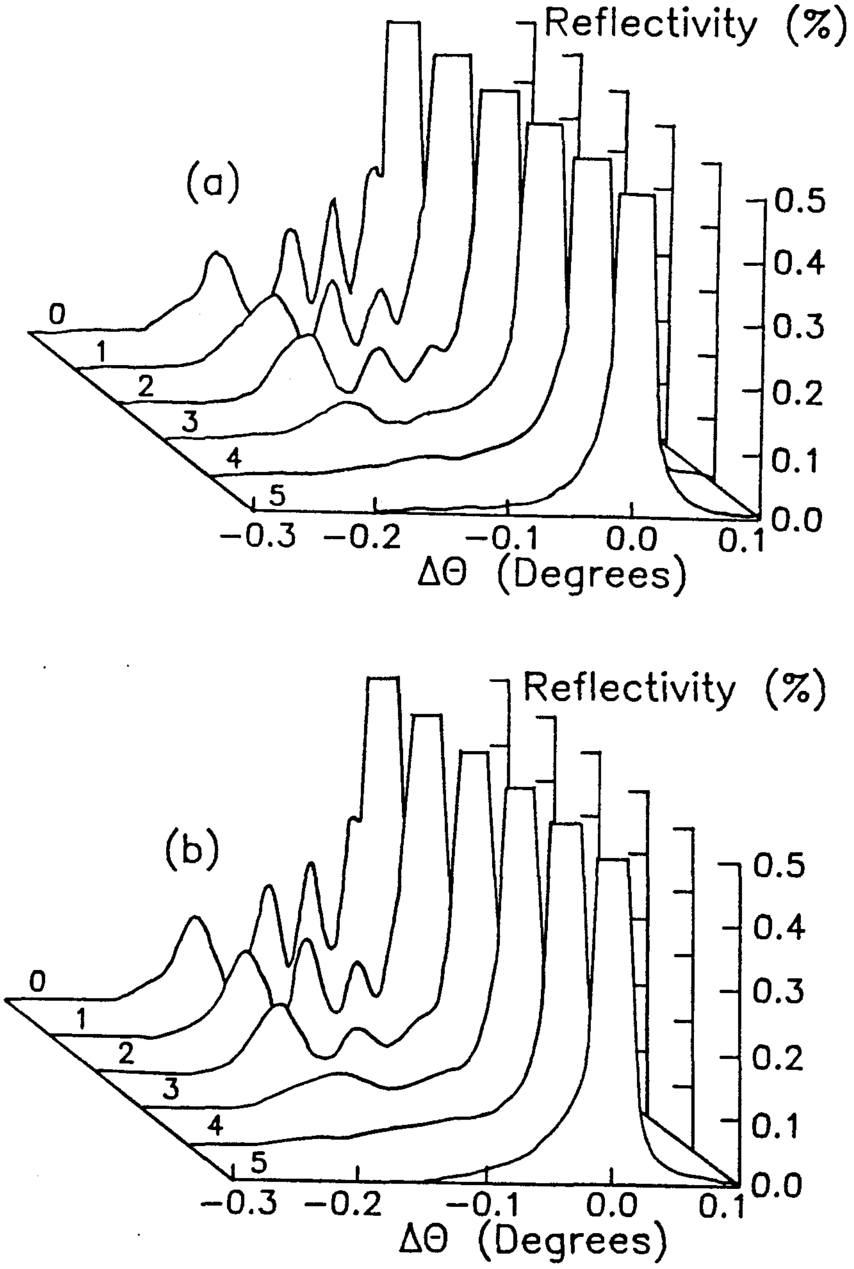

Figure 2.3 Experimental (a) and calculated (b) rocking curves for a (001) Si wafer implanted to a dose of 4×10^{13} ions/cm^2 with 250 KeV Ar$^+$ ions and analyzed with Fe-$K_{\alpha 1}$ (004) x-ray diffraction. The numbers (0-5) correspond to the etching steps.

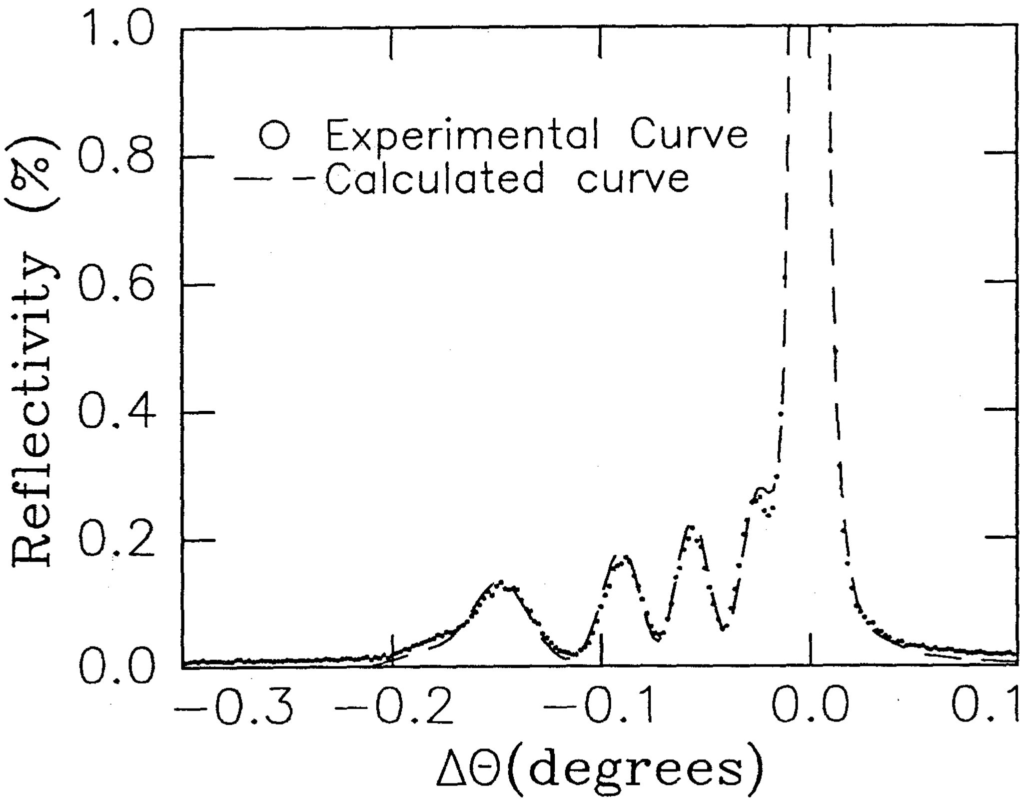

Figure 2.4 The calculated (dash line) and the experimental (solid line) rocking curve before etching.

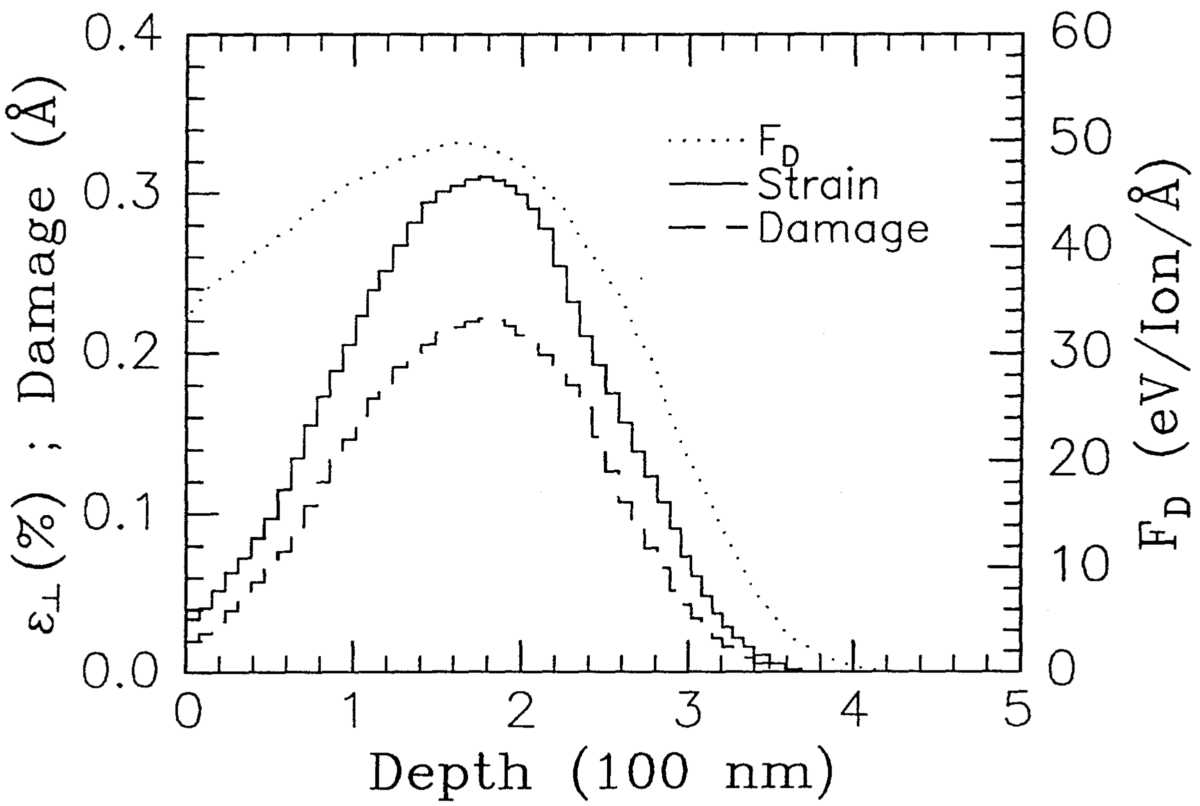

Figure 2.5 The self-consistent strain (solid line) and damage (dot-dash line) profiles which give the calculated curve in Fig. 2.4, and $F_D(x)$ (dotted line).

implantation in (001) GaAs and found that the X-ray strain perpendicular to the crystal surface, $\epsilon^{\perp}(x)$, is proportional to the $F_D(x)$. However, in the case of Si, the strain profile follows closely the curve of F_D beyond the maximum strain with a small shift in depth which is within the uncertainty of the depth removed by etching. The lower values of strain and damage toward the surface, as compared to F_D suggests that the surface acts as a sink for defects. Simple vacancies in Si are mobile at temperatures as low as 70K [5] and interstitial motion in Si is essentially athermal [6]. Thus, defect complexes must be responsible for the majority of the residual strain and damage observed.

In the simulation of X-ray rocking curves, attention must be given to the fact that profiles of strain and damage which give a calculated rocking curve that match an experimental rocking curve are not, in general, unique.

2.3 Measurements of Strain in Films with Nanometer Scale Thickness Using Thin Film X-ray Interferometry

Thin film X-ray interferometry has been used to characterize thin active layers in quantum well structures [7-11]. The interference effect is due to the phase shift generated by the thin embedded layer and has been shown to be sensitive to a thickness of a few monolayers for a large misfit system [11]. The application of the X-ray interferometry on a quantum well structure has been explained by Wie [9] and Tapfer et al., [10, 11] using the kinematical diffraction theory for the structure shown in Fig. 2.6(a). A structure shown in Fig. 2.6(b) is more complicated to formulate when the cap layer is the same material as the substrate, since the substrate can not be described properly using kinematical diffraction theory. In this case, dynamical diffraction theory is necessary to simulate the X-ray spectrum. The important information that can be extracted from the X-ray interference spectrum is the phase shift factor which is proportional to the product of the thickness and strain relative to the cap layer of the very thin films and the quality of the cap layer. Hence, if the

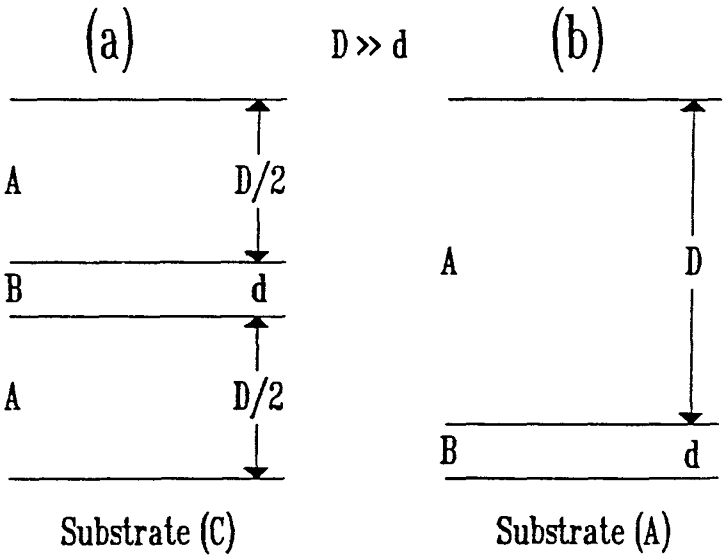

Figure 2.6 Schematics of two basic types of structure which will generate an X-ray interference effect.

thickness of a thin, highly-strained layer can be independently verified, its strain state can be determined. In the case of sputtering damage, the phase shift, ψ, generated by the bulk displacements in the sputtered layer can be written as

$$\psi = \frac{2\pi \sin(\theta_B)\cos(\phi)}{\lambda} \int_{t_0}^{t_f} x\epsilon(X)dx, \tag{1}$$

where θ_B is the Bragg angle of the substrate, ϕ is the angle between the lattice plane and the sample surface, λ is the X-ray wavelength, t_0 is the initial depth position of the damaged layer, t_f is the final depth position of the damaged layer, and $\epsilon(x)$ is the depth dependence of the perpendicular strain of the damaged layer. Replacing the depth dependence of the strain in the sputtered layer by average strain of the layer, ϵ_{av}, we have

$$\psi = \frac{2\pi \sin(\theta_B)\cos(\phi)}{\lambda}\epsilon_{av}(t_f - t_0). \tag{2}$$

2.3.1 Residual Strain in Low Energy Ion Bombarded Si

A smooth surface is an important initial condition for thin film growth, and can be achieved via thermal, physical, and chemical processes. Low energy ion bombardment has been employed as a low temperature processing technique for removing surface contaminants physically and/or chemically [13-18]. The physical process of low energy ion bombardment involves sputtering as well as the generation of surface and bulk displacements. Although the surface displacements can be removed by further annealing at higher temperatures to achieve a smooth surface, the effect of annealing on the bulk defects cannot be easily determined using typical surface analysis techniques. The bulk defects are known to produce changes in the lattice parameter normal to the surface plane [19, 20]. Little information for the atomic arrangement normal to the surface plane can be obtained from most surface analysis techniques. In work described here, We employed X-ray interferometry to study the strain generated by low energy ion bombardment.

The Si (001) substrates were cleaned using a method similar to that described by Eaglesham et al., [21], and this cleaning procedure is described in Appendix B. After a 250°C pre-bake *in situ* inside a molecular beam epitaxy chamber, the Si (001) substrates were heated to 450°C and then sputtered using a low energy Ar^+ ion beam (100-400 eV) with ion fluxes of the order of 1×10^{14} ions/cm^2-s to a dose on the order of 1×10^{15} ions/cm^2. A 150 nm Si film was grown on top of the sputtered surface at 500°C, at a growth rate of 0.1 nm/s.

Figure 2.7(a) shows the (004) diffraction peak of a Si (001) substrate sputtered with 300 eV Ar^+ ion beams to a dose of 1×10^{15} ions/cm^2. Figure 2.7(b) shows the (224) diffraction peak of the same sample as in (a). The solid lines in Fig. 2.7(a) and 2.7(b) are the curves calculated using dynamical diffraction theory with a phase shift factor $\psi = 1.78 \pm 0.15$. The corresponding TEM micrograph is shown in Fig. 2.7(c). The damaged region starts at a depth of about 160 nm from the surface and the strained region is estimated to be 5 nm wide. The strain in the sputtered layer can be estimated through the combined analysis of the XRC simulation and TEM observation. First, we extract the phase shift factors from the XRC data and the thicknesses from the TEM micrographs, then the average strain in the sputtered layer can be calculated using eqn. (2). The strain estimated this way for the sample shown in Fig. 2.7 is $(1.5 \pm 0.4)\%$.

Figure 2.8(a) shows the dose dependence of the interference spectrum of samples sputtered with 200 eV Ar^+. The phase shift factors were 0.35 ± 0.15 and 0.80 ± 0.15 for doses of 1.0×10^{15} Ar^+/cm^2 and 2×10^{15} Ar^+/cm^2 respectively . For a sample sputtered to a dose of 4×10^{15} Ar^+/cm^2, the interference spectrum is broadened significantly which makes the determination of the phase factor impossible. The broadening results from the quality of the cap layer which contains a significant number of dislocations, as shown in Fig. 2.8(b).

The ion energy dependence of the average strain is shown in Fig. 2.9. The thicknesses of the damaged layers sputtered with different ion energies were estimated using TEM and found to be 2.0 nm, 3.5 nm, 4.5 nm, and 7.0 nm for 100 eV, 200 eV, 300 eV, and 400 eV respectively. The average strain was then calculated using equation (1). All the films were sputtered using Ar^+ with different ion energies to a dose of 1×10^{15} ions/cm^2 at 500°C. As the ion energy increases the strain also increases monotonically. At 300-400 eV region, the average strain stop increasing and the sample sputtered with 400 eV Ar^+ shows dislocations in the cap layer which initiated in the sputtered layer.

Figure 2.10 shows the change of the X-ray interference spectrum after different annealing temperatures (500°C-900°C) for the sample shown in Fig. 2.7. The annealing time is 30 min. for all temperatures. It was found that annealing at temperatures lower than 900°C does not affect the X-ray spectrum which indicates that the defects created by sputtering are stable up to 900°C. This seems to suggest that the lowest temperature for defect annealing after sputtering cleaning the Si (001) surface is 900°C. However, when defect interaction can be neglected, the re-distribution of the defects will not change the total integrated phase factor. Thus, the X-ray interference spectrum will not be affected significantly. Furthermore, a sample with a cap layer

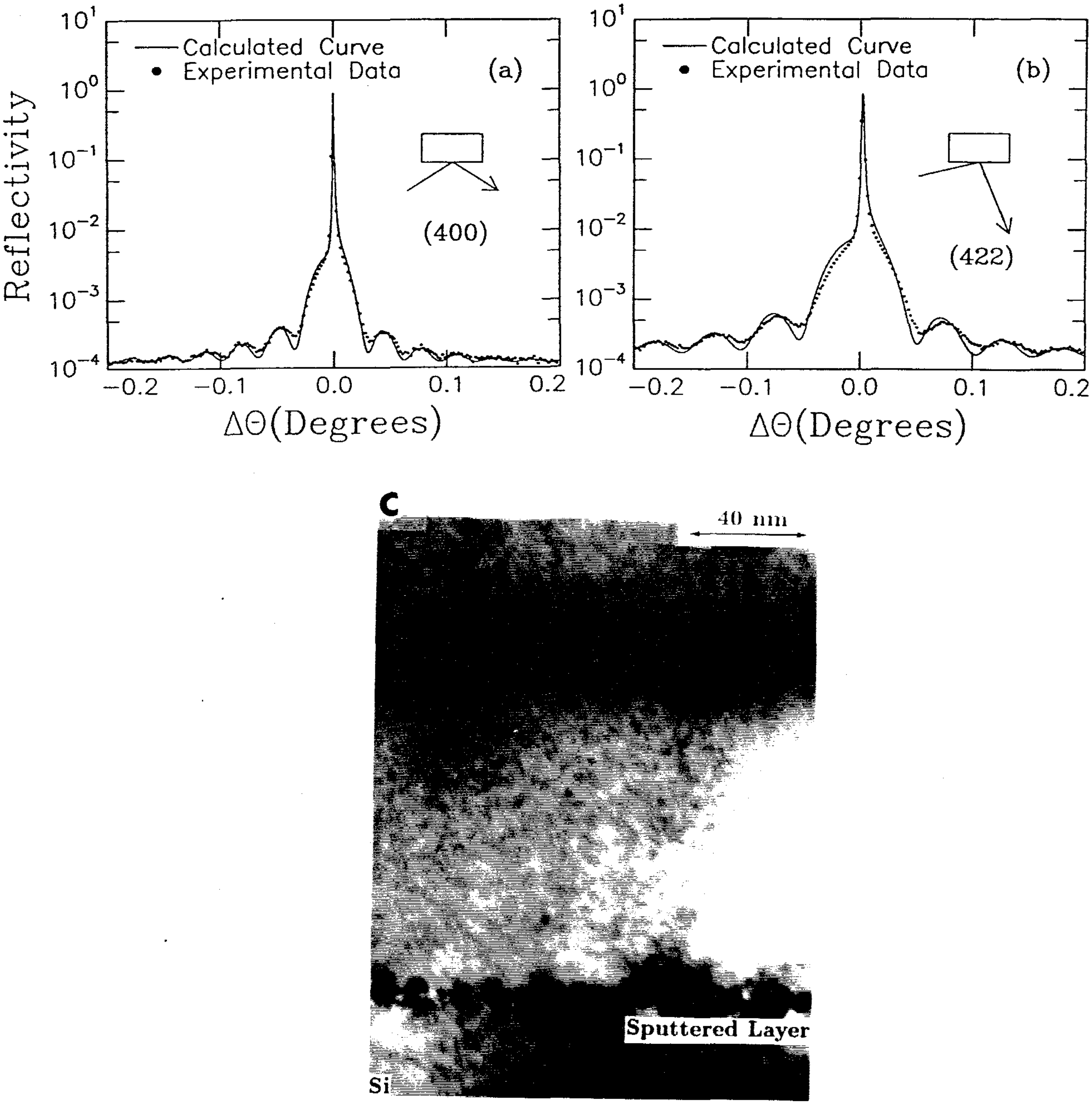

Figure 2.7 (a) The X-ray interference spectrum around the (004) diffraction peak of a Si (001) substrate sputtered with 300 eV Ar^+ to a dose of 1×10^{15} ions/cm^2. (b) The corresponding X-ray interference spectrum around a (224) diffraction peak. The solid lines in (a) and (b) are the calculated curves. (c) The corresponding TEM micrograph shows 160 nm thick cap layer Si on top of the sputtered substrate.

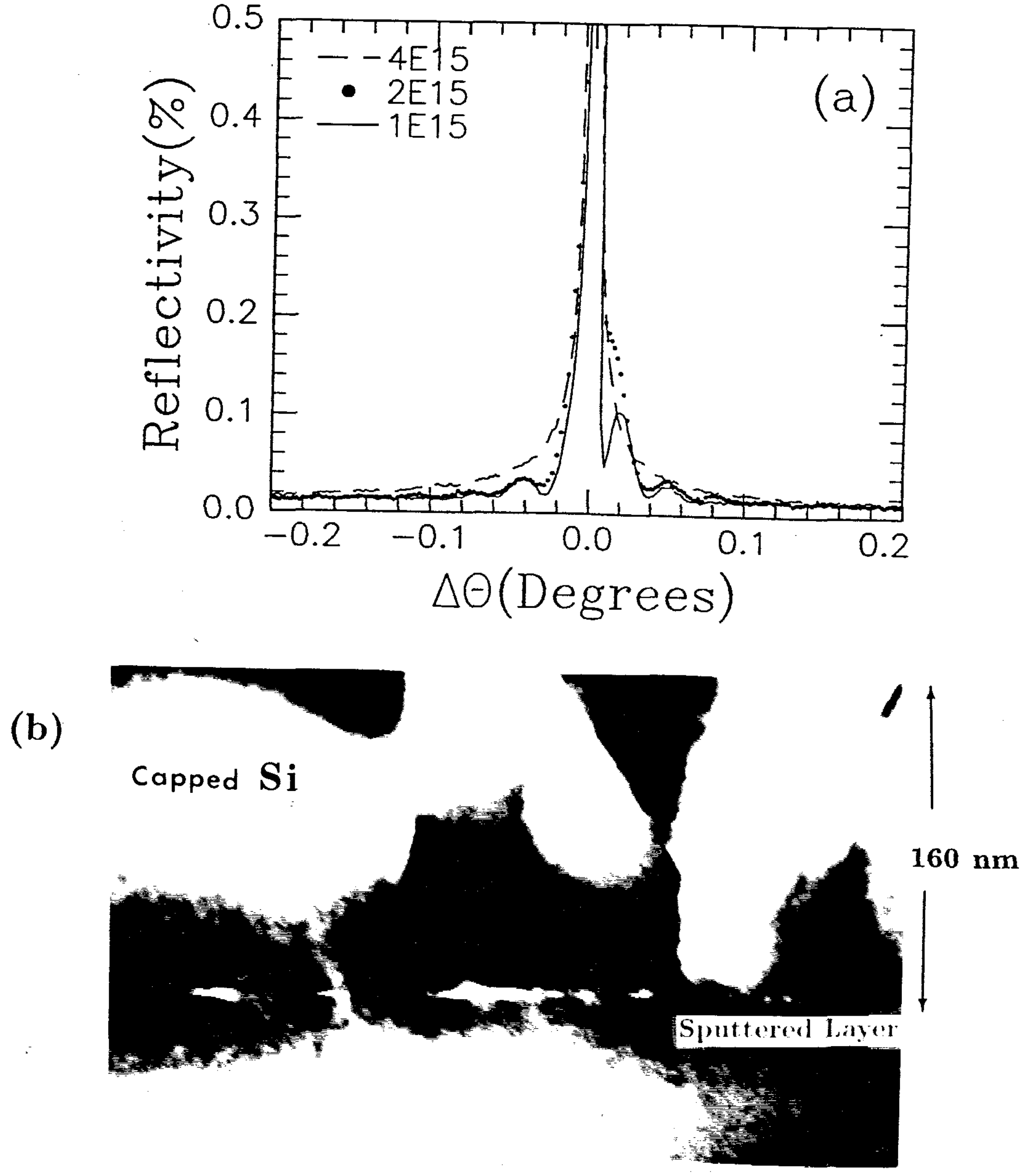

Figure 2.8 (a) The dose dependence of the interference spectrum for samples sputtered with 200 eV Ar^+. The dashed line is for the high dose sample which contained dislocations in the cap layer shown in (b). (b) The (110) bright field TEM micrograph of sample sputtered to a dose of 4×10^{15} Ar^+/cm^2.

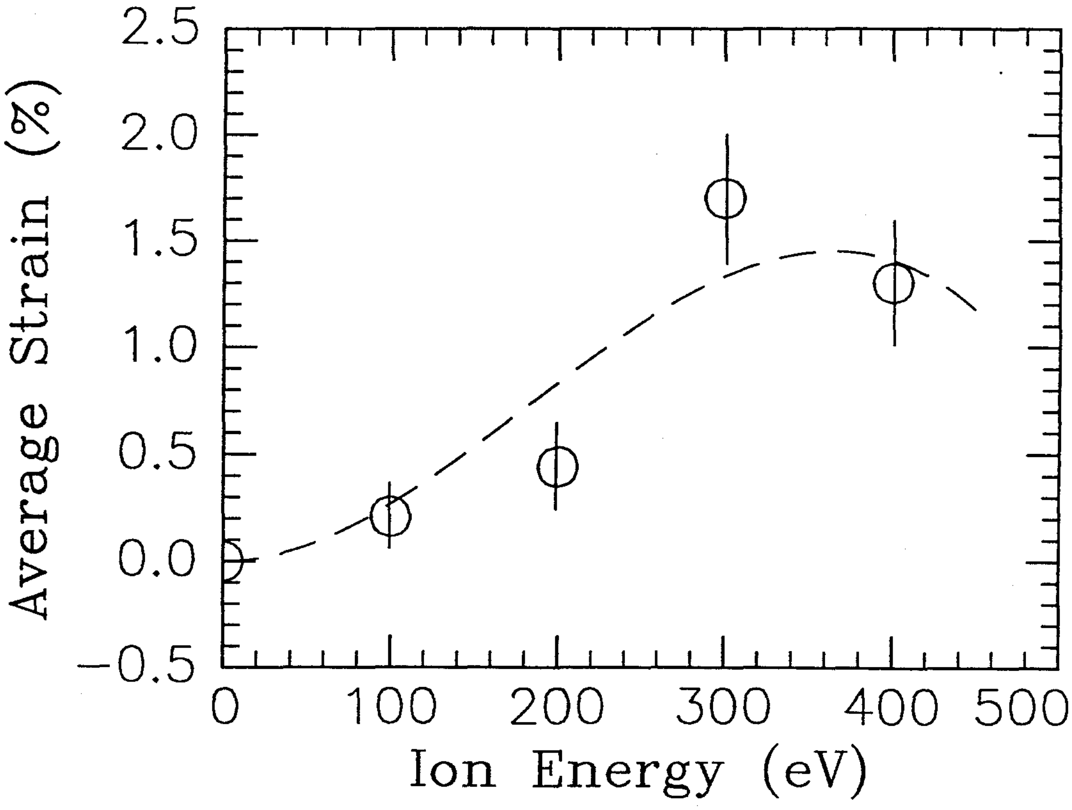

Figure 2.9 The ion energy dependence of the average strain in the sputtered layer. The samples were sputtered with different energy Ar^+ ion beams to a fixed dose of 1×10^{15} ions/cm^2 at 500°C. The error bars include the uncertainty of thickness (TEM) and phase shift measurements. The dashed line is a guide to the eyes.

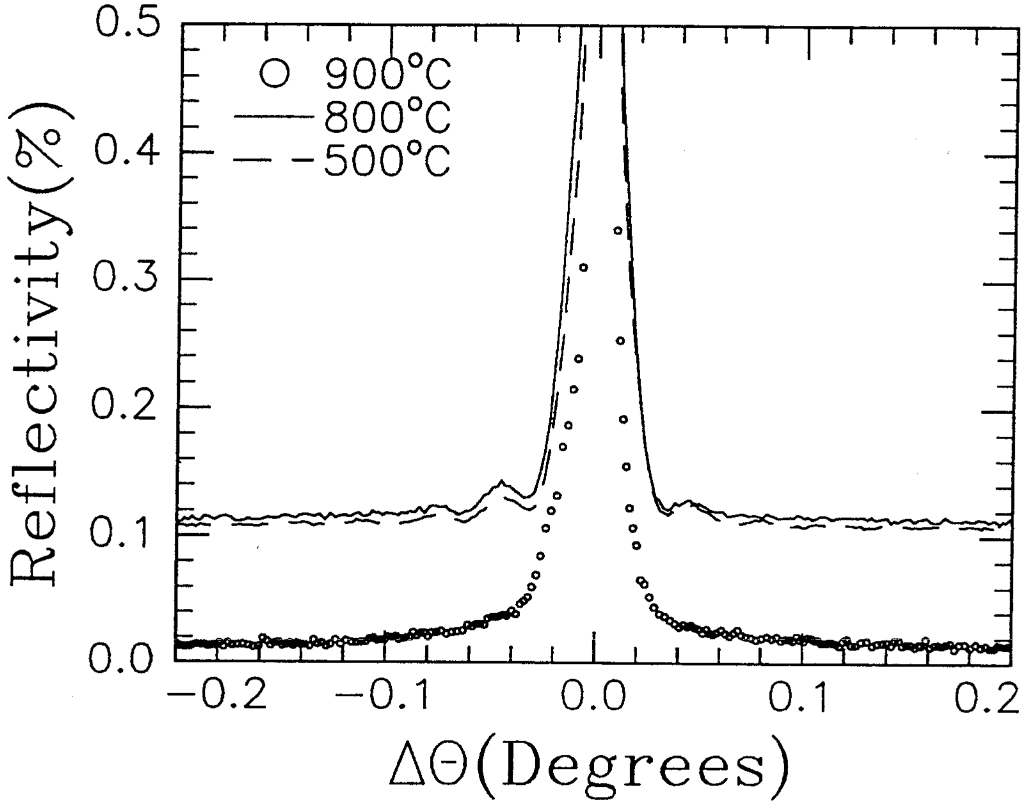

Figure 2.10 The changing of the X-ray interference spectrum after different annealing. The annealing time for all temperatures is 30 min. The reflectivities of samples annealed at 500°C and 800°C are shifted 0.1% for clarity.

on top of a sputtered layer may have a different annealing mechanism due to the relative accessibility of the sinks (e.g., free surface). These factors will affect the annealing temperature required for removing low energy ion sputtering damage. In the XTEM of the sample annealed at 900°C, the defect contrast produced by sputtering still exists which suggests that high temperature annealing is necessary for removing sputtering damage.

This is the first time that the strains generated by low energy ion sputtering (100-400 eV) of the surface have been measured. There are two difficulties involving in the analysis of the damage of the sputtered layer using the X-ray interference effect, (i) the phase shift is a function of the product of the thickness and the strain of the sputtered layer, thus, there is no unique fitting to the X-ray spectrum and (ii) a high quality top layer is essential for resolving the interference effect. The defects in the top layer can broaden the interference peak and smear out the information that can be extracted from the spectrum. The first difficulty can be resolved by combining TEM information and X-ray data to estimate the average strain in the sputtered layer.

Sputter cleaning procedures for Si surfaces have been investigated by Bean et al., [14] using 1 KeV Ar^+ ions to doses of the order of 1×10^{18} ions/cm^2 in the temperature range 25°-800°C. Since an increasing amount of damage was observed at higher sputtering temperatures and the damage consisting of trapped Ar bubbles and dislocation loops that were difficult to remove upon subsequent annealing, the proper sputter cleaning procedures include low temperature sputtering followed by high temperature annealing. Garverick et al., [16] use low energy ion beam (100 eV) and low ion dose (1×10^{16}) at temperature 750°C for Si surface cleaning and identify a window in ion energy and dose in which high quality epitaxial layers can be grown on top of the sputtered layer. The TEM micrograph provided in their work also show similar strain contrast in the sputtered layer. The observed damage widths for Si sputtered at 500°C are larger than works done by Al-Bayati et al., [22] in which the

Si substrates are sputtered at 200°C with Ar^+ ion energy from 60 to 510 eV, with corresponding damaged layer widths that vary from 2.0 to 4.3 nm. This also agrees with Bean et al., that the higher the sputtering temperature the wider the damaged region. The phenomenon was attributed to be due to an amorphous surface layer which prevented channeling of defects and incoming ions.

After sputter cleaning of a Si (001) surface using a low energy ion beam at a medium temperature (500°C), annealing at high temperature (900°C) is necessary to remove the sputtering induced defects as suggested by the post growth annealing which shows that these defects are possibly mobile at 900°C. However, high quality epitaxial layers can still be grown on top of the damaged layer. The low defect density epitaxial layers can be grown on top of sputtered layers with low defect densities. This suggests that the major issue in sputter cleaning is avoidance of the formation of extended defects through interaction of the point-like defects during the sputtering processes. Once the extended defects are formed in the sputtered layer, these extended defects are likely to propagate through epitaxial layers that are subsequently grown.

2.4 Misorientation Measurements

It is known that growth of a lattice mismatched heteroepitaxial system will introduce a misorientation between a film and its substrate as a misfit-relief mechanism. XRC is one of the best methods for measuring the misorientation angle [23, 24]. Figure 2.11 shows the geometry of the dependence of the peak separations between the film and its substrate on the rotation of the azimuthal angle, ω, of the sample. For small misorientation angle, φ, the relation of the peak separation , $\Delta\theta$, and the azimuthal angle can be expressed as

$$\Delta\theta = \Delta\theta_a + \varphi\cos(\omega - \omega_0), \tag{3}$$

where $\Delta\theta_a$ is the average peak separation between a film and its substrate due to the lattice constant difference only, and ω_0 is a term due to the arbitrary choice of starting azimuthal angle.

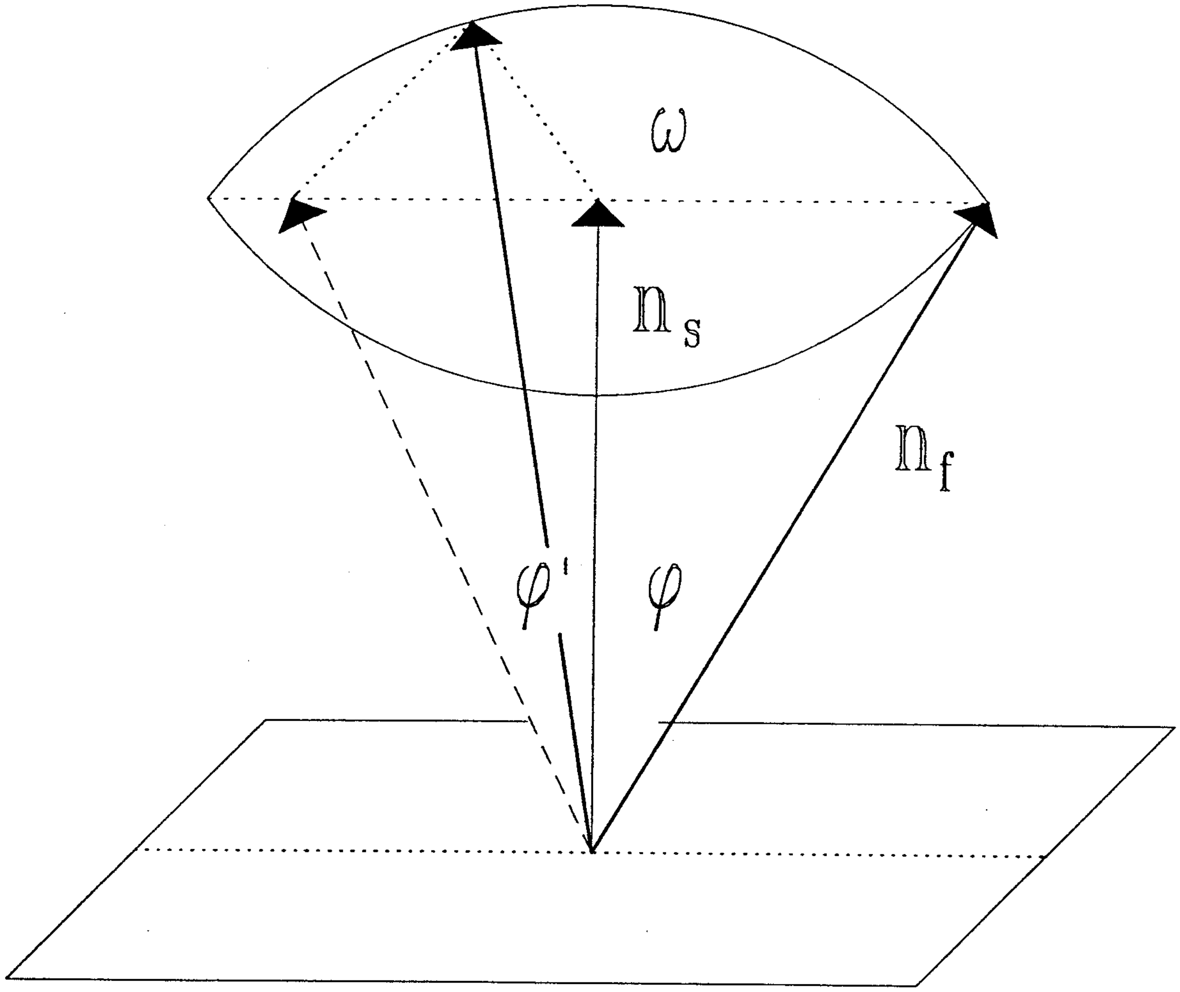

Figure 2.11 Schematic of misorientation dependence on the azimuthal angle.

Figure 2.12 shows a series of (004) diffraction peaks with different azimuthal angles for a 30 nm Ge film (grown at 300°C on Si (001) using molecular beam epitaxy with a growth rate of 0.1 nm/s and concurrent 200 eV Ar^+ at a ion-atom flux ratio of 0.15). After the 30 nm growth of the Ge film, the sample was annealed at 500°C and another 320 nm Ge was grown following annealing. Figure 2.13 shows the peak separation as a function of azimuthal angle. The solid line is a fitting curve of equation (2) and the misorientation between the film (001) direction and the substrate (001) direction is determined to be 0.2285° and the average diffraction peak separation is determined to be 1.5525°.

2.5 Conclusions

The application of the XRC provides valuable structural information for epitaxial films including strain profiles, damage profiles, and macroscopic interface structure (misorientation). The major advantage of the X-ray analysis is that it provide a non-destructive characterization method for strain measurement. With proper samples and conditions, the interference effect can be used to study nanometer thick films. The interference measurement gives the product of the strain and thickness in the film and requires a high quality cap layer. Thus, for strained layers with large lattice constant difference from the substrate, the sensitivity in the layer thickness measurement can be on the order of sub-monolayer, e.g., Ge sandwiched between Si layers. It is also possible to study the damage produced by low energy ion beam sputtering using the X-ray interference effect. The XRC analysis was used extensively in the following studies of the Si_xGe_{1-x} films on Si(001) or Ge(001) grown by low energy ion-assisted molecular beam epitaxy. In addition to a direct measurement of the strains in epitaxial films, curvature measurements can be employed to measure the in-plane stresses of amorphous or polycrystalline films on single crystal substrate.

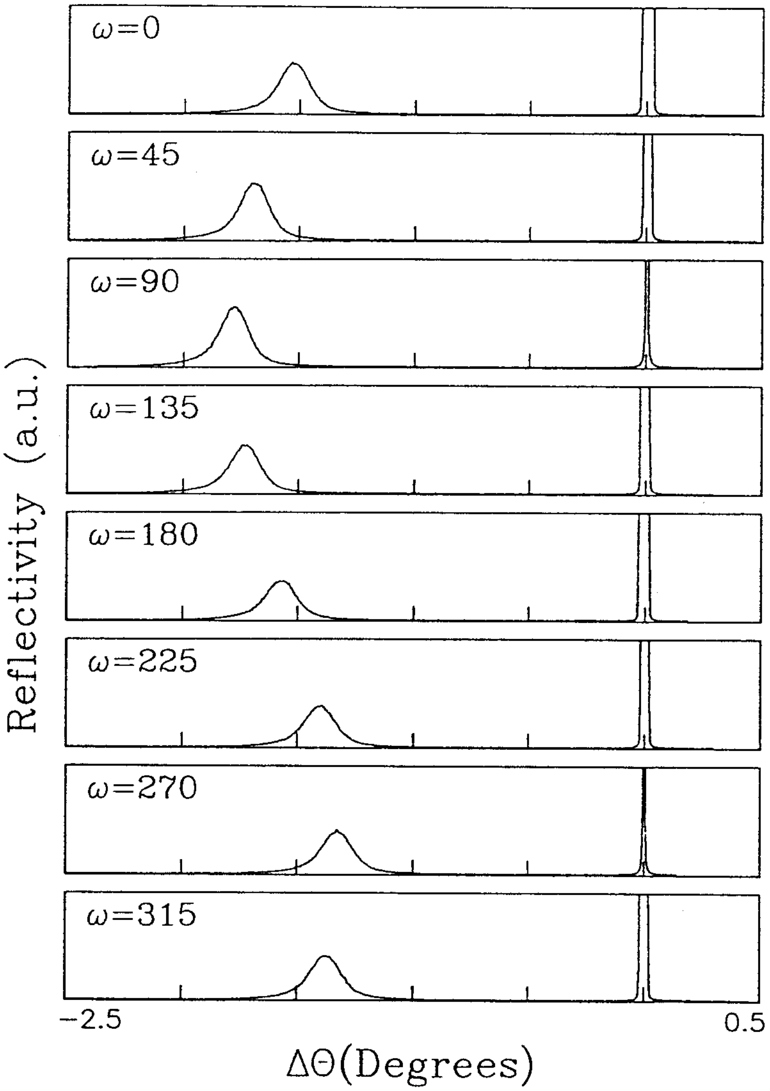

Figure 2.12 A series of (004) diffraction peak with different azimuthal angle for a sample with 350 nm thick Ge film on Si (001).

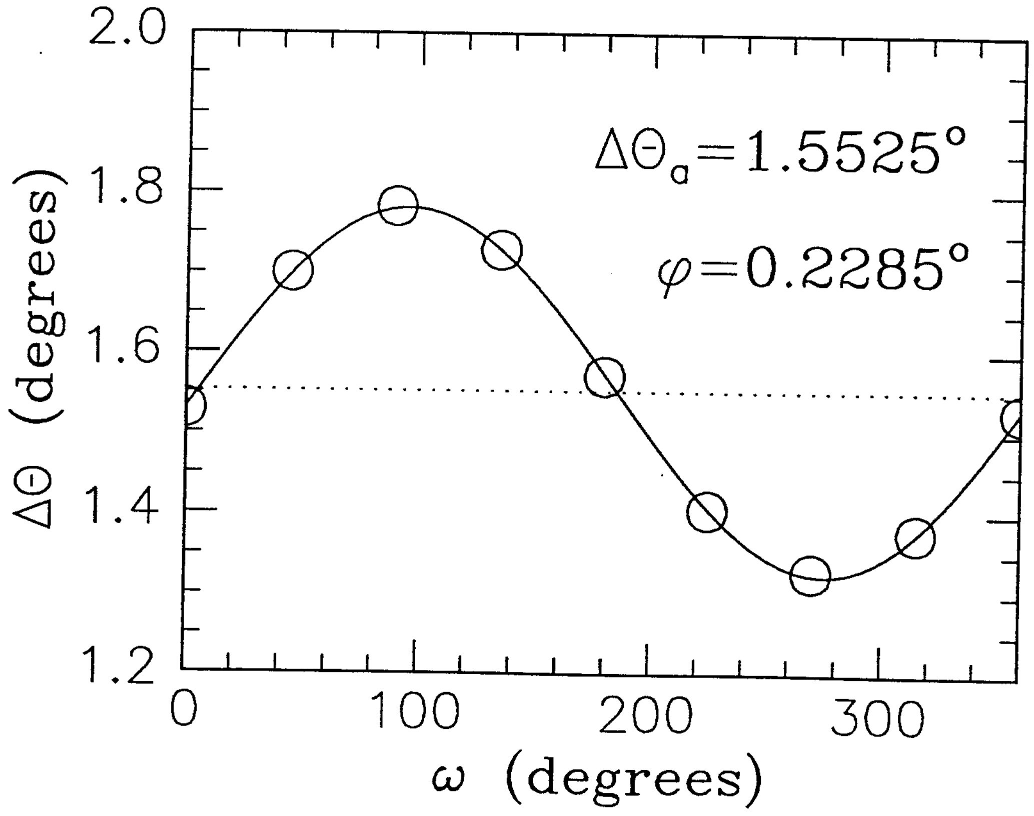

Figure 2.13 The peak separation as a function of azimuthal angle taken from Fig. 2.12 The solid line is a fitting curve using equation (2).

References

[1] T. Vreeland, Jr., A. Dommann, C.J. Tsai, and M.-A. Nicolet, Mat. Res. Soc. Symp. Proc. **130**, 3 (1989).

[2] V.S. Speriosu, H.L. Glass, and T. Kobayashi, Appl. Phys. Lett. **34**, 539 (1979).

[3] J.P. Biersack and L.G. Haggmark, J. Nucl. Instrum. Methods **174**, 257 (1980).

[4] B.M. Paine, N.N. Hurvitz, and V.S. Speriosu, J. Appl. Phys. **61**, 1335 (1987).

[5] J. Bourgoin and M. Lannoo, "Point Defects in Semiconductors II"; (Springer, Berlin, 1983).

[6] A. Seeger and K.P. Chik, Phys. Status Solidi **29**, 455 (1968).

[7] X. Chu and B.K. Tanner, Appl. Phys. Lett. **49**, 1773 (1986).

[8] J. Jeong, T.E. Schlesinger, and A.G. Milnes, J. Cryst. Growth.**87**, 265 (1988).

[9] C.R. Wie, J. Appl. Phys. **65**, 1036 (1989).

[10] L. Tapfer and K. Ploog, Phys. Rev. B **40**, 9802 (1989).

[11] L. Tapfer, M. Ospelt and H. von Känel, J. Appl. Phys. **67**, 1298 (1990).

[12] C.R. Wie, T.A. Tombrello, and T. Vreeland, Jr., J. Appl. Phys. **59**, 3743 (1986).

[13] E. Taglauer, Appl. Phys. A **51**, 238 (1990).

[14] J.C. Bean, G.E. Becker, P.M. Petroff, and T.E. Seidel, J. Appl. Phys. **48**, 907 (1977).

[15] J.H. Comfort, L.M. Garverick, and R.Reif, J. Appl. Phys. **62**, 3388 (1987).

[16] L.M. Garverick, J.H. Comfort, T.R. Yew, R.Reif, F.A. Baiocchi, and H.S. Luftman, J. Appl. Phys. **62**, 3398 (1987).

[17] K.M. Horn, J.Y. Tsao, E. Chason, D.K. Brice, and S.T. Picraux, J. Appl. Phys. **69**, 243 (1991).

[18] E. Chason, J.Y. Tsao, K.M. Horn, S.T. Picraux, and H.A. Atwater, J. Vac. Sci. Technol. A **8**, 2507 (1990).

[19] C.J. Tsai, H.A. Atwater, and T. Vreeland, Appl. Phys. Lett. **57**, 2305 (1990).

[20] C.J. Tsai, P. Rozenak, H.A. Atwater, and T. Vreeland, J. Crystal Growth **111**, 931 (1991).

[21] D.J. Eaglesham, G.S. Higashi, and M.Cerullo, Appl. Phys. Lett. **59**, 685 (1991).

[22] A.H. Al-Bayati, K.G. Ormann-Rossiter, R. Badheka, and D.G. Armour, Surf. Sci. **237**, 213 (1990).

[23] S.K. Ghandhi and J.E. Ayers, Appl. Phys. Lett. **53**, 1204 (1988).

[24] G. Bai, Ph.D. thesis, Caltech, (1991).

Chapter 3
Strain Modification Using Ion-Assisted Molecular Beam Epitaxy

3.1 Introduction

Low temperature semiconductor thin film processing has been the subject of recent interest and research, among them (i) the ability to achieve very abrupt doping profiles which will enable further advances in high density integration and new device functions, (ii) metal interconnects can be formed before the epitaxial growth which could allow much more flexible processing design, and (iii) the ability to control the microchemistry and microstructure of the deposited films which improve the ability to control device performance. Film growth processes must compensate for the reduced thermal energy at lower processing temperatures. Hence, external energy sources are needed to activate diffusion and reaction kinetics or produce a change in the processing surface, such as crystal growth, etching, doping, and oxidation. Energy sources used are photon and ions, i.e., laser-assisted processing or ion-assisted processing.

The bombardment of materials with energetic particles produces phenomena that have become of great importance in thin film technologies. All of these various phenomena involve different aspects of ion-solid interactions. The impinging energetic ions can be trapped on the surface or within the materials, or reflected from the surface. Which of these occurs in any situation is strongly influenced by the kinetic energies of the ions, the temperature of the bombarded surface, and the trapping mechanisms which include physisorption, chemisorption, chemical reaction and implantation [1]. The energy transferred from the ions to the atoms of the target produces effects like elastic collision, sputtering, ion mixing, defects production, thermal spike, electronic excitation, etc. Despite the intensive use of energetic ion beams in materials processing, the simply and highly successful physical description of ion-solid interaction is based on the binary collision model which is limited to collisions for high energy ion beams only. In 1950's-1970's, the major research activities in the ion beam modification of materials surround the uses of ion beams with energies larger than 1 KeV which can be described adequately with the binary collision model. From the 1970's, the applications of low energy ion beam ($E_i < 1$ KeV) have greatly increased, which triggered intensive modeling of low energy ion beam interactions with surface using molecular dynamics methods with many-body potentials [2, 3]

Low energy ion beams can stimulate thermal kinetic processes in thin film growth and surface processing. Applications reported to date include surface cleaning [4], enhanced dopant incorporation [5], physical or chemical surface smoothening [4-7], growth mode modification [10], and strain modification [11, 12]. Direct low energy ion beam deposition [13], partially ionized vapor deposition [14], ion beam sputter deposition [15, 16], and concurrent low energy ion bombardment during sputtering deposition [17] which also produced Si homoepitaxial films at much lower growth temperatures than conventional thermal molecular beam epitaxy (MBE). Although there are many potential advantages in using low energy ion bombardment as a tool for structure and property control, the damage generated by the ion beam is still a main concern especially for high quality epitaxial films in electronic applications. Improved understanding of ion-surface interactions during growth may help us in identifying the regime in which surface and near-surface processes, such as surface diffusion and incorporation at growth sites, can be enhanced at low temperatures while avoiding or controlling damage in the deposited films. This chapter is mainly concerned with systematic experimental observation of the effects of defects generated by the ion-assisted molecular beam epitaxial (IAMBE) growth process on film structure.

3.2 Experimental Setup

Films were grown in a custom-designed molecular beam epitaxy system with two electron beam sources and a Kaufmann-type ion source capable of producing Ar^+ or Xe^+ ion beams at energies of 50 eV-1200 eV. The schematic diagram of the system is shown in Fig. 3.1. The base pressure of the system was 5×10^{-10} Torr, and during the operation of ion gun the system was back-filled with Ar or Xe gas to a typical pressure of 8×10^{-5} Torr. Strain-modified films 100 nm thick were grown at a constant rate in the range 0.1-0.7 nm/s on (001) Ge substrates and 0.08-0.2 nm/s on (001) Si substrates, following growth of a 50 nm buffer layer of pure Ge or Si by conventional molecular beam epitaxy. Ion beam current density was measured using both a Faraday cup mounted adjacent to the Mo substrate block and measurement of ion current at the substrate block, and ion-atom flux ratios were typically in the range 1:10 - 1:100. Temperature was measured using a calibrated optical pyrometer. Growth temperatures were in the range of 200 - 450°C. RHEED was used for *in situ* monitoring of the surface. A four-crystal high resolution X-ray diffractometer [18] using a Cu-$K_{\alpha 1}$ radiation source as discussed in Chapter 1 or a double crystal X-ray diffractometer using a Fe-$K_{\alpha 1}$ radiation source was employed to analyze the film strains. Comparison of experimental data with simulations based on dynamical X-ray diffraction theory [19] was used to determine the strains. Ruthford backscattering spectrometer (RBS) was used to resolve the concentration of inert gas atom trapped inside the film and the alloy composition of $\mathrm{Si}_x\mathrm{Ge}_{1-x}$. Post-growth annealing was performed in a vacuum furnace with a pressure of 5×10^{-6} Torr.

3.3 Strain Modification:

The strain state for a 100 nm thick Ge film on (001) Ge grown by IAMBE is illustrated by the XRC diffraction intensity in Fig. 3.2(a), taken around the (004) and (224) Bragg angles using Cu - $K_{\alpha 1}$ radiation. The film was grown at $T = 300$°C, at a growth rate of 0.3 nm/s with a Ar^+ energy of $E_i = 200$ eV and ion-to-atom flux ratio of $J_i/J_a = 0.03$. In both cases, sharp Bragg peaks of instrumentation-limited and finite-thickness-limited widths were observed. Comparison of experimental X-ray data to a dynamical X-ray diffraction model, allowed strain to be extracted [19]. The results indicate the presence of a coherent film, i.e., $\epsilon_{||} = 0\%$, with perpendicular

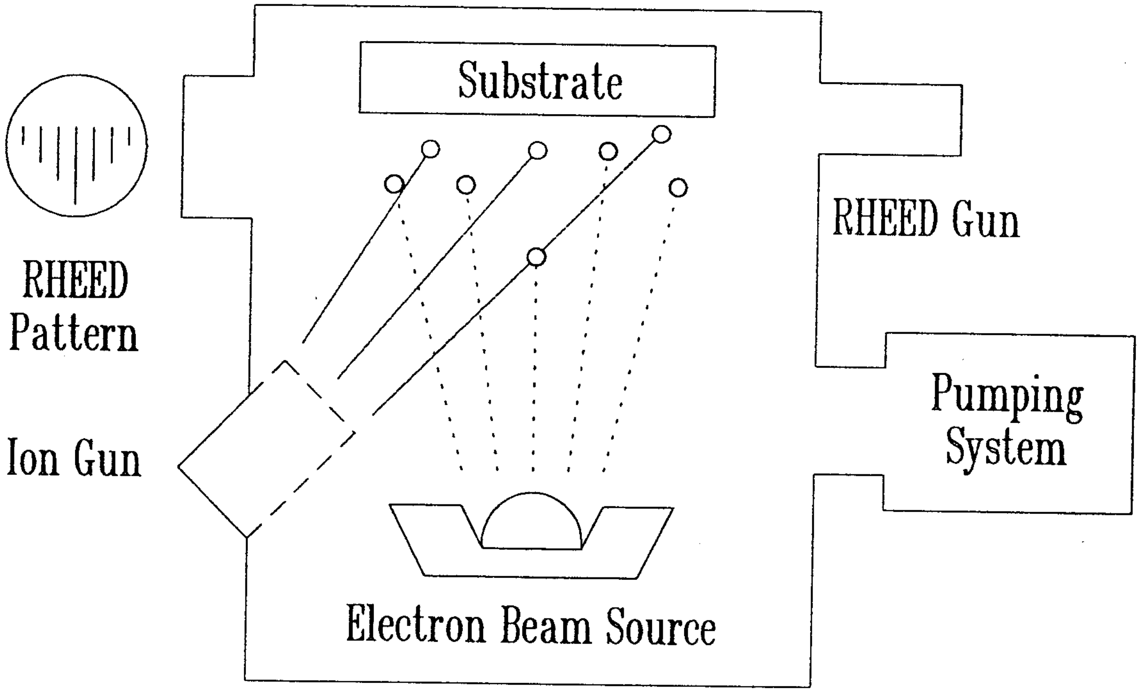

Figure 3.1 Schematics of the growth chamber equipped with electron beam sources, Kaufmann-type ion source, and reflection high energy electron gun for *in situ* monitoring the growth surface.

strain resulting in a tetragonal distortion such that $\epsilon_\perp = 0.82\%$. The post-growth RHEED pattern taken at 20 keV along a [110] azimuth provides a qualitative indication of a smooth surface morphology with (2x1) surface reconstruction. Cross-sectional transmission electron microscopy indicated the 100 nm film to be free of misfit dislocations, threading dislocations and stacking faults, indicating that strain modification did not occur as a result of the introduction of linear or planar defects. Figure 3.2(b) shows a cross section TEM micrograph of the sample, note that the film grown by IAMBE process has higher strain contrast as compared with the substrate and thermally grown buffer layer. Figure 3.3 shows XRC and RHEED results for a $Si_{.2}Ge_{.8}$ layer grown on Ge (001) by IAMBE at a growth rate of 0.25 nm/s with an Ar^+ energy of $E_i = 200$ eV and ion/atom flux ratio of $J_i/J_a = 0.03$. In the rocking curve scan around (004) diffraction angles, the Bragg peak from the 250 nm film occurs at $\Delta\theta = +0.11°$ with respect to the substrate Bragg peak. It should be noted that a coherent film with this alloy composition grown by conventional MBE exhibits a Bragg peak at $\Delta\theta = +0.5°$, with an associated strain of $\epsilon_\perp = -1.3\%$. The magnitude and sign of strain modification are nearly equal for the pure Ge film and the $Si_{.2}Ge_{.8}$ alloy, strongly suggesting that the normally tensile strain in the $Si_{.2}Ge_{.8}$ alloy was compensated by point defects introduced by IAMBE growth. The RHEED pattern also indicates a smooth surface morphology. Similar stresses in the Si_xGe_{1-x} grown on Si using ion-beam sputtering deposition have also been observed [16]. The films with thicknesses larger than the critical thickness for dislocation formation still retain a compressive strain.

The variation of perpendicular strain, $\epsilon_\perp$, with ion-to-atom flux ratio J_i/J_a, for 100 nm thick Ge films grown on Ge (001) with Ar^+ 200 eV and Xe^+ 200 eV at $T = 300°C$ and for 100 nm thick Si films grown on Si (001) with Ar^+ 100 eV at $T = 350°C$ by IAMBE is shown in Fig. 3.4. The expansion of the lattice constant in the growth direction in Xe^+ bombarded films is less than that for Ar^+ bombarded films with the same ion-atom flux ratio. This is consistent with the assumption that Xe^+ ions

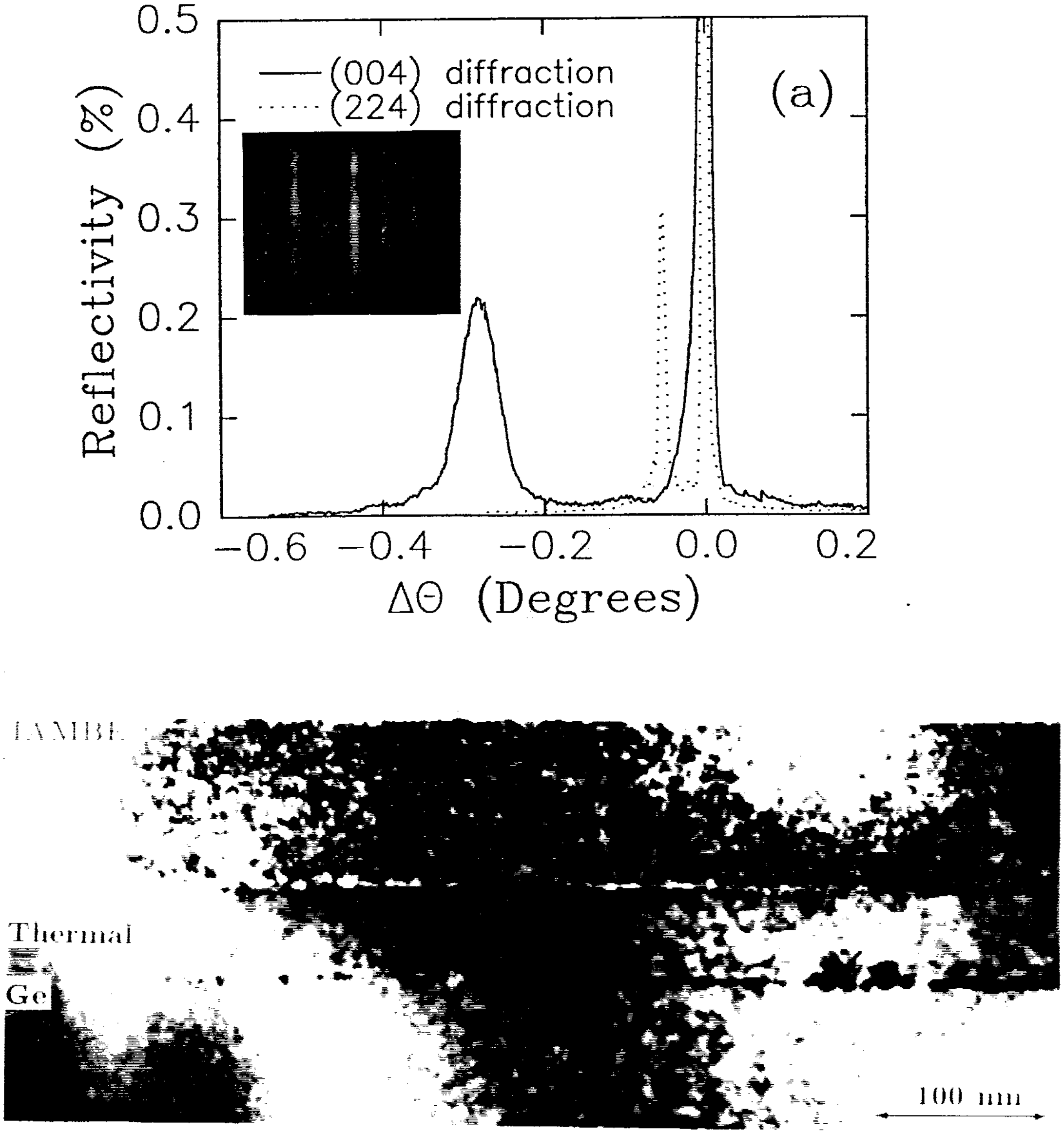

Figure 3.2 (a) X-ray rocking curves around (004) and (224) Bragg peaks for a 100 nm thick Ge film grown on (001) Ge by IAMBE at $T = 300°\mathrm{C}$ for an ion-to-atom flux ratio $J_i/J_a = 0.03$, and incident Ar^+ ion beam energy $E_i = 200$ eV. 20 KeV RHEED pattern at incident angle of 2° is shown as inset. (b) The corresponding bright field cross section transmission electron micrograph taken along the [110] zone axis.

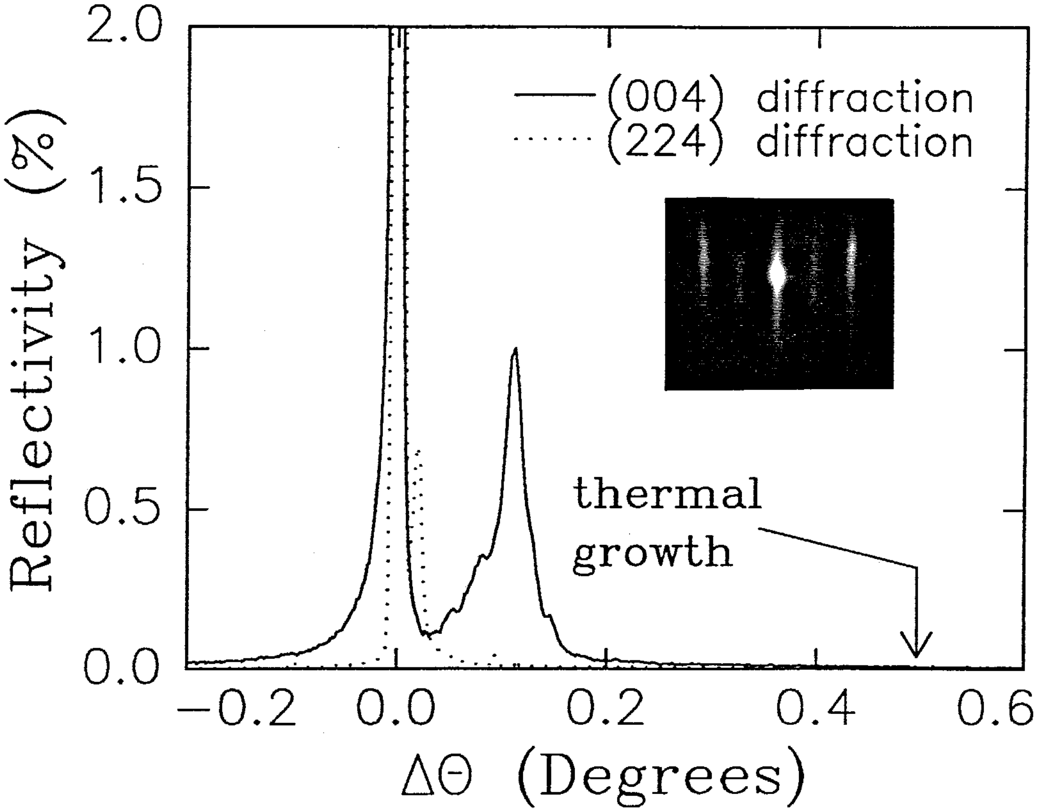

Figure 3.3 X-ray rocking curves around (004) and (224) Bragg peaks for a 250 nm thick $Si_{0.2}Ge_{0.8}$ / (001) Ge grown by IAMBE at $T = 300°C$; ion-to-atom flux ratio $J_i/J_a = 0.03$; incident Ar^+ ion beam energy $E_i = 200$ eV. 20 KeV RHEED pattern at incident angle of 2° is shown as inset.

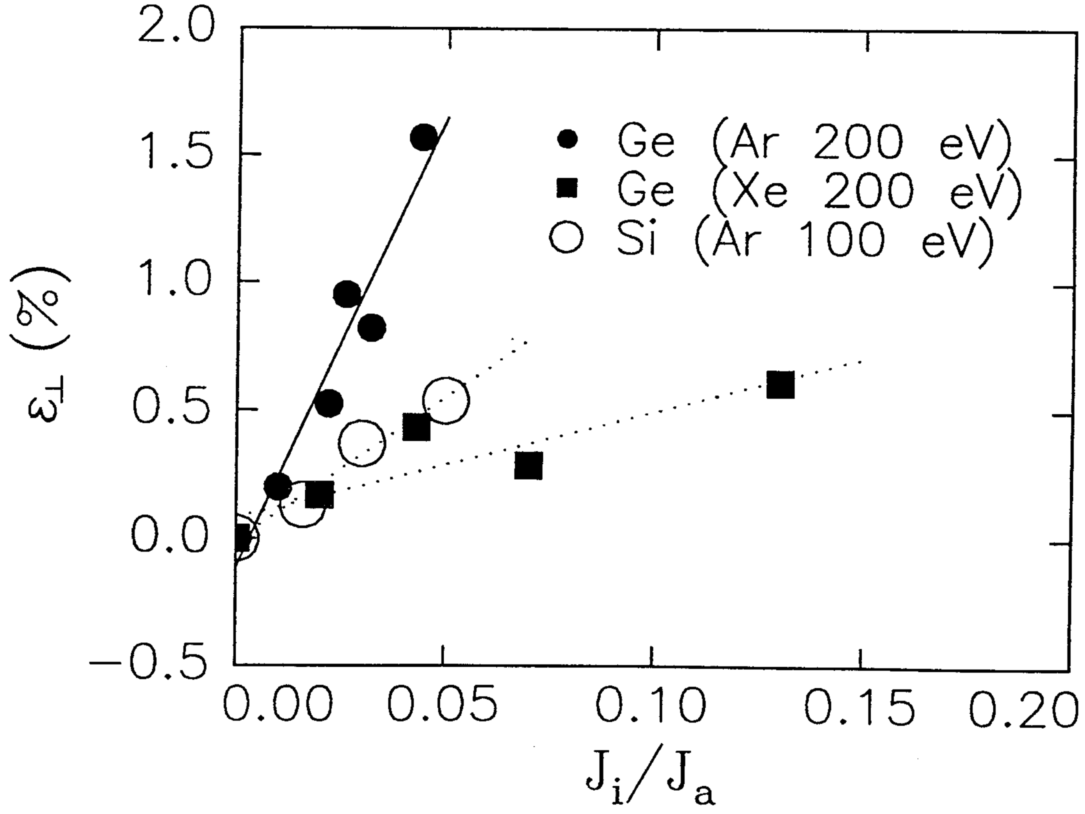

Figure 3.4 Variation of perpendicular strain $\epsilon_\perp$ with ion-to-atom flux ratio J_i/J_a at the surface for 100 nm thick Ge films grown on (001) Ge by IAMBE at $T = 300°C$ with (•) Ar^+ ion energy $E_i = 200$ eV, and with (■) Xe ion energy $E_i = 200$ eV, and for 100 nm thick Si films grown on (001) Si by IAMBE at $T = 350°C$ with (○) Ar^+ ion energy $E_i = 100$ eV. The uncertainty in the measurement of J_i/J_a is ± 0.004 which is not shown.

produce fewer bulk defects than Ar^+ ions with the same energy and the projected range of Xe^+ is smaller than that of Ar^+ [20]. Figure 3.5 shows the variation of the perpendicular strain, static displacement, and full width half maximum (FWHM) with J_i/J_a for 100 nm Ge films grown on Ge (001) substrate with Ar^+ 200 eV at $T = 300°C$ by IAMBE. Beside the $\epsilon_\perp$, the static displacement (defined in Chapter 1) of the films is proportional to J_i/J_a also, whereas the FWHM increases very quickly for $J_i/J_a > 0.03$. Assume that the point defects are clustered together such that their displacement fields simply superimpose on each other, in this case, the volume change remains the same but the correlations between the point defects and the fluctuations of the displacement field increase rapidly [21]. The rapid rise in FWHM for films grown at high ion-to-atom flux ratios indicates that the interactions between point defects are important. Assuming defect concentration is 1 atomic % (the trapped gas concentration), the interaction length is estimated to be approximately 1.5 nm.

The variation of perpendicular strain, $\epsilon_\perp$, with incident ion energy, E_i, for Ge films grown on Ge substrates by IAMBE at $T = 300°C$ with $J_i/J_a = 0.02$, and for Si films grown on Si substrate by IAMBE at $T = 350°$ C with $J_i/J_a = 0.016$ are shown in Fig. 3.6. A monotonic increase in strain with increasing incident ion energy in the energy range $E_i = 70 - 300$ eV is observed. In both cases, no detectable strain modification is observed for ion energies below 70 eV. The calculations of Brice et al., [20] suggest that the surface-to-bulk displacement, R, varies from $R = 1.6$ at $E_i = 100$ eV to $R = 8$ at $E_i = 50$ eV for Ge surface bombarded by Ar^+ ions. Although the determination of threshold energy for strain modification is affected by the instrument sensitivity and the threshold is expected to be temperature dependent, the close agreement between the theoretical estimate of the transitional energy regime for the onset of bulk displacements in Ge by Brice et al., [20] and this experiment is noteworthy.

The variation of perpendicular strain, $\epsilon_\perp$, with temperature for 100 nm thick Ge films grown on Ge substrates by IAMBE is shown in Fig. 3.7. The ion-to-atom flux

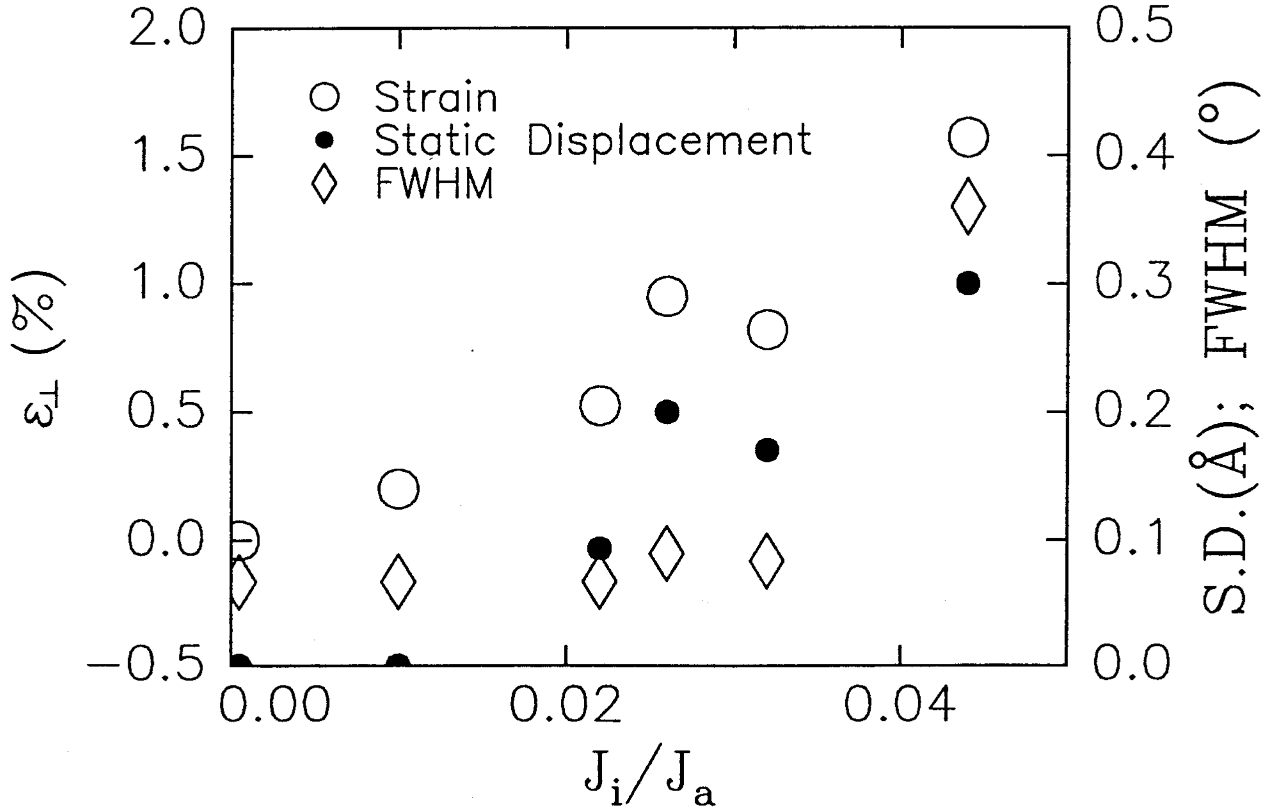

Figure 3.5 Variation of perpendicular strain $\epsilon_\perp$, static displacements (damage), and FWHM with ion-to-atom flux ratio J_i/J_a at the surface for 100 nm thick Ge films grown on (001) Ge by IAMBE at $T = 300°C$ with Ar$^+$ ion energy $E_i = 200$ eV. The uncertainty in the measurement of J_i/J_a is ±0.004 which is not shown.

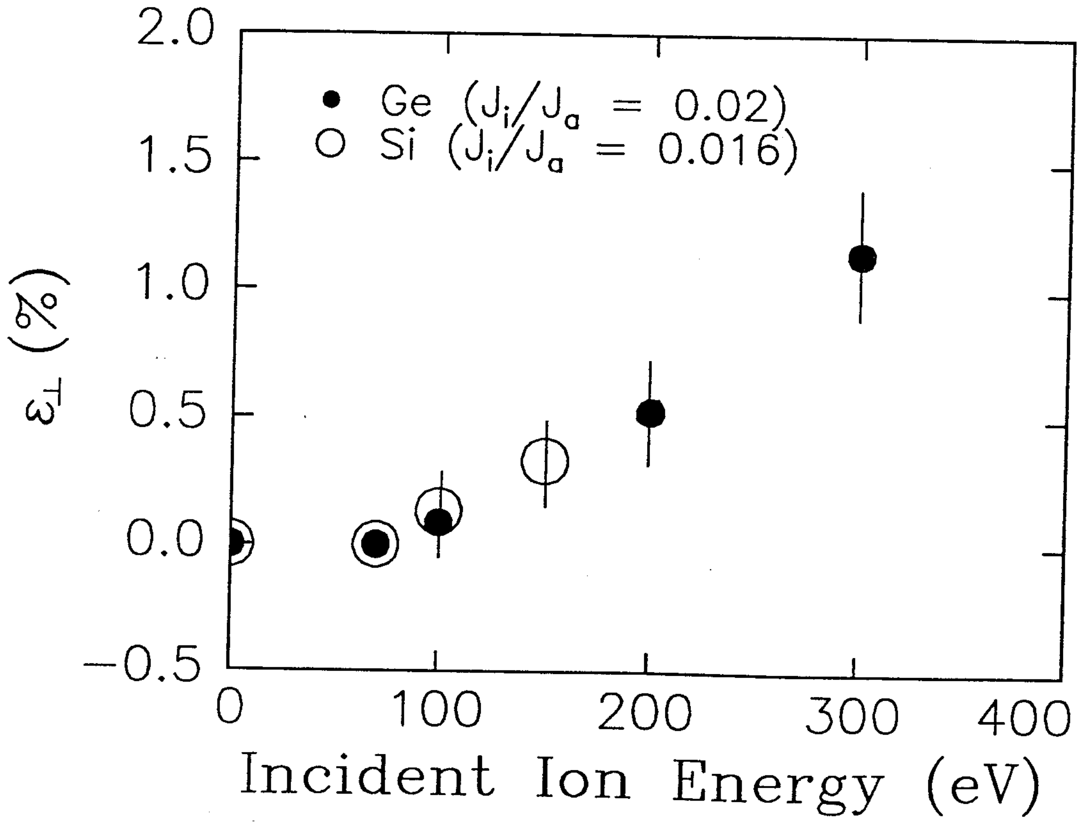

Figure 3.6 Variation of perpendicular strain, $\epsilon_\perp$, with incident ion energy, E_i, (•) for 100 nm thick Ge films grown on (001) Ge by IAMBE at T = 300°C with a fixed ion-to-atom flux ratio, J_i/J_a = 0.02, and (∘) for 100 nm thick Si films grown on (001) Si by IAMBE at T = 350°C with a fixed ion-to-atom flux ratio, J_i/J_a = 0.016. Error bars indicate the uncertainty introduced by possible variations in the ion-to-atom-atom flux ratio, J_i/J_a

ratio at the surface was fixed at $J_i/J_a = 0.02$, and ion energy was fixed at $E_i = 200$ eV. The Arrhenius plot indicates an apparent activation energy of $Q_{sr} = 0.12 \pm 0.05$ eV in the temperature range 200-400° C for the defect dissociation kinetics of the rate-limiting process in strain reduction. The migration kinetics of simple interstitials in Ge are not well understood, but interstitial motion in Si is essentially athermal [22], hence the observation of a non-zero activation energy for defect annihilation suggests that interstitial migration may not be the rate-limiting event. The apparent activation energy Q_{sr} is lower than that estimated for vacancy migration in bulk Ge (0.25 eV) [23], but is similar to the activation energy for grain boundary motion during high energy ion irradiation-induced grain growth in Ge [24]. The weak dependence of strain on the growth temperature has also been observed by the Meyer et al., [25] for ion-beam sputtering deposition of Si_xGe_{1-x} films on Si. The estimated activation energy for strain reduction assuming an Arrhenius behavior are 0.15 eV for $Si_{0.4}Ge_{0.6}$ films and 0.5 eV for $Si_{0.7}Ge_{0.3}$. An interesting trend is that the activation energy increases as the Si concentration in a SiGe film increases which may be explained by the fact that the activation barrier for native point defects migrations in Si (aside from interstitials) is larger than that in Ge [26].

Previous work on Ge epitaxial films grown on (001) GaAs substrate done by Haynes et al., [27] using 40 eV direct Ge beam showed a small expansion of lattice parameter in growth direction. This small free volume expansion was presumably caused by the native defects of Ge, since no inert gas was involved in the deposition process. Zuhr et al., [28] also observed perpendicular strain of ~ 0.15% for an epitaxial Si film grown at 900 K with direct low energy ion beam deposition (20 eV Si^+). These reports suggest the importance of the native point defects in strain modified films. To elucidate the relative roles of native point defects and trapped gas in strain modification. Figure 3.8 shows the Xe concentrations in Ge films grown at $T = 300°C$ with 200 eV Xe^+ at $J_i/J_a = 0.02$ and Ar concentrations in Si films grown at $T = 350°C$ with 100 eV Ar^+ at $J_i/J_a = 0.016$ versus perpendicular strains. If

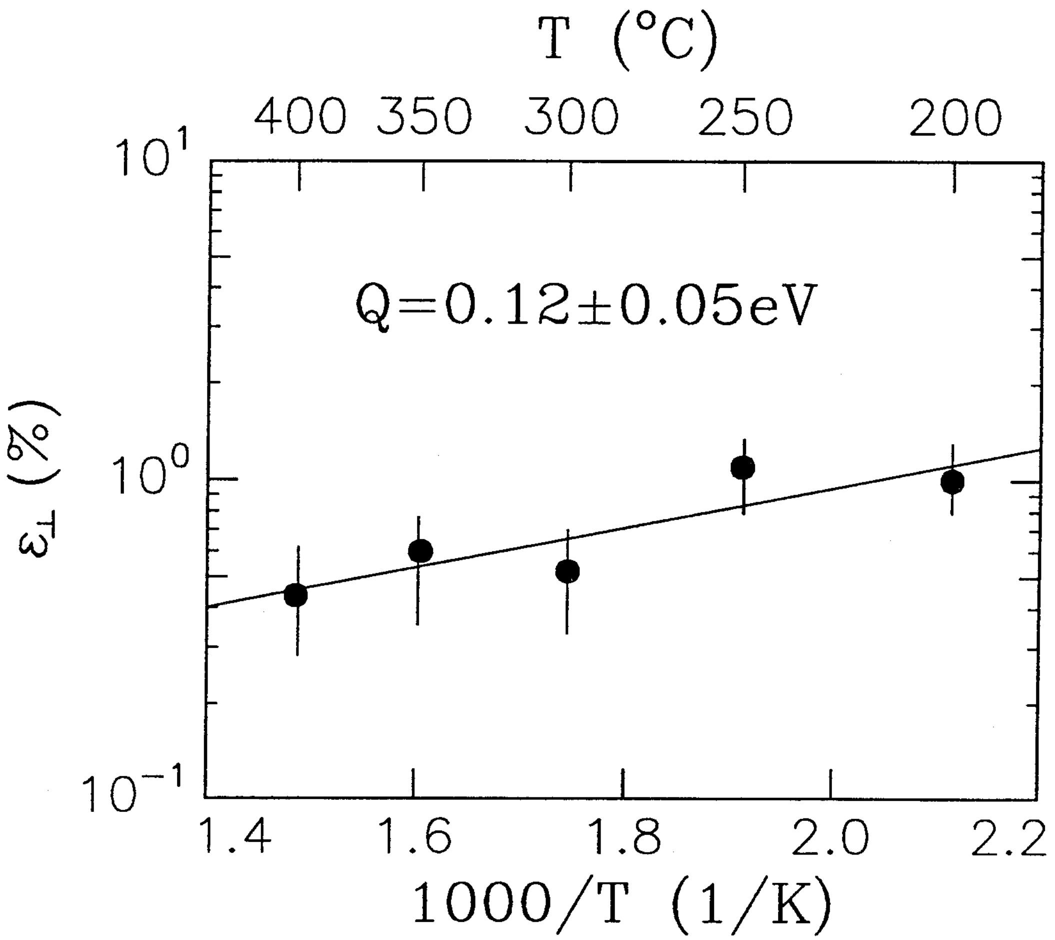

Figure 3.7 Variation of perpendicular strain, $\epsilon_\perp$, with growth temperature for a 100 nm thick Ge films grown on (001) Ge by IAMBE. Ion-to-atom flux ratio at the surface was fixed at $J_i/J_a = 0.02$, and Ar^+ ion energy at 200 eV. Error bars indicate the uncertainty introduced by possible variations in J_i/J_a.

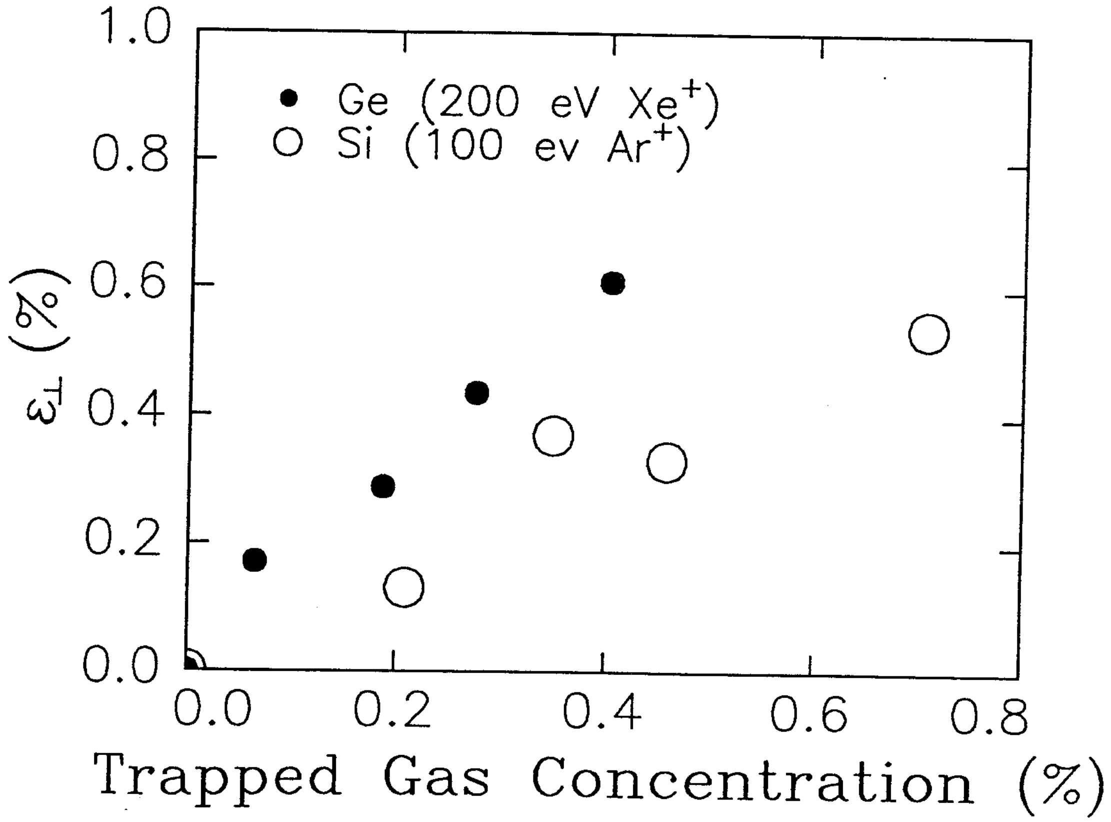

Figure 3.8 The relation of the perpendicular strains of films grown by IAMBE and the trapped inert gas concentration.

we assume that strains are generated only by trapped gas and Vegard's law can be applied for the lattice parameter in this case with $\epsilon_{||} = 0$ and $a_{Ar} = 0.188$ nm , close agreement can be obtained between experimental value and calculated value for Ar in Si films. This suggests that trapped inert gas atoms in target play an important role in strain modification of the IAMBE films.

3.4 Thermal Stability of IAMBE Films

The thermal stability of the films grown by IAMBE was further studied. Figure 3.9 shows a series of X-ray rocking curves of different annealing temperatures for a 100 nm thick Ge film grown on (001) Ge at 300°C with 200 eV Xe^+ at $J_i/J_a = 0.04$. Two important changes were observed, (i) the broadening and (ii) the angular shift of the Bragg peaks of the film. The broadening of the Bragg peaks again indicates that the interactions between the point defects are important and clustering of point-like defects is likely. The strain behavior as a function of annealing temperature of a Ar^+ bombarded Ge film grown at $T = 300°C$ with $J_i/J_a = 0.02$, a Xe^+ bombarded Ge film grown at $T = 300°$ C with $J_i/J_a = 0.04$, and a Ar^+ bombarded Si film grown at $T = 350°$ C with $J_i/J_a = 0.04$ were plotted in Fig 3.10. If the annealing behavior is explained by the segregation of Ar atoms to form bubbles or the aggregation of native point defects to form extended defects, a monotonic decrease in strain with respect to annealing temperature should be expected. This seems to suggest at least two processes of defect annihilation or aggregation occurred during annealing. Furthermore, RBS results also suggest that the Ar concentration in annealed Si samples was practically unchanged in the annealing temperature range. From this observation it was deduced that migration of either Ar atoms or native point defects alone is not able to explain the annealing behavior. The nonmonotonic behavior leads us to speculate that the strain modification is related to Ar-defect complex formation.

The X-ray rocking curves for post-growth isochronal annealing of a 250 nm thick $Si_{.2}Ge_{.8}$ film grown on (001) Ge at $T = 300°C$, 200 eV Ar^+, and $J_i/J_a = 0.03$ are

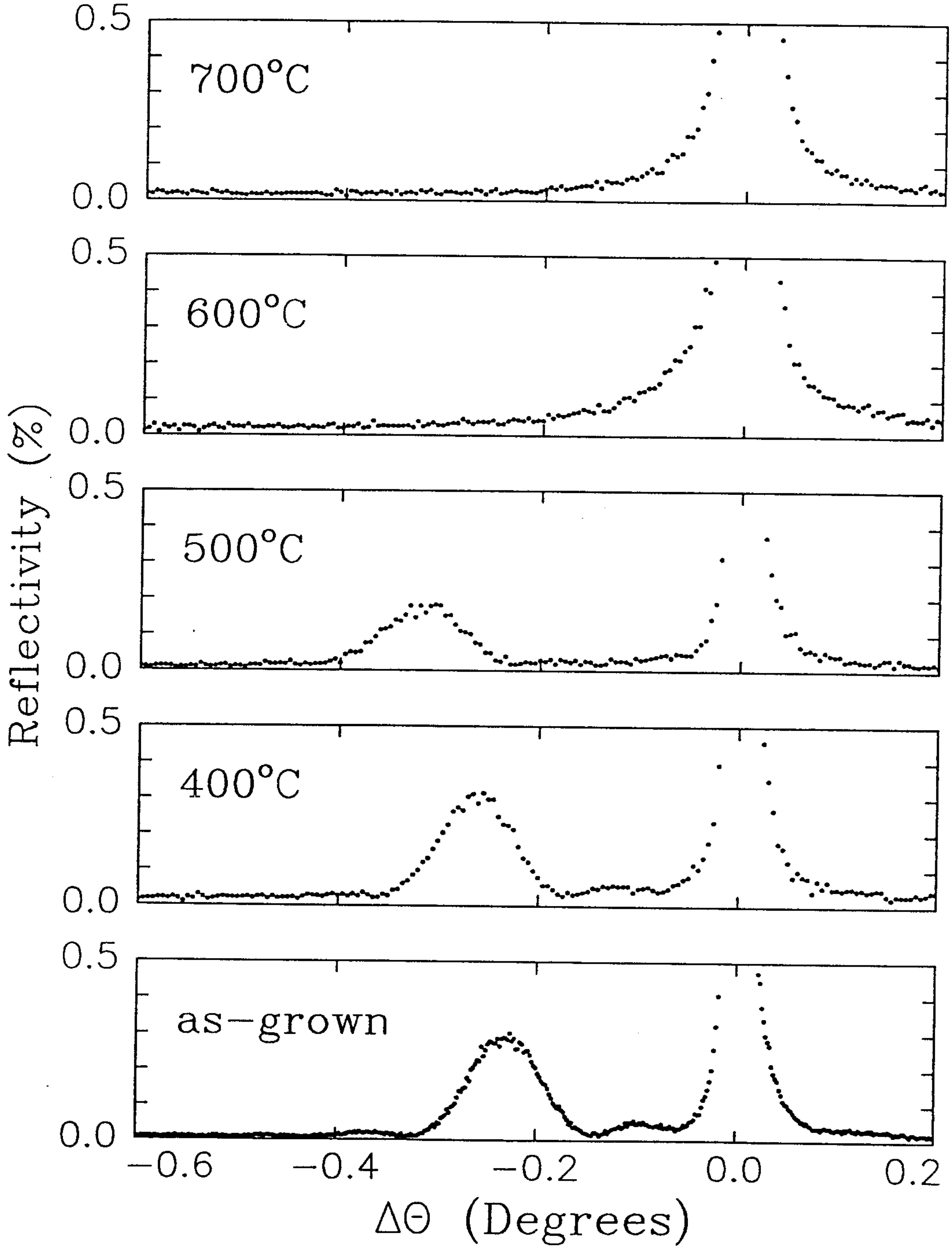

Figure 3.9 X-ray rocking curves for a 100 nm thick Ge film grown on (001) Ge at 300°C with 200 eV Xe^+ at $J_i/J_a = 0.04$ annealed at different temperatures.

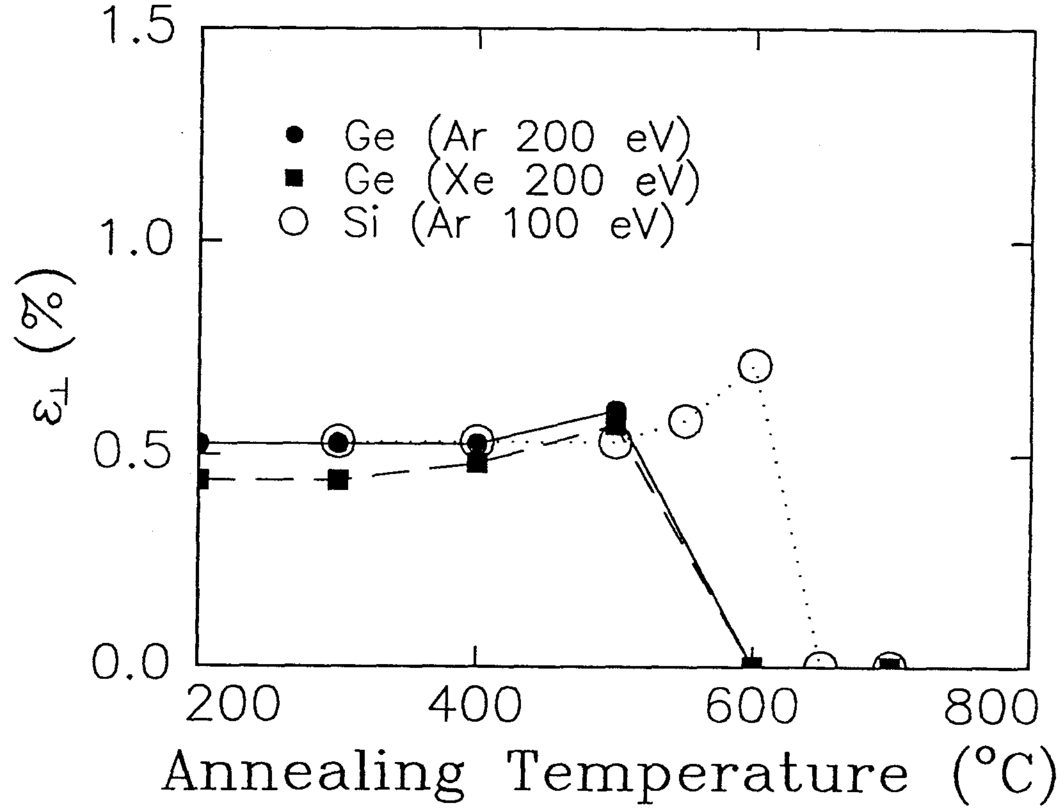

Figure 3.10 Variation of perpendicular strain, $\epsilon_\perp$, with annealing temperature for a 100 nm thick Ge film grown on Ge substrate at growth temperature T = 300°C with (●) 200 eV Ar^+ ions at an ion-to-atom flux ratio $J_i/J_a = 0.02$ and with (■) 200 eV Xe^+ ions at an ion-to-atom flux ratio $J_i/J_a = 0.04$, and for a (○) 100 nm thick Si film grown on Si substrate at growth temperature T = 350°C with 100 eV Ar^+ ions at an ion-to-atom flux ratio $J_i/J_a = 0.04$. The annealing time for Ge films is 1 hour and for Si film is 30 minutes. Uncertainty in measurement is indicated by the size of the symbol. The lines are included as a guide to the eye.

shown in Fig. 3.11(a) and of a 180 nm thick $Si_{0.3}Ge_{0.7}$ film grown on (001) Ge at $T = 300°C$, 200 eV Ar^+, and $J_i/J_a = 0.02$ are shown in Fig. 3.11(b). The Fe - $K_{\alpha 1}$ X-ray source was used and the annealing time for each temperature step was 30 min. The film before annealing were analyzed to be coherent film. The Bragg diffraction peak remains sharp for sample annealed at 400° C and becomes broad and increases in the Bragg angle. The broadening of diffraction peak may be caused by the enhanced diffusion of Si into Ge substrate due to defect motion at annealing temperature or by the formation of defect cluster and dislocation. Different strain relaxation directions in Fig. 3.11(a) and Fig. 3.11(b) were observed. The increase in the Bragg angle which does not exist in the thermal growth sample further indicates that the misfit strain was compensated by the point defects.

Figure 3.12 shows the dependence of perpendicular strain on the Si concentration for Si_xGe_{1-x} grown on (001) Ge for thermal growth case. The IAMBE film can exist in the strain state below fully relaxed strain state. The thermodynamic driving force for the IAMBE film is still toward the fully relaxed equilibrium state, which causes an increase in the Bragg angle. The difference between initial film strain and equilibrium relaxed strain state determines the kinetic annealing path and may cause the films to have different relaxation mechanisms other than the generation of misfit dislocations.

3.5 Conclusions

We have observed changes in Ge and Si_xGe_{1-x} layer strain by up to 1.5% during concurrent molecular beam epitaxial growth and low energy ion bombardment. The films are coherent and dislocation free (in the detection limit of TEM and X-ray diffraction). The dependence of the layer strain on ion energy, ion-atom flux ratio, and growth temperature are consistent with the model in which misfit strain in the film is accommodated by free volume changes associated with the injection of a uniform dispersion of defects consisting of native point defects and/or trapped inert gas atoms. The defects generated by low energy ion bombardment during epitaxial growth are

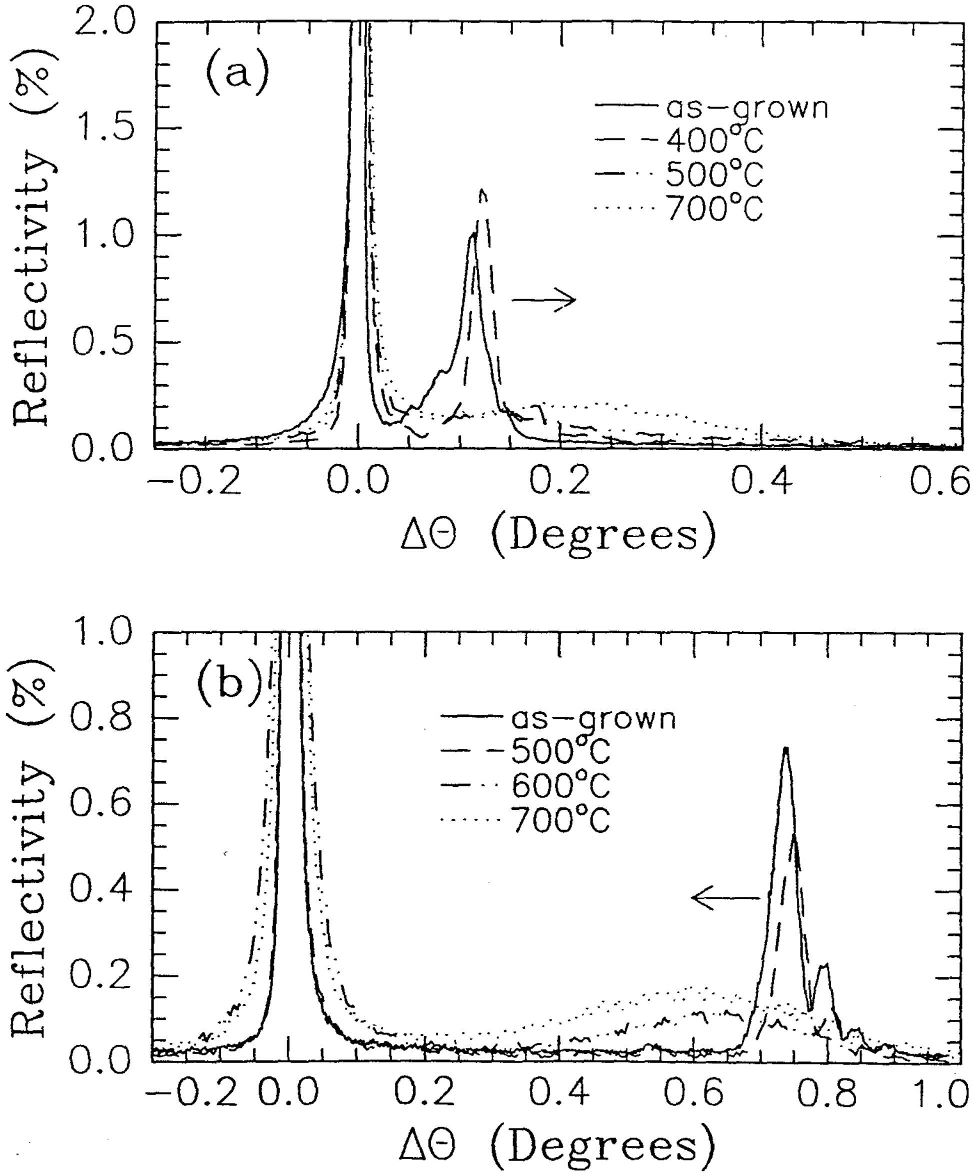

Figure 3.11 The X-ray rocking curves for post-growth isochronal annealing of a 250 nm thick $Si_{.2}Ge_{.8}$ film grown on (001) Ge at T = 300°C, 200 eV Ar^+, and $J_i/J_a = 0.03$ are shown in Fig. 3.11(a) and of a 180 nm thick $Si_{0.3}Ge_{0.7}$ film grown on (001) Ge at T = 300°C, 200eV Ar^+, and $J_i/J_a = 0.02$ are shown in Fig. 3.11(b). The Fe-$K_{\alpha 1}$ X-ray source was used and the annealing time for each temperature step was 30 min.

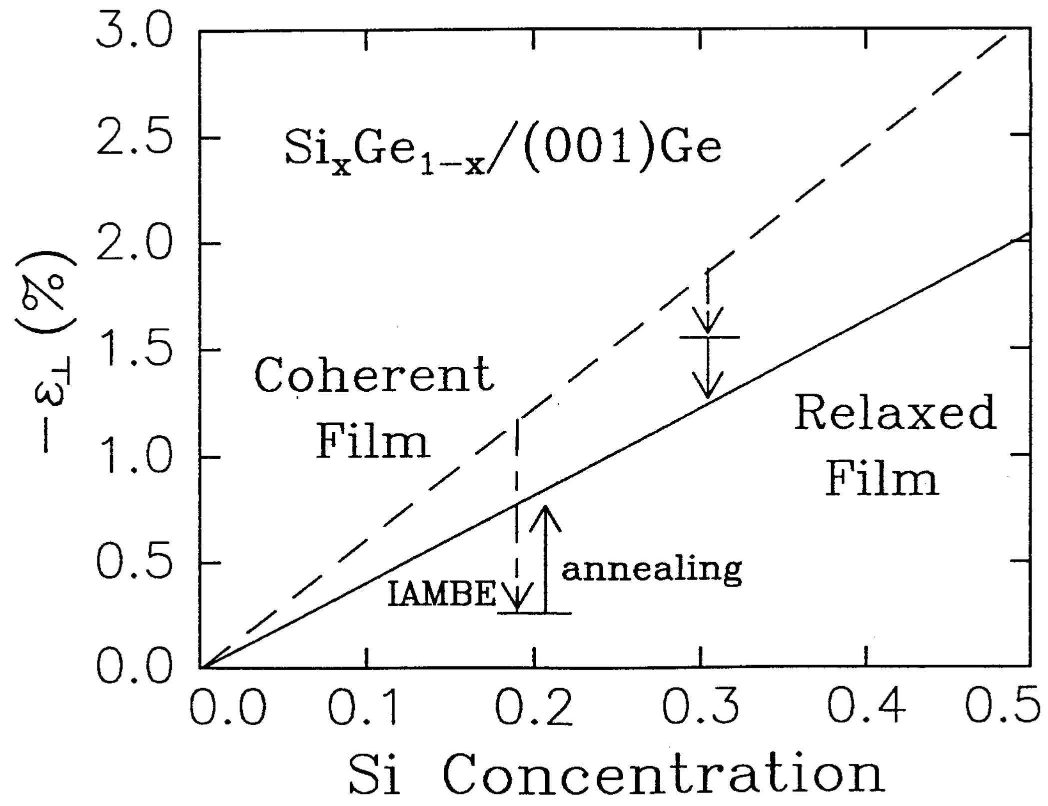

Figure 3.12 Variation of perpendicular strain on the Si concentration for Si_xGe_{1-x} grown on (001) Ge for thermal growth with coherent or fully relaxed case. The dashed lines indicate the changes of strain in the films grown by IAMBE. The arrows indicate the direction of the driving force for strain relaxation upon post-growth annealing.

stable up to 400 – 500° C for Ge films and 500 – 600° C for Si films. A transient increase followed by a decrease in film strain during post-growth annealing was observed. Defect complexes consisting of native point defects and trapped inert gas atom were thought to be the main factor in producing the strain changes in the films grown by IAMBE. The kinetic path for strain relaxation of Si_xGe_{1-x} on (001) Ge depends on the relative amount of the total misfit strain accommodated by the IAMBE.

References

[1] S.R. Kasi and J.W. Rabalais, Rad. Effects. **112**, 119 (1990).

[2] B.W. Dodson, Crit. Rev. Solid State Mater. Sci., **16**, 115 (1990).

[3] B.W. Dodson, J. Vac. Sci. B **5**, 1393 (1987).

[4] W.R. Burger and R. Reif, J. Appl. Phys. **62** 4255 (1987).

[5] J.E. Greene,*CRC Critical Reviews in Solid State and Materials Science*, **2**, 47 (1983).

[6] J.Y. Tsao, E. Chanson, K.M. Horn, D.K. Brice, and S.T. Picraux, Nucl. Instr. and Meth. B **39**, 72 (1989).

[7] E. Chason, J.Y. Tsao, K.M. Horn, and S.T. Picraux, J. Vac. Sci Technol. B **7**, 332 (1989).

[8] E. Chason, J.Y. Tsao, K.M. Horn, S.T. Picraux, and H.A. Atwater, J. Vac. Sci. Technol. A **8**, 2507 (1990).

[9] K.M. Horn, J.Y. Tsao, E. Chason, D.K. Brice, and S.T. Picraux, J. Appl. Phys. **69**, 243 (1991).

[10] C.-H. Choi, L. Hultman, and S.A. Barnett, J. Vac. Sci. Technol. A **8**, 1587 (1990).

[11] C.J. Tsai, H.A. Atwater, and T. Vreeland, Appl. Phys. Lett. **57**, 2305 (1990)

[12] C.J. Tsai, P. Rozenak, H.A. Atwater, and T. Vreeland, J. Cryst. Growth. **111**, 931 (1991).

[13] P.C. Zalm and L.J. Beckers, Appl. Phys. Lett. **41** 167 (1982).

[14] T. Itoh, T. Nakamuru, M. Muromachi, and T. Sugiyama, Jpn. J. Appl. Phys. **16**, 553 (1977).

[15] C. Schwebel, F. Meyer, G. Gautherin, and C. Pellet, J. Vac. Sci. Technol. B **4**, 1153 (1986).

[16] F. Meyer, C. Schwebel, C. Pellet, G. Gautherin, A. Buxbaum, M. Eizenberg, abd A. Raizman, Thin Solid Films **184**, 117 (1990).

[17] T. Ohmi, K. Hashimoto, M. Morita, and T. Shibata, J. Appl. Phys. **69**, 2062 (1991).

[18] W.J. Bartels, J. Vac. Sci. Technol. B **1**, 338 (1983).

[19] C.R. Wie, T.A. Tombrello, and T. Vreeland, J. Appl. Phys. **59**, 3743 (1986).

[20] D.K.Brice, J.Y. Tsao and S.T. Picraux, Nucl. Instrum and Methods **44**, 68-78 (1989).

[21] P.H. Dederichs, J. Phys. F : Metal Phys. **3**, 471 (1973).

[22] A. Seeger and K.P. Chik, Phys. Status Solidi **29** 455 (1968).

[23] J.A. Vanvechten, Phys. Rev. B **10**, 1482 (1974).

[24] H.A. Atwater, C.V. Thompson, and H.I. Smith, J. Appl. Phys. **64**, 2337 (1988).

[25] F. Meyer, M. Zafrany, M. Eizenberg, R. Beserman, C. Schwebel, and C. Pellet, J. Appl. Phys. **70**, 4268 (1991).

[26] M. Lannoo and J. Bourgoin, "Point Defects in Semiconductors I";(Springer-Verlag, Berlin, Heidelberg, 1981).

[27] T.E. Haynes, R.A. Zuhr, S.J. Pennycook, B.C. Larson, and B.R. Appleton, J. Vac. Sci. Technol. A **7**, 1372 (1989).

[28] R.A. Zuhr, B.R. Appleton, N. Herbots, B.C. Larson, T.S. Noggle, and S.J. Pennycook, J. Vac. Sci. Technol. A **5**, 2135 (1987).

Chapter 4

A Kinetic Model of Defect Incorporation Process for Ion-Assisted Molecular Beam Epitaxy

4.1 Introduction

During ion-assisted molecular beam epitaxy, injection of point-like defects into the sub-surface region results in entrapment of defects. When low energy ion bombardment is combined with epitaxial growth at a constant rate, the resulting uniform dispersion of point-like defects leads to uniformly strained epitaxial layers. The linear dependence of the strain on the ion-to-atom flux ratio [1, 2] suggests that defect recombination was consistent with first-order kinetics and that the major sink for defect annihilation was the free surface. Following these assumptions, we can conceptualize the steady-state defect concentration as a simple moving boundary diffusion problem using a continuum approximation. A multi-site multiply-activated migration model of low energy ion beam enhanced dopant incorporation using surface, bulk, and three intermediate sites with different activation barriers has been proposed by Ni et al., [3]. A qualitative comparison of the present work with this model is also discussed. The simple moving boundary diffusion model with single activation energy was also generalized to multiply-activation migration processes. The present model was also combined with the ion peening model [4] to further predict the dependence of the defect concentration on the ion energies and other material properties.

4.2 Moving Boundary Diffusion Model with Single Activation Energy

We consider the growth surface to be a one dimensional system in a frame moving with velocity v, by substituting $x + vt$ for x into the diffusion equation and assuming the diffusivity of the defects at the growth temperature, D, is independent of concentration. We have

$$\frac{dn}{dt} = D\frac{d^2n}{dx^2} - v\frac{dn}{dx} + S, \tag{1}$$

where n is the defect concentration, x is the distance measured from the growth surface, v is the growth rate, and S is the source function representing the defect profile generated by the ion beam. We are interested in the steady-state solution, $dn/dt = 0$. Equation (1) is basically the same as the diffusion equation used by Myers-Beaghton [5] for studying the diffusion and adatom interactions during epitaxial growth on a vicinal surface without a recombination term. We choose two simple source functions, (i) a step function and (ii) a Gaussian function, as shown in Fig. 4.1. The choice of the step function is to illustrate the functional dependence of the important parameters in the IAMBE process. We define a projected defect production range, R_p, for the step source function above which the defect production rate can be ignored. In the Gaussian source function, ΔR_p is the standard deviation of the projected defect production range. The quantities R_p and ΔR_p have the usual meaning when we deal with the dopant incorporation, i.e., R_p is the projected range and ΔR_p is the range straggling. We also define $\alpha = v/D$. For purposes of comparison of these two source functions, we fixed the total defects flux (per unit surface area per unit time) and set it equal to K. The boundary conditions used in solving the problem for the step function are $n(0) = 0$, $n(\infty) = C$, n is continuous at position R_p, and the slope of n at position R_p is also continuous and for the Gaussian function they are $n(0) = 0$, $n(\infty) = C$, and the slope of n at $x = \infty$ is 0. The solutions for the final concentration in these two cases are the following:

$$\begin{aligned} (i) \quad C &= \frac{K}{v} + \frac{K}{\alpha R_p v}(e^{-\alpha R_p} - 1) \\ (ii) \quad C &= \frac{K}{v}\{1 - \frac{e^{-\alpha R_p + \alpha^2 \Delta R_p^2/2} erfc(-\frac{R_p}{\sqrt{2}\Delta R_p} + \frac{\alpha \Delta R_p}{\sqrt{2}})}{[1 + erf(\frac{R_p}{\sqrt{2}\Delta R_p}]}\}. \end{aligned} \tag{2}$$

For the step defect distribution, the final defect concentrations in the growth rate-limited regime, $\alpha R_p \gg 1$, are proportional to K/v, while in the diffusion-limited

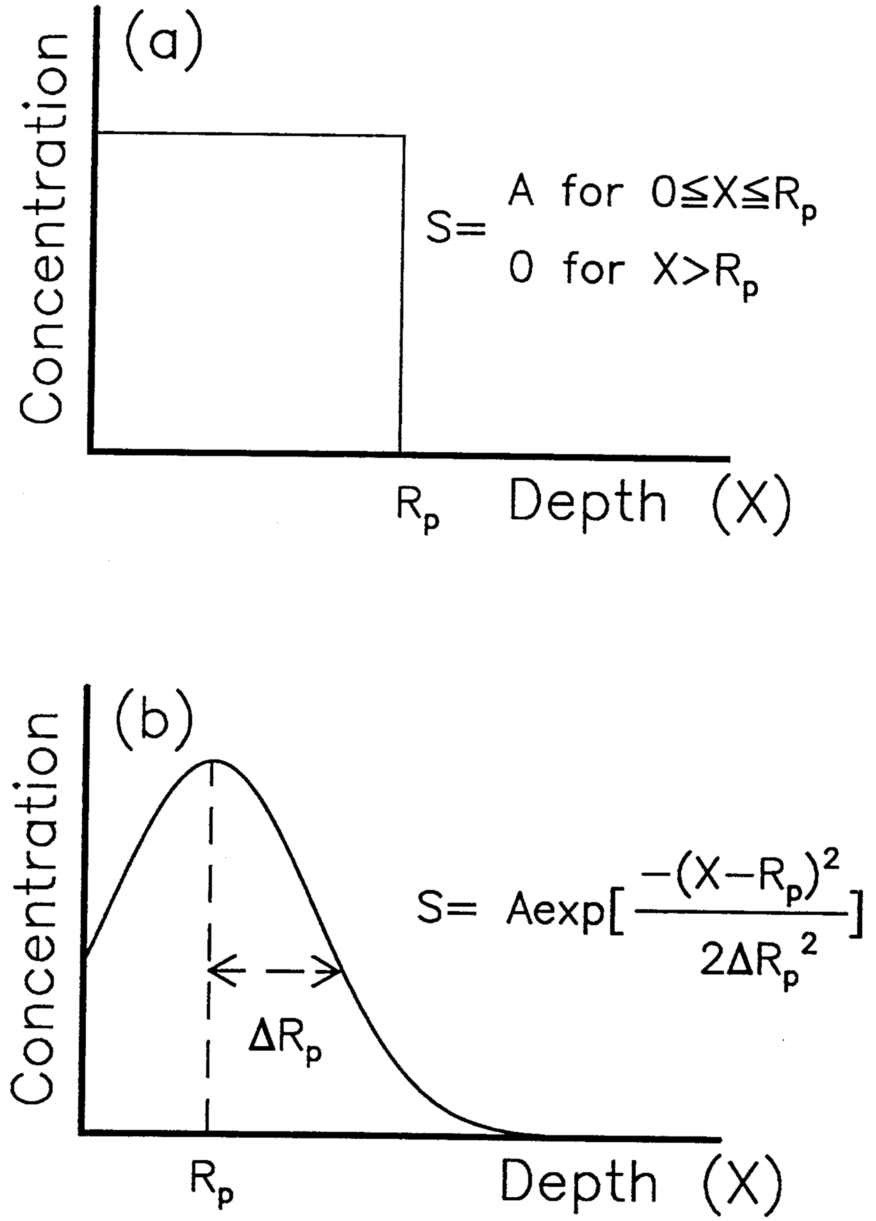

Figure 4.1 Defect production profiles used for analytic solution of equation (1) with total defects per unit area per unit time. (a) A step function with defect production range R_p, (b) a Gaussian with defect production range R_p and standard range deviation ΔR_p.

regime, $\alpha R_p \ll 1$, the final concentrations are proportional to KR_p/D. For the Gaussian defect distribution, the final concentration C can be proved to be convergent and the criterion for achieving the growth-rate limited regime depends on the value of $M = \frac{R_p}{\sqrt{2}\,\Delta R_p}$. The sufficient condition for the growth rate limited regime is $\alpha R_p \gg 2M + M^2$, while for $M \gg 1$, the exponential term in equation (2-ii) will dominate the approach of the final concentration to K/v, the condition becomes $\alpha R_p \gg 1$. The condition states that, for a fixed defect production range, broader defect production profiles require higher growth rates to trap all the defects. Note that K is proportional to the ion flux. Figure 4.2 shows the final concentrations as a function of αR_p for the step function and the Gaussian functions with $M = 0.707$ and $M = 2.828$. The final defect concentration of a step source function never reaches unity because a certain portion of the defects can be classified as surface defects. This clearly shows that, in the IAMBE processes, the definition of surface defects (defects that are generated in the substrate and escape out of the substrate), and bulk defects (defects that are generated and trapped in the substrate), are not only related to the diffusivity of defects and the defect production profile but also to the growth velocity. Let us use the step function case to illustrate the definition of the surface defects and bulk defects in the IAMBE process. The portion of bulk defects is defined as the ratio of the final retained defects per unit area to the defects generated per unit area by the ion beam. The total number of defects per unit area generated by the ion beam in the range of $0 - R_p$ is KR_p/v and the total number of final retained defects per unit area within the same range is CR_p, thus the portion of bulk defects is $C \cdot v/K$ and the portion of surface defects is $1 - (C \cdot v/K)$. Thus, the curves in Fig. 4.2 also define the portion of bulk defects as a function of αR_p.

The model was compared with the strain in the films grown by IAMBE. A simple analysis of the strain modification was based on the assumption that the strains measured from the X-ray rocking curve analyses were proportional to the product of defect concentration and the defect associated volume changes. Table 4-I lists

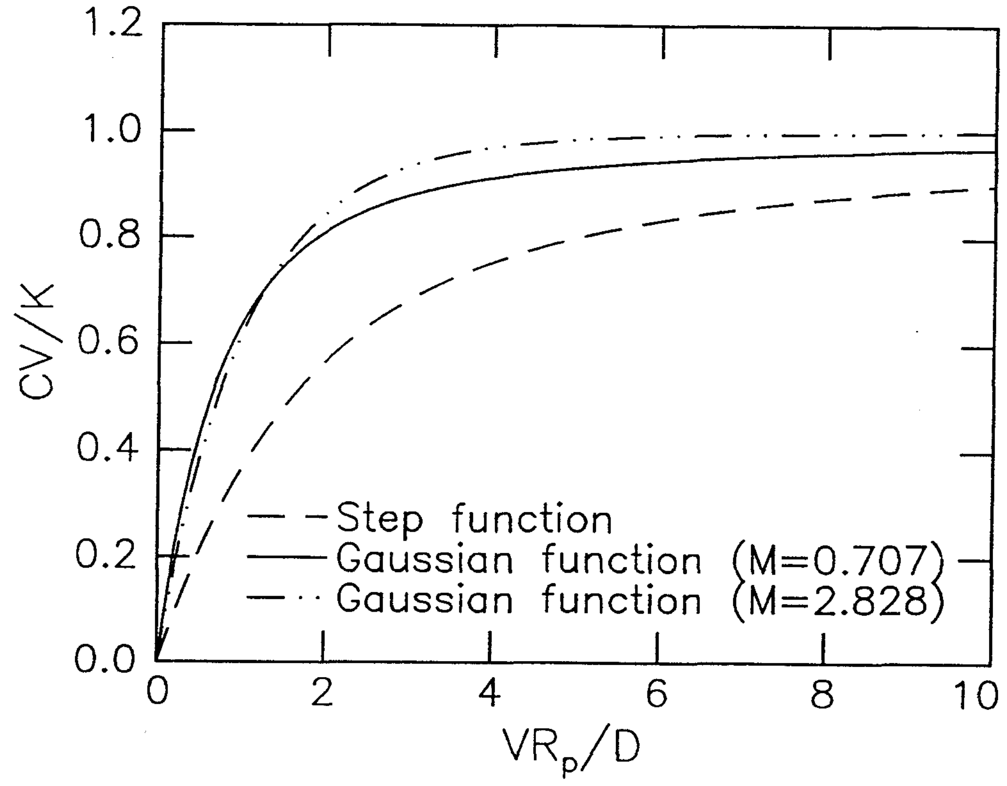

Figure 4.2 The dependence of the final normalized defect concentrations and normalized bulk defects on the αR_p for a step source function, a Gaussian source function with $\frac{R_p}{\sqrt{2}\Delta R_p} = 0.707$, and a Gaussian source function with $\frac{R_p}{\sqrt{2}\Delta R_p} = 2.828$.

Growth Rate (nm/s)	Ion Flux μA/cm^2	Ions/Atoms	Strain (%)	Ions
0.60	4.20	0.010	0.20	Ar$^+$
0.30	4.68	0.022	0.53	Ar$^+$
0.35	6.45	0.026	0.95	Ar$^+$
0.25	6.13	0.035	0.82	Ar$^+$
0.24	7.58	0.045	1.57	Ar$^+$
0.30	4.84	0.023	0.17	Xe$^+$
0.20	5.97	0.042	0.44	Xe$^+$
0.17	8.06	0.067	0.29	Xe$^+$
0.10	9.68	0.137	0.61	Xe$^+$

Table 4-I Growth conditions of IAMBE Ge films on Ge (001) substrate with concurrent 200 eV Ar$^+$ ion beams and 200 eV Xe$^+$ ion beams at 300°C.

data associated with Ge films grown by the IAMBE processes. In Chapter 3, Figure 3.4 shows the linear dependence of the strain on the ion-atom flux ratio, J_i/J_a. If one ion produces one defect, J_i/J_a will be the same as K/v. In general, this is not necessarily the case for defect incorporation processes. Thus, for defect incorporation processes, J_i/J_a which is a directly measurable quantity, was used. We note that in these growth conditions the strains are proportional to the ion-to-atom flux ratio only, and not the absolute ion flux. This suggests that the growth conditions are in the growth rate-limited regime since the final concentration in this regime is proportional to K/v. We can find the upper limit of the defect diffusivity taking the growth rate as 0.1 nm/s, the defect production range estimated from the TRIM calculation is on the order of 1 nm for the above ion energy condition , thus, $D \ll 10^{-15}$ cm^2/s for growth conditions to be in the growth rate limited regime. In previous experiments, we estimated an apparent activation energy for strain annihilation *obtained from the* *dependence of the strains on the growth temperatures* to be $Q = 0.12$ eV [1]. If we use this activation energy and put it into the condition $D \ll 10^{-15}$ cm^2/s, we find that the pre-exponential factor, at 600°K, is $D_0 \ll 10^{-14}$ cm^2/s. This value implies a diffusion site density which is too low to be consistent with ordinary bulk thermal diffusion, and thus suggests the apparent activation energy obtained from the growth temperature dependence is *not* the true activation energy for a single rate-limited bulk defect diffusion process. This estimated activation energy may instead reflect the thermal spike energy deposited by the bombarding ions.

4.3 Cascade-Assisted Diffusion

An energetic particle striking a target will generate a cascade. Cascade recovery consists in principle of two parts, (i) athermal recovery and (ii) thermal recovery. The athermal recovery is due to the fact that there are both vacancies and interstitials inside the cascade region. The thermal recovery of the cascade is due to the local heating (thermal spike) which provides thermal energy to the defects. The fact that (i) the defects left after the events of cascade recovery are stable at the growth temperature and (ii) nonetheless we measured a very low apparent activation energy, suggests that a possible explanation for the apparent activation energy in the growth temperature dependence of the strain annihilation is related to cascade-assisted defect diffusion. The final defects generated by the ion beam have an activation energy for movement much larger than the apparent activation energy. The defects have a good probability to move when they are struck by a cascade with a time period of the lifetime of the cascade.

The thermal spike concept has been used in sputtering and ion mixing. Several attempts at calculation of the temperature evolution inside a cascade region [6, 7, 8] have been made; we follow Vineyard's calculation of the temperature evolution inside a cylindrical thermal spike [8] which has been successfully applied to explain the ion beam mixing data [9]. It is important to remember the basic assumptions of the thermal spike model that the heat conduction equation is valid over the microscopic region and short time scale involved. The medium is considered to have a thermal conductivity, κ, a heat capacity, C_h, and a density ρ. The major contribution of the spike induced jumps of the defects is from the core region at the beginning of the time, thus, for simplicity and to a first order approximation, we assume that the heat capacity and the thermal conductivity are temperature independent at high temperature. Consider the liberation of the heat per unit length, F_d, at a point at the origin at time, $t = 0$, with the initial medium temperature equal to the substrate growth temperature, T_g, the temperature $T(s,t)$ at position s and time t corresponding to the solution for the heat conduction equation is

$$T(s,t) = \frac{F_d}{4\pi\kappa t}\exp(-\frac{\rho C_h s^2}{4\pi\kappa t}) + T_g. \tag{3}$$

The number of jumps per unit time contributed from the spike for a defect with a migration activation energy, Q_m, and an attempt frequency, ν, is

$$\eta = J_i\nu\int_0^\infty 2\pi s ds\int_{t_0}^\infty \{\exp(-\frac{Q_m}{k_B T(r,t)}) - \exp(-\frac{Q_m}{k_B T_g}\}dt, \tag{4}$$

where J_i is the ion flux and k_B is the Boltzmann constant. The initial width of the cylindrical spike is determined by the starting time t_0. This cylindrical spike is assumed to have influence on the subsurface region only. We performed numerical integration of equation (4) with parameters, $F_d = 150$ eV/nm estimated from TRIM simulation of 200 eV Ar$^+$ bombarded Ge, $J_i = 3 \times 10^{13}$ ions/cm^2-s, $C_h\rho = 27$ J/mole-°K is the heat capacity for liquid Ge taken from reference [10], and $\kappa = 0.014$ watt/cm−°K, as suggested by Thompson and Nelson [11]. The adjustable parameters are the activation energy for the defect migration and the starting time, t_0, which corresponds to the initial distribution of the deposited energy [6] or the time needed to establish the Maxwell-Boltzmann distribution, i.e., local thermal equilibrium, which ranges between 10^{-12} and 10^{-13} s [12]. Figure 4.3 shows the evolution of the spike temperature over time and space using the parameters mentioned above. The duration of the spike is in the order of 5×10^{-12} s and the distribution of the

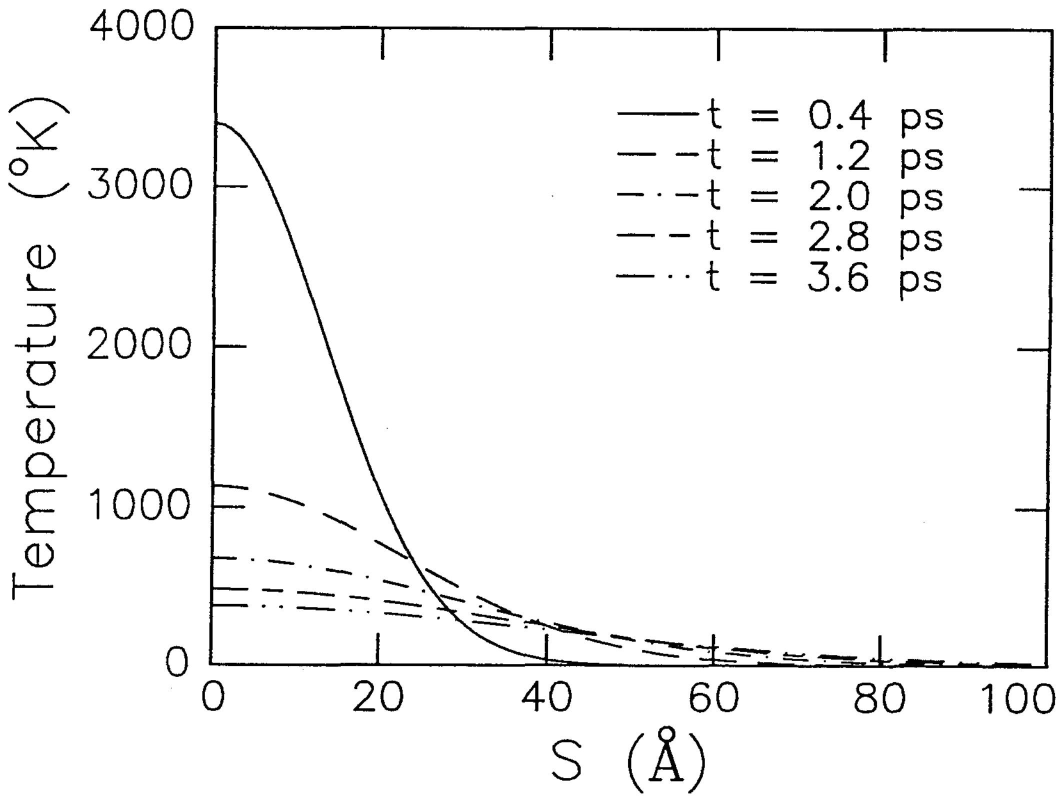

Figure 4.3 The temperature evolution inside a cylindrical spike. For calculation parameters see text.

heat is confined in a 5 nm diameter region. The spike will have little effect on the defects that lies outside of the region.

The effective diffusivity in IAMBE process can be defined as $D = D_0(\eta/\nu + \exp(-Q_m/k_B T_g))$ Figure 4.4 shows three curves of effective diffusivity with (i) $Q_m =$ 1.5 eV and $t_0 = 4 \times 10^{-13}$ s, (ii) $Q_m = 2$ eV and $t_0 = 4 \times 10^{-13}$ s, and (iii) $Q_m = 2.5$ eV and $t_0 = 4 \times 10^{-13}$ s. The starting time, $t_0 = 4 \times 10^{-13}$ s, is in the range of the cascade duration [12] and consistent with molecular dynamics simulations [13]. The apparent activation in the first curve is $Q_a = 0.08$ eV, in the second curve is $Q_a = 0.1$ eV, and in the third curve is $Q_a = 0.12$ eV. The experimental data points were the growth temperature dependence of strains of Ge films grown with 200 eV Ar^+ ion bombardment and ion-to-atom flux ratio, $J_i/J_a = 0.02$. We can define a transition temperature, T_{tr}, above which the defect diffusion is thermally activated and below which the defect diffusion is cascade-assisted. The transition temperature is written as

$$T_{tr} = \frac{Q_m}{k_B}(\ln(\frac{\nu}{\eta}))^{-1}. \tag{5}$$

As we can see from Fig. 4.4 that the transition temperature for the third curve is about 800K. In previous work, we find that no strain can be detected for 200 eV Ar^+ bombarded Ge films with ion-to-atom flux ratio, $J_i/J_a = 0.02$ at growth temperatures above 800K [1] and that the defects are mobile at 800K upon post growth annealing of the strained films [2]. A fair agreement between the experimental observation and the calculation was found to be $Q_m = 2 - 2.5$ eV and $t_0 = 4 \times 10^{-13}$ s. The corresponding pre-exponential factor is 2.32×10^{-16} cm^2/s which also agrees with the condition for the growth-rate limited regime. Note that the choice of t_0 and Q_m is not unique. As t_0 decreases the apparent activation energy and T_{tr} decrease and when Q_m increase the apparent activation energy and T_{tr} increase. Although the results of the calculation of the spike evolution is not exact due to the assumptions made and owing to the non-unique choice of t_0 and Q_m, the agreement between the experimental observation and this simple calculation suggests that the energy

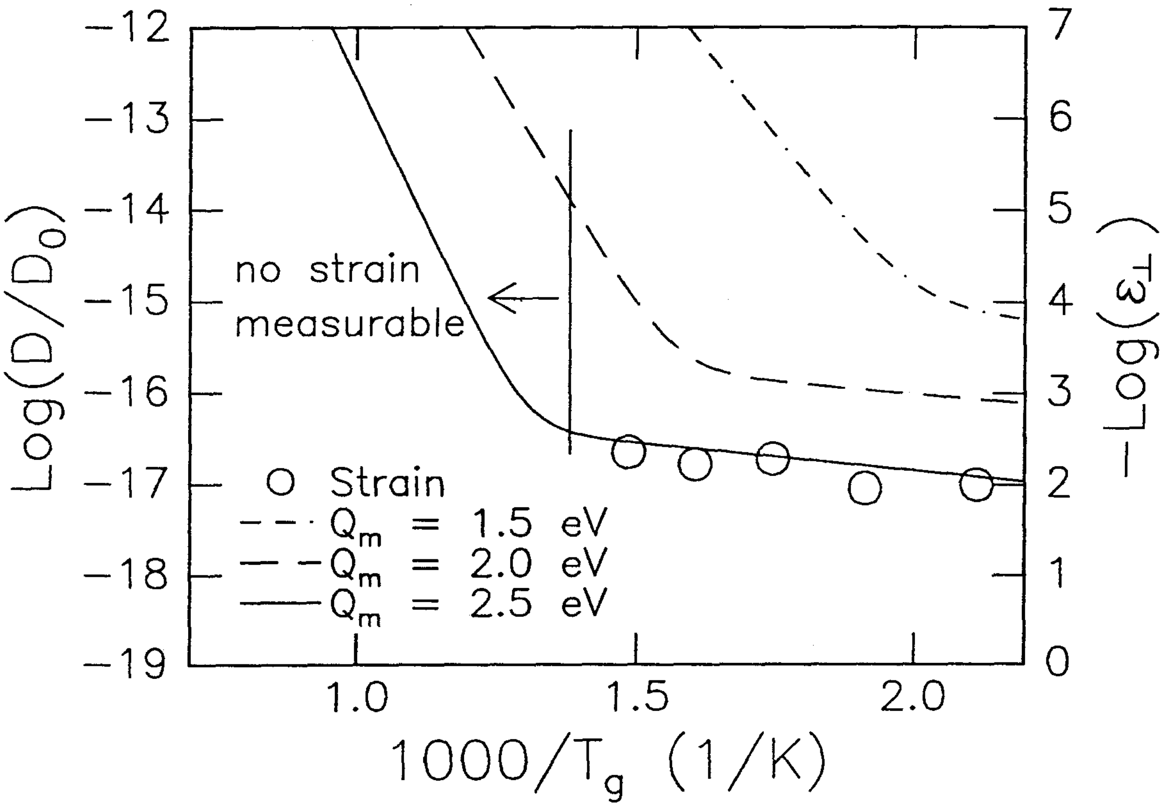

Figure 4.4 Normalized diffusivity as a function of temperature for different activation energies of defect migration. All curves are calculated with $t_0 = 4 \times 10^{-13}$ s, $F_d = 150$ nm/s, and $J_i = 3 \times 10^{13}$ ions/cm^2-s. The experimental data points were the growth temperature dependence of strains of Ge films grown with 200 eV Ar$^+$ ion bombardment and ion-to atom flux ratio, $J_i/J_a = 0.02$.

deposited by the energetic particle plays an important role in the defect diffusion process. Equation (4) has been numerically integrated for finite T_g by Gilmore et al., [14] to investigate the contribution of the thermal spike effect on the adatom surface diffusivity during ion beam assisted deposition of Au on NaCl using 100 eV Ar^+ ions. They concluded that the thermal spike would produce a negligible effect on adatom diffusivity for typical adatom densities. In contrast to the calculation of Gilmore et al., [14] we find that the thermal spike has a profound effect on the apparent activation energy of defect diffusion in spite of the small effective diffusivity.

Meyer et al., [15] have also obtained low activation energies, 0.15 eV for 800 nm $Si_{0.4}Ge_{0.6}$ film and 0.5 eV for 300 nm $Si_{0.7}Ge_{0.3}$ film grown on Si (100) by ion-beam sputtering deposition, from the growth temperature dependence of film stresses. Since the film thicknesses are above the critical thicknesses for dislocation formation, the films are expected to be at least partially relaxed. The low activation energy observed by Meyer et al., suggests that the major driving force for strain relaxation is the defect diffusion and the cascade-assisted diffusion is the dominant mechanism for defect migration.

We note also that Windischmann has provided a detail analysis of the ion peening model to explain the intrinsic stresses of thin films prepared by the ion beam sputtering [4]. The ion peening model which is based on the knock-on linear cascade theory of transmission sputtering proposed by Sigmund [16] can explain the intrinsic stresses for a variety of films deposited at a temperature where the defect mobility is sufficiently low that the growth conditions can be classified to be in the growth-rate limited regime and can provide a basis for the description of the total defect flux, K. The main problem involved in the ion peening model is that the model does not clearly specify the fraction of the athermal recombination of the defects generated by ion beams.

4.4 Ion Incorporation

The continuous moving boundary diffusion problem used in this analysis of defect-related strain produces parametric dependences that are qualitatively similar to the discrete multi-site model presented by Ni et al., [3]. Hence it seems reasonable to compare this analysis with the discrete model, which can be done by setting $K = \gamma J_i$ for dopant incorporation where γ is the incorporation coefficient which is the fraction of the ions which rest on or inside the target. The incorporation coefficient for fixed ion species and substrate is a function of ion energy and substrate temperature. In the case of Sb ion incorporation into Si, the incorporation probability is assumed to be unity for the all ion energies and for all substrate temperatures. We can also generalize the moving boundary diffusion model by additional terms in equation (1) which act to model dopant segregation. In the temperature regime used in the experiments of Ni et al., [3], the diffusivity of the dopant at 900°C for Sb atoms in Si is comparable to vR_p, thus the dopant incorporation probability (Cv/J_i, the same as the definition of the bulk defects) will rise quickly at low growth rate and saturate. Figure 4.5 shows the data of incorporation probability of Sb atoms as a function of Si growth rate taken from reference [3] and the calculated curves using the moving boundary diffusion model. In the fitting process, first of all, we find that the calculated curves cannot fit the experimental data with a single activation energy. We follow the description in reference [3] to chose the Sb projected ranges for different energies, $R_p = 0.25$ nm for 100 eV ions, $R_p = 0.53$ nm for 200 eV ions, and $R_p = 0.81$ nm for 300 eV ions, and fix $\Delta R_p/R_p = 0.3$. The activation energies at 900°C obtained from 100 eV Sb ion beam data is $D = 3.0 \times 10^{-15}$ cm^2/s, from 200 eV Sb ion beam data $D = 1.4 \times 10^{-16}$ cm^2/s, and from 300 eV Sb ion beam data $D = 8.1 \times 10^{-16}$ cm^2/s. Note that the diffusivities approach the bulk value as ion energies increase. The diffusivity values obtained lie in the range of those assumed for the third and fourth layers in Ni's model. The phenomenon of lower activation energy in the sub-surface region suggests that the multi-site model is necessary for dopant incorporation using low energy ion beams.

The temperature dependence of the dopant incorporation has two cases (i) the

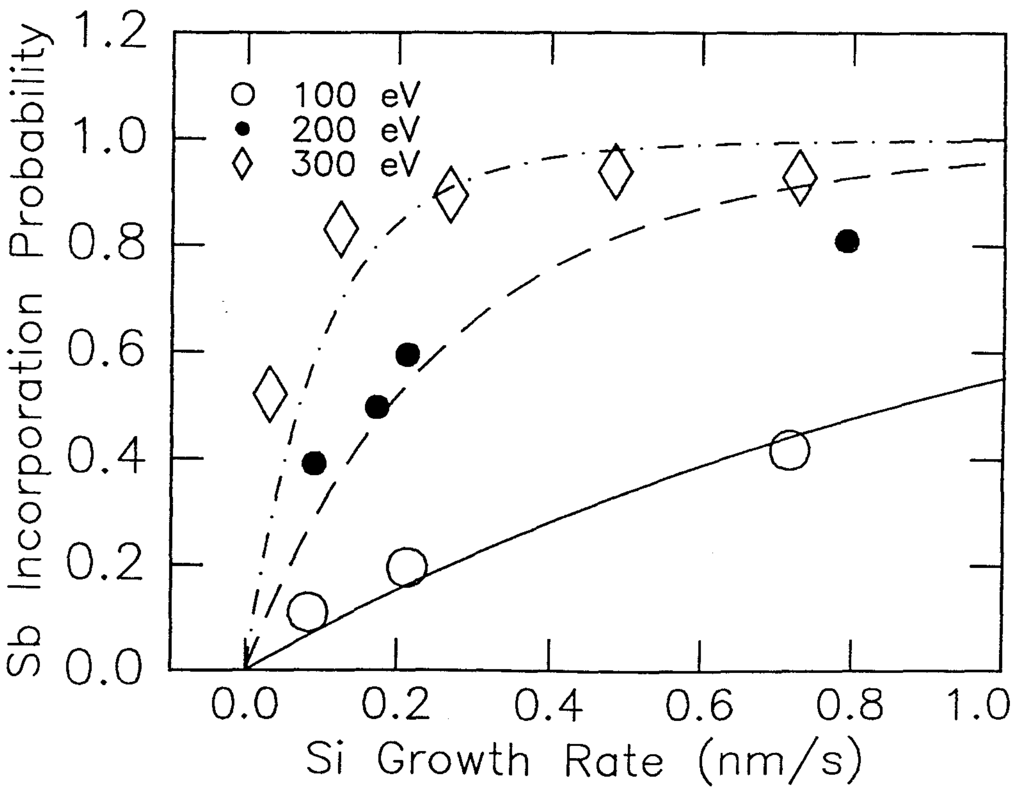

Figure 4.5 Sb ions incorporation probability as a function of ion energy and the Si growth rate. The experimental data are taken from reference [3]. The curves are calculated from equation (2-ii) with fixed $\frac{R_p}{\sqrt{2}\Delta R_p} = 2.357$ used in reference [3]. The parameter for the solid line is $R_p/D = 0.8$ s/nm, for the dashed line $R_p/D = 3.7$ s/nm, and for the dotted line $R_p/D = 10$ s/nm.

transition temperature between thermal diffusion and cascade-assisted diffusion lied in the growth rate-limited regime and (ii) the transition temperature lied in the diffusion-limited regime. From equation (4) and (5), the number of jumps per unit time contributed from the spike for a defect is proportional to the ion flux, J_i, thus, the transition temperature increases as the ion flux increases. For all other growth parameters fixed except the ion flux, case (i) corresponds to a low incoming ion flux and case (ii) corresponds to a high incoming ion flux. In case (i), the effective diffusivity dominated by the cascade-assisted diffusion at low temperature is so small such that $\alpha R_p >> 1$. This indicated that the temperature dependence of the dopant incorporation would not be perturbed by the cascade-assisted diffusion, since the dopant incorporation process was already in the growth rate-limited regime. In case (ii), the cascade-assisted diffusion will dominate the diffusion process before the dopant incorporation process can be classified to be in the growth-rate-limited regime. This implies that the effective diffusivity dominated by the cascade-assisted diffusion is so large such that αR_p is comparable to unity or much smaller than unity . Thus the approach of dopant incorporation probability to unity is no longer controlled by the thermal activation energy, instead, it is controlled by the apparent activation energy due to cascade-assisted diffusion below the transition temperature. The curve 1 in Fig. 4.6 shows case (i), in which the effect of cascade assisted diffusion does not play an important role in dopant incorporation and curve 2 corresponds to case (ii), in which a second activation energy plays a role in the ion incorporation probability. The parameters used in calculating these two curves are shown in the figure caption. The only difference is a change in the effective pre-exponential factor for cascade-assisted diffusion which can be adjusted by changing the ion flux. Figure 4.7 shows the data points taken from reference [3] and the curves calculated using equation (2-ii) with $v = 0.17$ nm/s, $R_p = 1.1$ nm for 400 eV Sb ions and the choices of R_p at other different energies are the same as before, $D_0 = 0.214$ cm^2/s for all energies, and the activation energy is 3.23 eV for 100 eV Sb ions, 3.31 eV for 200 eV Sb ions, 3.36

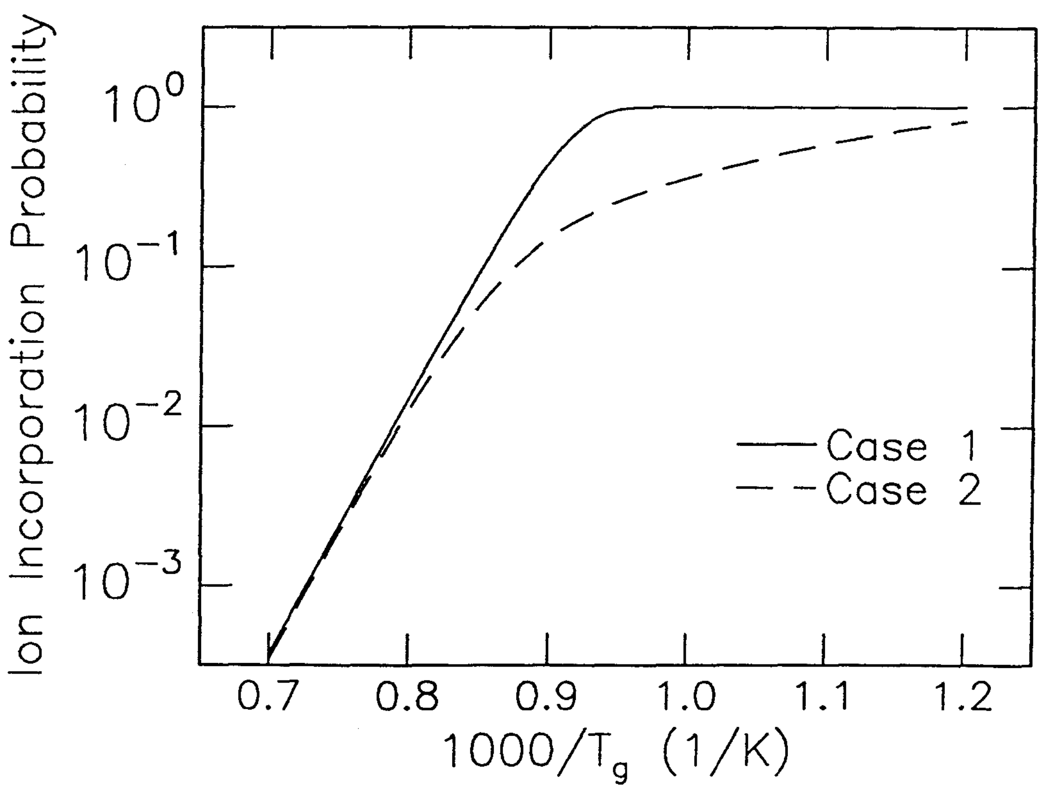

Figure 4.6 The ion incorporation probability as a function of growth temperature. In case 1 (solid line), the thermal diffusivity dominates from $\alpha R_p = 0$ to $\alpha R_p \gg 1$. In case 2 (dashed line), the cascade-assisted diffusivity extends down to $\alpha R_p < 1$. The parameters used to calculate these two curves are $D_0 = 0.214$ cm^2/s and $Q_m = 3.2$ eV for thermal diffusivity, $D_0 = 1 \times 10^{-16}$ cm^2/s and $Q_a = 0.6$ eV for cascade-assisted diffusivity in case 1, and $D_0 = 1 \times 10^{-13}$ cm^2/s and $Q_a = 0.6$ eV for cascade-assisted diffusivity in case 2.

eV for 300 eV Sb ions, and 3.40 eV for 400 eV Sb ions. The activation energies are chosen this way so that the previous diffusivities at 900°C for different ion energies, obtained from the growth rate dependence of dopant incorporation are numerically equal in the context of the present single activation energy model. The experimental conditions in reference [3] correspond to case (i) in Fig. 4.6 due to the low ion flux and high growth temperature which were used. The calculated curves fit the data points well for ion energies larger than 300 eV while giving poor fits for lower energy ion beams. It is also interesting to compare the difference between the inert gas incorporation. Our previous measurements of the Xe concentration trapped inside Ge films [1] indicated that the incorporation probability of Xe was only about 3% even when the growth conditions were in the growth rate-limited regime. This suggests the importance of the incorporation coefficient.

The major deviation of the moving boundary diffusion model from low energy ion incorporation data is due to the multiple activation processes for dopant incorporation such as adsorption and desorption of the ions at the surface, the difference between surface phonon and bulk phonon, and the electronic state near surface which all could contribute to the multiple activation processes. All the curves in Fig. 4.5, Fig. 4.6, and Fig. 4.7 are calculated from equation (2-ii) which is a solution subjected to the boundary condition that $N(0) = 0$ which is not a good condition for low energy dopant incorporation processes and predicts that no dopant incorporation will occur through adsorption and desorption processes. One should also avoid the dopant incorporation processes at the temperature regime below T_{tr} where the defects generated by the ion beam are stable. Since, the simple moving boundary diffusion model neglects the depth dependence of the diffusivity of the defects, the quantitative use of this simple model is probably only suitable for higher energy ion beams (e.g., $E_i > 300$ eV).

4.5 Conclusions

The IAMBE processes can be modeled using a continuous moving boundary dif-

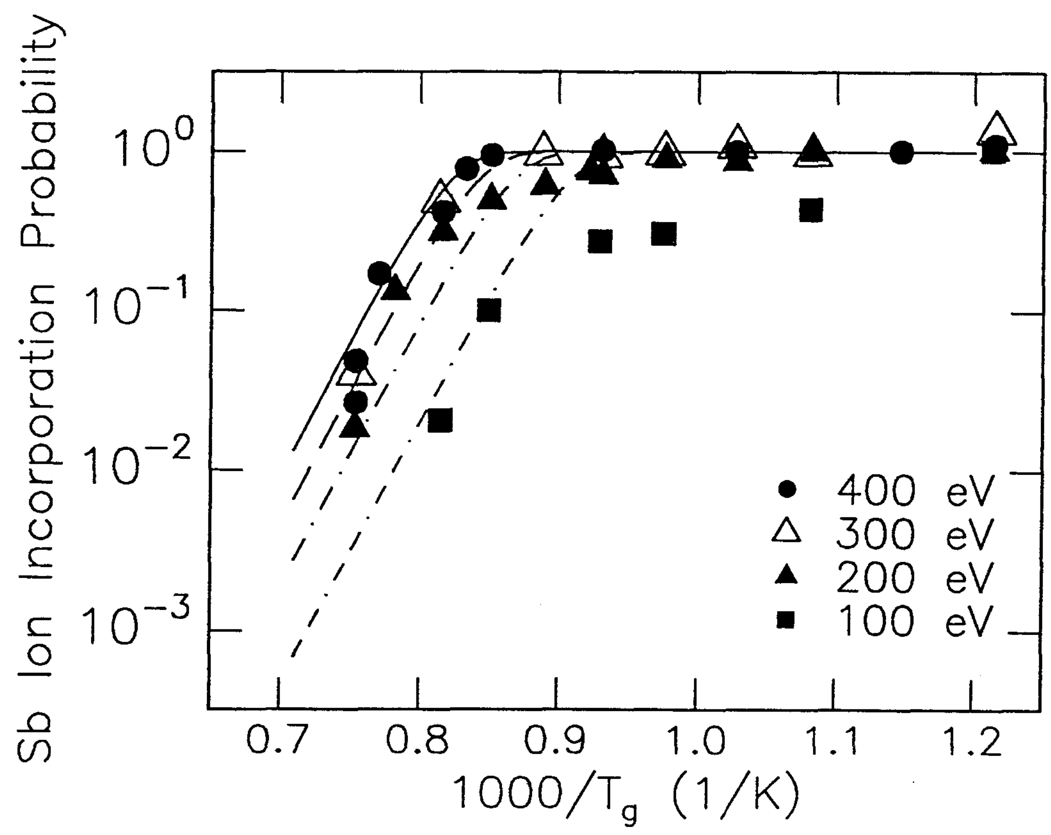

Figure 4.7 The temperature dependence of the dopant incorporation for different Sb ion energies. The data points are taken from reference [3]. All lines are calculated with $D_0 = 0.214$ cm^2/s and $v = 0.17$ nm/s. The values of R_p, 0.25 nm, 0.53 nm, 0.81 nm, and 1.1 nm, and the values of activation energy for Sb ions in Si, 3.23 eV (dotted line), 3.31 eV (dot-dashed line), 3.36 eV (dashed line), and 3.40 eV (solid line), correspond to 100 eV, 200 eV, 300 eV, and 400 eV Sb ions respectively.

fusion model. The defect concentration generated by the ion beam is proportional to the ion-to-atom flux ratio in the growth rate limited regime. The definitions of surface defects (defects that will come out to the surface) and bulk defects (defects that will be trapped inside the bulk) were defined in a dynamic term as a function of the growth rate, defect production range, and defect diffusivity. The low apparent activation energy obtained from the growth temperature dependence of the strain annihilation is explained by cascade-assisted defect diffusion. In IAMBE processes, the ion beam generates a cascade which undergoes athermal and thermal recovery. The defects left after cascade recovery have a diffusivity determined by the relative importance of the thermal diffusion and subsequent cascade-assisted diffusion. The same equation can also be used to described the dopant incorporation processes and reasonable agreement with experimental data can be found for higher energy ion beams. In low energy ion incorporation processes, the defect incorporation may accompany the dopant incorporation. In general, the activation energies for defect diffusion and dopant diffusion are not the same. Neglecting the interaction between defects and dopants, one could define transition temperatures for both defects and dopants. For enhancing dopant incorporation while minimizing defect incorporation, one should also avoid the dopant incorporation processes at the temperature regime below T_{tr} where the defects generated by the ion beam are stable. The moving boundary diffusion model gives a unified view of dopant and defect incorporation processes. The multiple activation site in the surface region can be done by adding layers in the surface region with different diffusivities and continuous boundary conditions at each interface. However, the model can only be used to describe the incorporation of point-like defects. When extended defects formation or the segregation of the dopants is involved, the simple model needs to be modified.

References

[1] C.J. Tsai, H.A. Atwater, and T. Vreeland, Appl. Phys. Lett. **57**, 2305 (1990).

[2] C.J. Tsai, P. Rozenak, H.A. Atwater, and T. Vreeland, J. Cryst. Growth **111**, 931 (1991).

[3] W.-X. Ni, J. Knall, M.A. Hasan, G.V. Hansson, J.-E. Sundgren, S.A. Barnett, L.C. Markert, and J.E. Greene, Phys. Rev. B **40**, 10449 (1989).

[4] H. Windischmann, J. Appl. Phys. **62**, 1800 (1987).

[5] A.K. Myers-Beaghton and D.D. Vvedensky, Phys. Rev. B **42**, 5544 (1990).

[6] R. Kelly, Radiation Effects **32**, 91 (1977).

[7] P. Sigmund and C.Claussen, J. Appl. Phys. **52**, 990 (1981).

[8] G.J. Dienes and G.H. Vineyard, "Radiation Effects in Solids", Interscience Publishers, INC., New York (1957). G.H. Vineyard, Rad. Effects. **29**, 245 (1976).

[9] Y.T. Cheng, Mater. Sci. Rep. **5**, 47 (1990).

[10] I. Barin, "Thermochemical Data of Pure Substances", Pt. 1; (VCH, New York, 1989).

[11] M.W. Thompson and R.S. Nelson, Phil. Mag. **7**, 2015 (1962).

[12] M.W. Thompson, "Defects and Radiation Damage in Metals"; (Cambridge University Press, London, 1969).

[13] R.S. Averback, Nucl. Instr. Meth. **B15**, 675 (1986).

[14] C.M. Gilmore, A. Haeri, and J.A. Sprague, Thin Solid Films **165**, 359, 1988.

[15] F. Meyer, M. Zafrany, M. Eizenberg, R. Beserman, C. Schwebel, and C. Pellet, J. Appl. Phys. **70**, 4268 (1991).

[16] P. Sigmund, in "Sputtering by Particle Bombardment I", edited. by R. Behrisch; (Springer, Berlin, 1981), Ch. 2.

Chapter 5

Island Suppression during Initial Growth Stage of Ge on Si(100) by Ion-Assisted Molecular Beam Epitaxy

5.1 Introduction

The growth of heteroepitaxial films with atomically sharp interfaces is important in solid-state electronic device applications. In the growth of heteroepitaxial films, three different growth modes have been identified : (i) a 3-D island growth (termed the Volmer-Weber mode), (ii) a 2-D layer-by-layer growth (termed the Frank-van der Merwe mode), and (iii) a 2-D layer-by-layer growth to some thickness followed by 3-D island growth (termed the Stranski-Krastanov mode). Figure 5.1 schematically illustrates these three growth modes. The simplest criteria for the equilibrium growth mode depends on the relative surface energies of a substrate (σ_s), a film (σ_f), and their interface (σ_i). If the strain energy due to the lattice mismatch between a film and its substrate can be neglected, the condition for these growth modes are :

(1) $\sigma_s < \sigma_f + \sigma_i$ (Volmer Weber)
(2) $\sigma_s > \sigma_f + \sigma_i$ (Frank-van der Merwe)
(3) $\sigma_s > \sigma_f + \sigma_i$ (Stranski-Krastanov)

The Stranski-Krastanov(SK) growth mode is a complication of the layer-by-layer growth mode due to other factors, for example, the strain energy of a lattice mismatched film, the extra energy for surface reconstruction, etc. In the case of Ge and Si, Ge has a lower surface energy than Si and about 4% larger in the lattice constant than that of Si. For Si films grown on Ge(100), the Volmer-Weber growth mode are generally observed, but for Ge films grown on Si(100), the SK growth mode is observed in the initial growth stage. It has been shown that for non-zero misfit between film and substrate that layer-by-layer growth is never the equilibrium growth mode [1]. Here, we investigate the effect of low energy ion bombardment during the initial stages of growth of Ge on Si(100) and try to find the actual mechanisms modified by

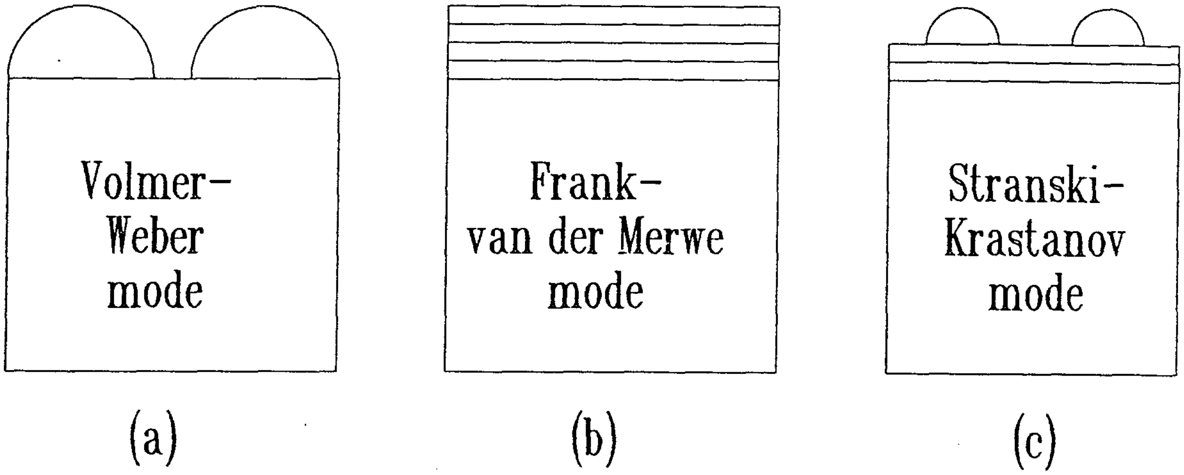

Figure 5.1 Schematic representations of three different crystal growth modes.

low energy ion beam which are responsible for the observed island suppression.

5.2 Experimental Observations

The molecular beam epitaxy growth system used is described in chapter 3. Si films with thicknesses in the range of 10 nm to 80 nm were grown as buffer layers on top of Si substrate at 550°C at a growth rate of 0.1 nm/s. The cleaning procedure is described in the Appendix B. Reflection high energy electron diffraction (RHEED) operated at 12 KeV with an emission current of 40-50 mA was used to monitor the growth surface. The buffer layer growth was stopped when a strong RHEED specular beam was observed in out-of-phase condition. Ge films were then grown in the temperature range from 300-500°C with a growth rate of 0.8-1.2 nm/min. In the following description, the nominal growth rate is 0.8 nm/min. unless otherwise specified. The Ge film thicknesses ranged from 1.0-2.0 nm. The Ar^+ ion energies varied from 70-150 eV and the ion-atom flux ratio, J_i/J_a, was in the range of 0.1-0.3. The sputtering yield for Ar^+ 150 eV on Ge target is in the range of 0.1-0.3 for this energy range [2]. For $J_i/J_a = 0.3$, the reduction in growth rate modified film thickness due to sputtering is less than 10%. For a 2.0 nm films, the reduction in thickness is only 0.2 nm. The thickness of the Ge films for various samples were randomly selected to be measured by Rutherford backscattering spectrometry (RBS) to confirm that the thickness did not vary more than 10%.

Figure 5.2(a) shows two series of RHEED pattern for a film grown by ion-assisted molecular beam epitaxy (IAMBE) and a thermally grown film at a growth rate of 1.2 nm/min. These two series of RHEED pattern were obtained from the same substrate by blocking half of the sample. Thus, half of the substrate was subjected to 70 eV Ar ion bombardment with $J_i/J_a = 0.3$. The sample was grown at 350°C. The RHEED patterns were taken by interrupting the growth every 5 seconds. Figure 5.2(b) shows the final surface morphology of the samples. The fluctuation of the diffraction intensity along the Bragg rods in a RHEED pattern indicates roughness of a surface along the growth direction, e.g., island growth. The surface roughness along the growth direction reduces the 2-dimensional characteristics of the surface. Hence, the diffraction intensity concentrates around the bulk Bragg spot. As the surface roughness increases, the diffraction intensity at a position which is not corresponding to a 3-dimensional diffraction spot decreases intensity, thus increases the fluctuation of diffraction intensity along the Bragg rod. The RHEED pattern will become more and more "spotty" as the roughness along the growth direction increases. As we can see in Fig. 2 (a) , the RHEED patterns became more and more spotty as Ge films thickness became thicker and thicker. This indicates increases in roughness along the growth direction as films become thicker. A comparison between the IAMBE grown film and the thermally grown films shows that the surface of the thermally grown sample is rougher than that of the IAMBE grown sample (Fig. 2(b)). Figure 5.3 shows two series of RHEED pattern for a film grown by ion-assisted molecular beam epitaxy (IAMBE) and a thermal grown film. The samples were grown at 475°C. The IAMBE film was bombarded using 150 eV Ar^+ with $J_i/J_a = 0.3$. The RHEED patterns were

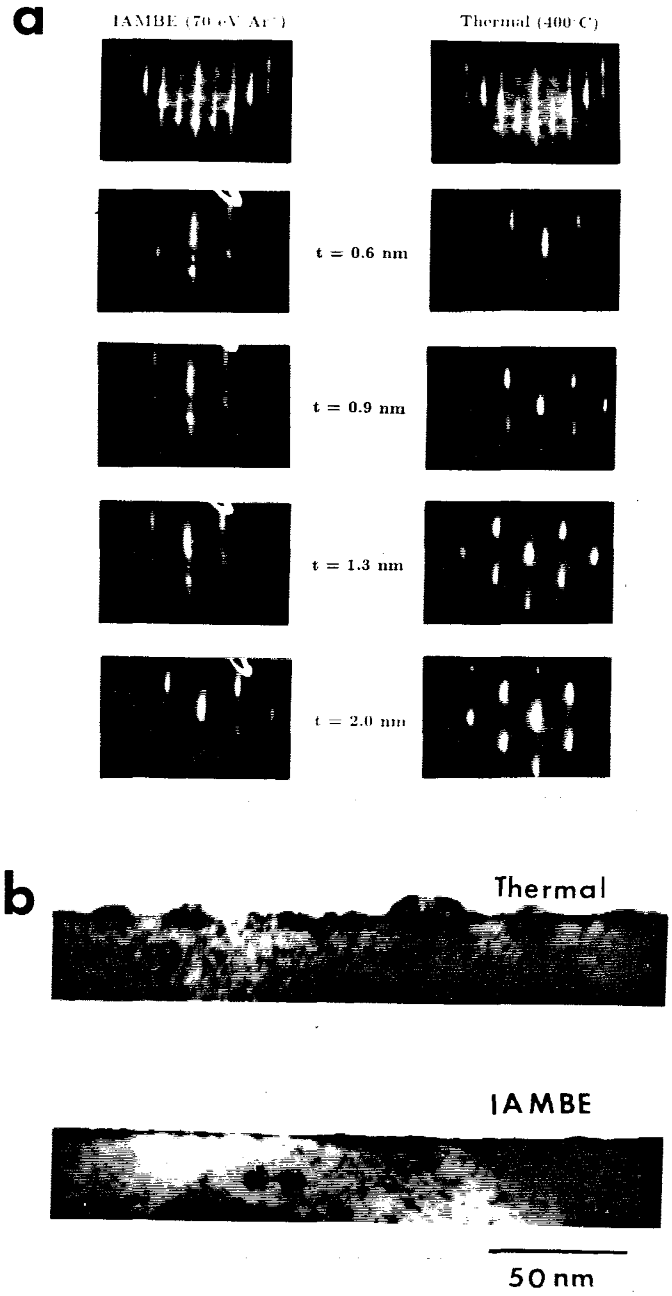

Figure 5.2 (a) RHEED patterns along [110] azimuth for a film grown by ion assisted molecular beam epitaxy and for a film grown by conventional molecular beam epitaxy. See text for detail growth conditions. (b) The cross section transmission electron micrographs (bright field, [110] zone axis) of the final surfaces of the corresponding samples.

taken without interrupting the growth. After 40s of deposition which corresponds to a thickness of 0.5 nm, the RHEED pattern for thermally grown sample is "spotty" already, while the specular beam in the IAMBE grown sample still persists. The RHEED patterns for the thermally grown sample became spotty more rapidly than the thermally grown sample shown in Fig. 5.2, while the final RHEED pattern for IAMBE films appears to be smoother than that of the IAMBE film in Fig. 5.2. The RHEED patterns of the IAMBE grown film shown in Fig. 5.3 shows diffusive Bragg rods (perpendicular to the rods) which indicates a two-dimensional roughness on the surface. However, the surface roughness along the growth direction is suppressed significantly compared to the thermally grown sample. The effectiveness of the ion energy on the island suppression is noticeably large.

5.3 Islanding Kinetics without Ion Bombardment

To better understand the island suppression mechanism during IAMBE process, it is important to examine both the thermodynamic driving force for island formation and the islanding kinetics. Tersoff [3] has investigated the SK growth mode of Ge on Si(100) using a modified Keating potential [4]. The results show that the layer-by-layer growth is expected for the first monolayer regardless of other details because Ge has a much lower surface energy than Si and is stabilized for up to 3 layers due to the energy gained by having a softer material with large strain associated with the surface dimerization (reconstruction). The analysis is based on quasi-equilibrium state without considering the kinetics of the island formation. Srolovitz [5] proceeded to use another approach which considers the continuum elastic stability of the surface of a strained epitaxial film. By balancing the elastic energy change in evolution from a flat surface to a perturbed surface profile with the increase of the surface energy, Srolovitz [5] defines a critical wavelength of stability for a smooth surface which depends on the surface diffusion kinetics. The surface will be smoothened for a perturbed surface profile with a wavelength smaller than the critical wavelength due to the significant

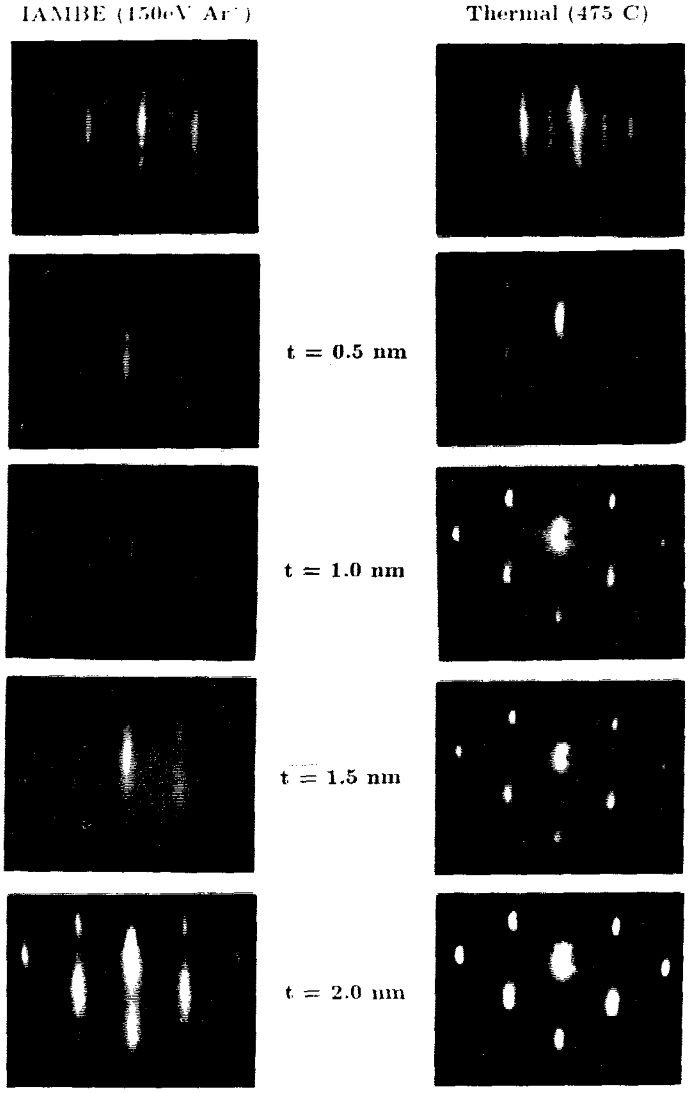

Figure 5.3 RHEED patterns along [110] azimuth for a film grown by ion assisted molecular beam epitaxy and a film grown by conventional molecular beam epitaxy. See text for detail growth condition.

increase in surface energy. Spencer et al., [6] further extended Srolovitz's approach to a time-dependent linear stability problem. The model proposed by Spencer et al., [6] assumes that the island is coherent and the island formation is kinetically limited by adatom surface diffusion. The strain energy of the film is reduced by formation of island for a traction-free surface. In this time-dependent case, the island will grow if the growth rate of the perturbation amplitude is smaller than the deposition rate and vice-versa.

Several methods for island suppression during the initial stage of SK growth mode or VW growth mode have been investigated. Copel et al., [7, 8] used As surfactants to alter the energetics of growth and kinetically inhibited the island formation and inter-diffusion. Eaglesham and Cerullo [9] have also demonstrated that the island formation did not occur for Ge films grown on Si at 200°C which can be explained as kinetic suppression because of limited surface diffusion.

Figure 5.4 (a-d) shows a series of high resolution transmission electron micrographs (HRTEM) and the corresponding RHEED pattern for samples grown at different temperatures (300-500°C). The average island size increases as the growth temperature increases as expected. This indicates the kinetic suppression of island formation. For most of the islanded films grown in this experiment, strain relaxation occurs which violates the assumption of Spencer's model that islands are coherent. Large coherent Ge islands have been reported [10] in which the misfit strain is accommodated by the local substrate deformation around these large coherent islands. The misfit strain accommodated by the dislocation formation or the local substrate deformation can alter the energetics of island formation. However, this should affect the quantitative but not the qualitative nature of the kinetic suppression as long as the island is strained to some degree. The HRTEM for 475°C shows tendency for island faceting along {113} which agrees with earlier work [11, 12].

5.4 Possible Mechanisms for Island Suppression using IAMBE

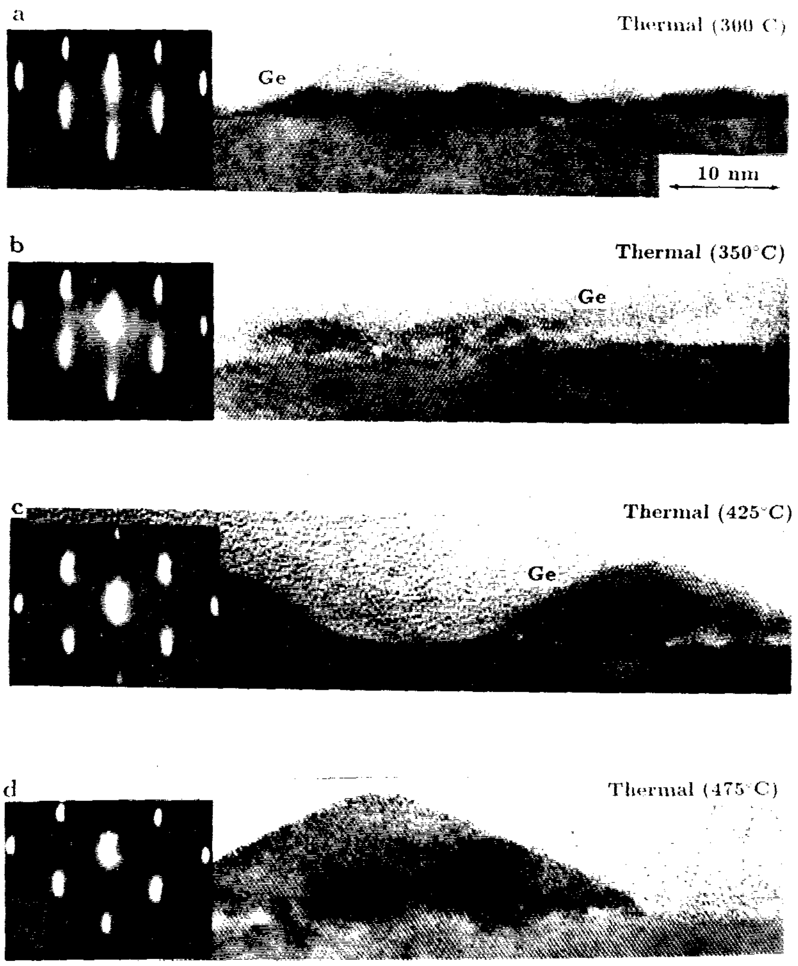

Figure 5.4 The growth temperature dependence of the island sizes.

Choi et al., [13, 14] use low energy Ar^+ beam ($E_i = 28$ eV) to suppress the island formation for InAs on Si and GaAs on Si. The suppression mechanism was attributed to the dissociation of sub-critical nuclei with the low energy ion beam, which decreased the nucleation rate of islanding [14]. Other investigations of the alternation of the islanding kinetics by low energy ion bombardments have been reported for systems with VW growth mode for poly-crystalline materials on amorphous substrates [15, 16]. Bombardment-induced island dissociation can either enhance the island growth rate relative to the island nucleation rate for high adatom mobility case [15] or enhance nucleation rate relative to the growth rate for low adatom mobility case [16].

Strain in the epitaxial overlayer is the thermodynamic driving force for island formation. As a tool for probing island formation kinetics, IAMBE is interesting because it allows the strain driving force for island formation and the surface amplitude fluctuations during island formation to be independently varied. The research reported here consistutes of the first measurement of the strain state for very thin IAMBE grown films and relation of strain to island formation. Figure 5.5 shows two X-ray interference spectrums of two samples grown with Ge thicknesses 1.0 nm and 1.5 nm at 450°C. The Ge films were bombarded with 200 eV Ar^+ at $J_i/J_a = 0.2$. Immediately after Ge growth, another 250 nm Si was grown thermally to generate X-ray interference effect. In Figure 5.5(a), the solid line corresponds to the experimental data and the dotted line corresponds to the calculated spectrum with a phase factor of 1.59. Thus, the thickness of the Ge layer is estimated to be 1.0 nm. The clear interference spectrum strongly suggests that little dislocations exist in the capped Si layer. In Figure 5.5(b), no clear interference effect was observed which suggests that the capped layer contains a significant number of dislocations, and that the film is at least partially relaxed. The nominal Ge coverage (atoms/cm^2) for both samples were also checked by RBS. From the X-ray data, we know that all of the 2.0 nm films in our experiment are partially relaxed. This shows that the islanding does not coincide with the strain relaxation for IAMBE grown films in contrast to the thermally grown

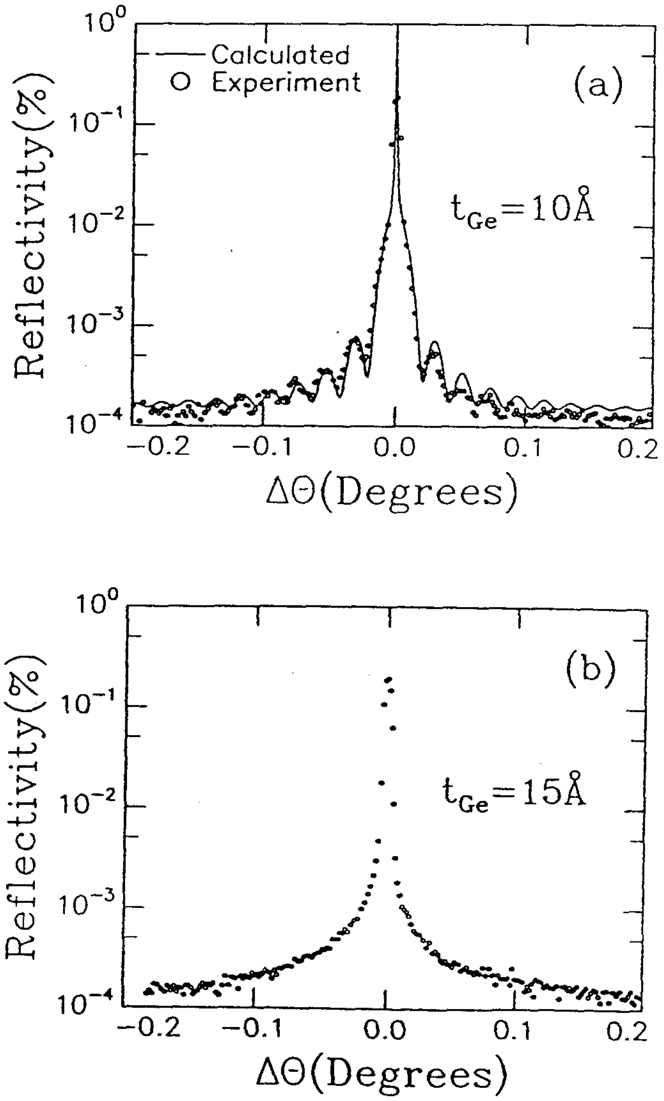

Figure 5.5 X-ray interference spectrums of IAMBE grown Ge films 1.0 nm thick (a) and 1.5 nm thick (b) with concurrent 200 eV Ar^+ bombardment at $J_i/J_a = 0.2$. The Ge films were capped with 250 nm thick Si. The solid line in (a) is the calculated curve using dynamical diffraction theory.

samples [16-19].

Interface mixing can lower the strain energy, and rearrangement of the Si and Ge atoms at the surface can further compensate the surface stresses associated with the reconstruction [3]. To address this point, evolution of surface morphology during growth and after post-growth annealing was examined. Figure 5.6(a) shows two RHEED patterns and a HRTEM of a 2.0 nm thick Ge film grown on Si (001)at 300°C and bombarded by 150 eV Ar^+ with $J_i/J_a = 0.3$. After growth, the sample was heated up to 475°C for 5 min. and then the heater was turned off immediately. At this annealing temperature, the interdiffusion between Ge and Si is negligible. Figure 5.6(b) shows another two RHEED patterns of a sample grown at 300°C with a Ge thickness of 1.2 nm and bombarded by 100 eV Ar^+ with $J_i/J_a = 0.3$. After growth, the sample was annealed at 475°C for 30 min. The RHEED pattern after annealing is less streaky than the RHEED pattern before annealing but the effect is not substantial. This suggest that the interface mixing effect has suppressed the island formation. However, the islanding occurs at 2.0 nm which indicates that the intermixing between Ge and Si is not completely responsible for the suppression mechanism of IAMBE process. Figure 5.6(c) shows the RHEED patterns and HRTEM of Ge films which were grown at 300° and bombarded with 150 eV Ar^+ with $J_i/J_a = 0.2$ during the first 1.2 nm of growth. Subsequently, the ion beam was turned off and another 0.8 nm was grown thermally at the same temperature. Islanding also occurs in 5.6(c) as in 5.6(a) indicating that ion bombardment during growth does not significantly diminish the misfit strain driving force for islanding. These results support the viewpoints that island suppression using IAMBE is a dynamical process in which the critical requirement is a minimization of surface amplitude fluctuation. The results also imply that bombardment-induced interface mixing effects appear to be unimportant, under these growth conditions.

Chason et al., [21, 22] have studied the evolution of surface morphology of Xe bombarded Ge (001) surface and found that, in the temperature range 250-400°C,

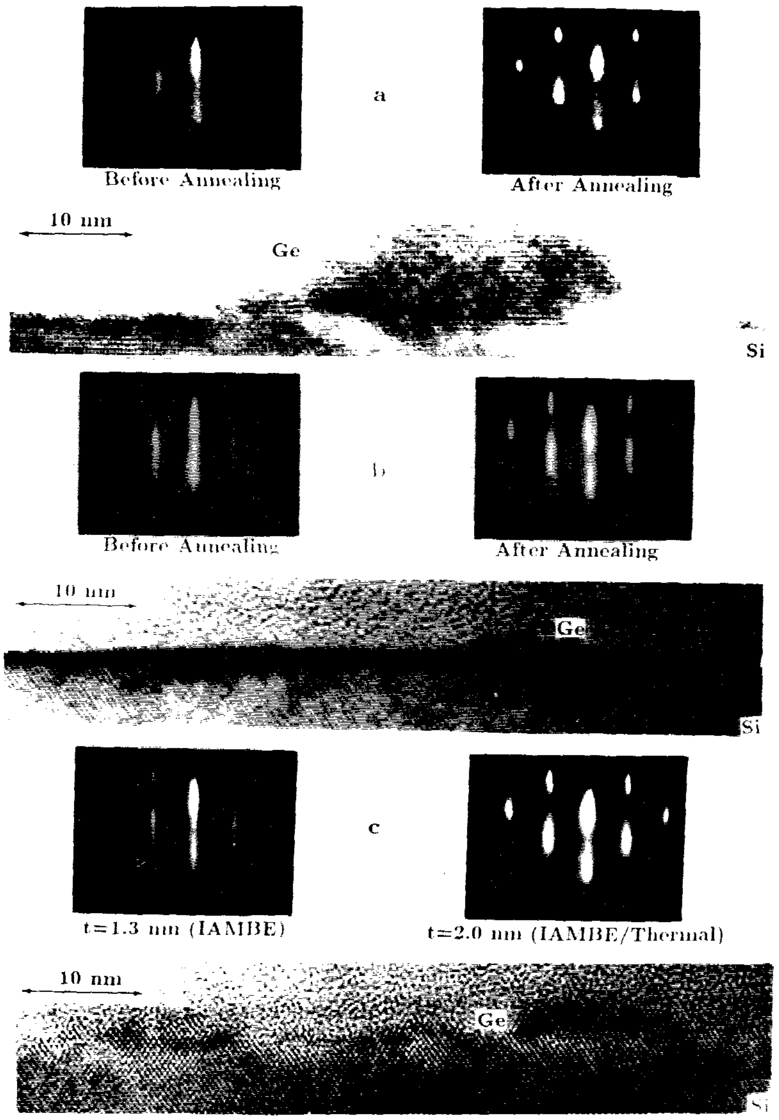

Figure 5.6 (a) The before-annealing and after-annealing RHEED patterns for a Ge film with 2.0 nm thick and the corresponding HRTEM after annealing. (b) The before-annealing and after-annealing RHEED patterns for a Ge film with 1.2 nm thick. (c) The RHEED pattern and the HRTEM of a Ge film grown in two steps. For detail growth conditions see text.

the surface reaches a steady state roughness and the smoothening kinetics is similar to the growth smoothening. Bedrossian et al., observed RHEED oscillation due to layer-by-layer sputtering of the Si with 200-250 eV Xe^+ at temperature range 350-470°C [23]. Above this temperature regime, the RHEED oscillation disappears. Bedrossian et al., concluded that the layer-by-layer sputtering is due to the condensation of vacancy-like defects on the surface into surface sites and the behavior of the vacancy-like defects is generally analogous to that of adatoms. Thus at high temperatures, surface vacancies migrate to the step edge which results in the step edge retraction and RHEED oscillation disappears. For Ge surface bombarded at temperature above 400°C, the RHEED specular beam intensity does not change significantly [21] which indicates that the surface vacancy is mobile. These results are analogous to adatom kinetics in epitaxial growth, thus it is clear that the surface roughness is ion flux dependent for a fixed ion energy and ion species and the transition temperature above which a certain fraction of the surface vacancies created can migrate to the step ledges is flux-dependent. With comparable ion flux and growth rate to Chason's experiment, although not the same ion species, our results show that the island suppression effect of Ge films on Si using 150 eV Ar^+ exists even at growth temperature of 475°C which suggests that the surface vacancy-produced surface roughness is not a critical factor in island suppression. However the RHEED patterns of IAMBE grown Ge films bombarded by 150 eV Ar^+ typically show diffuse diffraction rods which indicates microscopy in-plane surface roughness on the order of 4.0 nm.

Figure 5.7 shows another series of HRTEM microghaphs of 2.0 nm thick samples grown at 425°C . The Ge film in Fig. 5.7(a) was grown by thermal MBE. Figure 5.7(b) shows a Ge films grown by IAMBE with 150 eV Ar^+ at $J_i/J_a = 0.27$. The Ge film in Fig. 5.7(c) was grown by thermal MBE and, after growth, the film was bombarded with 150 eV Ar^+ at a flux of 1.3×10^{13} ions/cm^2-s for 5 min. The film in Fig. 5.7(d) was grown by thermal MBE on a 6° miscut substrate off (001) toward (100) which will have an average terrace width of about 1.5 nm assuming a single layer step [24]. The decrease in terrace width induced by substrate miscut does not appear to suppress island formation. The average aspect ratio (height-to-diameter) for islands is 0.25±0.04 for thermally grown samples and 0.16±0.04 for films subjected to after growth sputtering. Similar results for Ge films grown at 475°C were observed also as shown in Fig. 5.8. The films thickness of the samples shown in Fig. 5.8 (a) and (b) is 1.8 nm and that of the sample after sputtering shown in Fig. 5.8 (c) is 1.6 nm estimated from RBS measurements. It is interesting to compare the RHEED pattern of sample (a) and (c) in Fig. 5.8. The RHEED pattern of sample (c) in Fig. 5.8 shows a slight increase in diffraction intensity along the diffraction rod direction after sputtering which suggests that island dissociation has occurred during post-growth bombardment of the islanded films. Some stacking faults were also observed in the post-growth sputtered samples. It is possible that the partial dislocations associated with the stacking faults may be formed by the precipitation of a closed-packed vacancy or interstitial loops produced by the ion bombardment (Frank partial dislocation).

The above experimental observations in conjunction with the time-dependent linear stability model [6], suggest that bombardment-induced island suppression can be explained by the dissociation of the islands. Island suppression in turn reduces the growth rate of the perturbation amplitude relative to the deposition rate, thus, the onset of the islanding is delayed relative to that for films grown by thermal MBE. Besides the direct dissociation of the islands in the early stage before strain relaxation, the strain relaxation before islanding can also contribute to the reduction of the growth rate of the perturbation amplitude at the later stage. This explanation is similar to the explanation given by Choi et al., [14] through the concept of suppressing nucleation rate for island formation. Hence, we can frame these results in terms of the time-dependent stability [6] model as follows: for a specified deposition rate and growth rate of the perturbation amplitude, there is a critical ion-atom flux ratio above which the growth rate of the perturbation amplitude can be suppressed

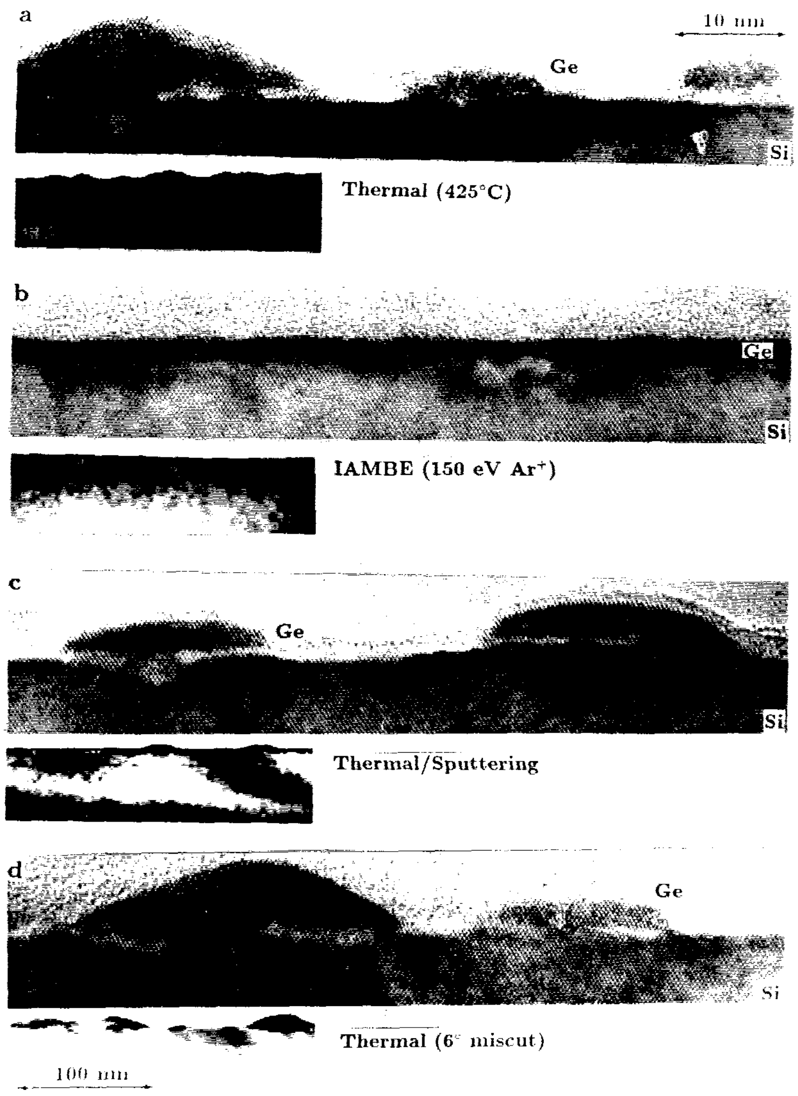

Figure 5.7 (a) A thermally grown sample, (b) a sample by IAMBE, (c) a sample grown thermally and then sputtered, and (d) a sample grown thermally on a 6° miscut substrate off (001) toward (100). Details see text.

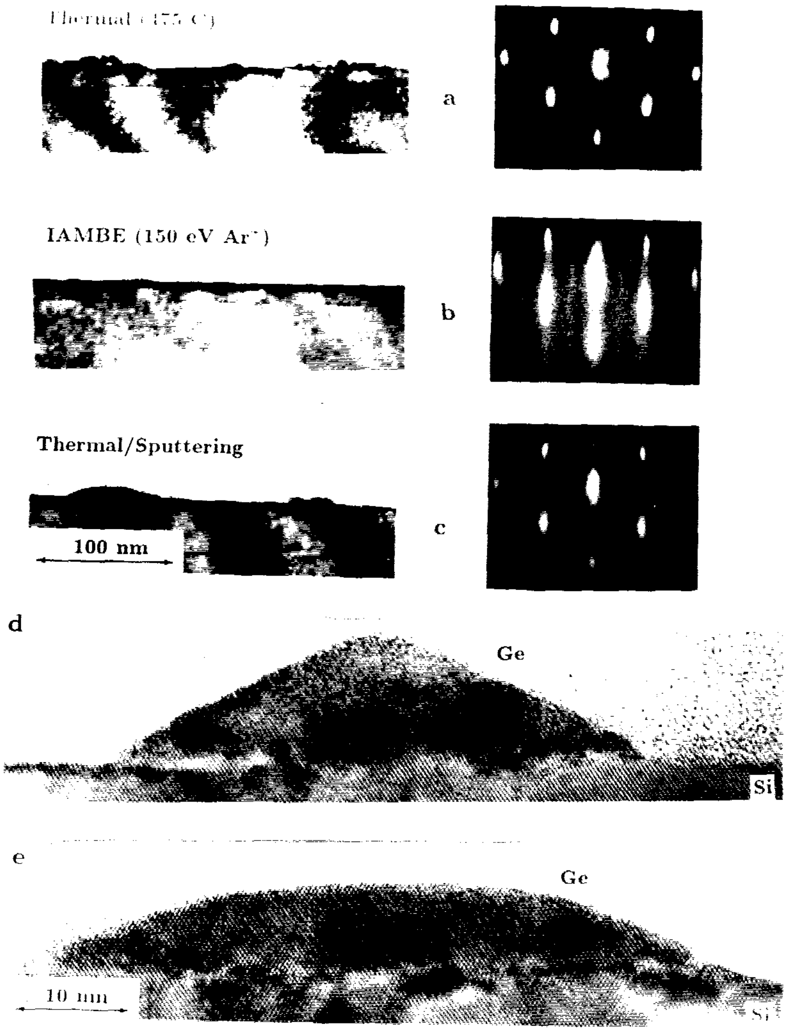

Figure 5.8 Bright field electron micrographs and RHEED patterns of(a) a thermally grown sample, (b) a sample grown by IAMBE with 150 ev Ar^+ at $J_i/J_a = 0.3$, (c) a sample grown thermally and then sputtered with 150 eV Ar^+ at a flux of 1.2×10^{13} ions/cm^2-s for 5 min., (d) the corresponding HRTEM of sample (a), and (e) the corresponding HRTEM of sample (b).

completely and below which the critical thickness for island formation is prolonged.

5.5 Conclusions

In heteroepitaxial growth of a film with lower surface energy than that of the substrate, the misfit strain associated with the growth will change the growth mode from Frank-van der Merwe mode to Stranski-Krastanov mode. The thermodynamic driving force for islanding is the reduction of the misfit strain energy associated with the growth of an heteroepitaxial system. The change of the growth mode is likely for materials with low plastic deformation rate such as semiconductors. The islanding kinetics is governed by the two adatom surface diffusion. The relative rate for the film growth and the island growth which is characterized by a perturbation amplitude of the surface determines a critical thickness for island formation. The results here show that ion bombardment-induced island dissociation can reduce the surface amplitude fluctuation, and that this is the island suppression mechanism for Ge growth on Si by IAMBE. These results also imply that ion bombardment suppresses island formation without significant reduction in the film strain driving force for islanding via, e.g. bombardment-induced mixing or point defect injection.

More universally, this work demonstrate that strain relief via plastic deformation (i.e., generation of misfit dislocations) and islanding are in fact unrelated, but competing mechanisms for misfit reduction. In this context, ion bombardment is a tool which allows the surface amplitude fluctuations to be suppressed independently of plastic deformation kinetics, thereby demonstrating their fundamental independence.

References

[1] G.H. Gilmer, M.H. Grabow, and A.F. Bakker, Mater. Sci. Eng. B **6**, 101 (1990).

[2] H.H. Andersen and H.L. Bay, "Sputtering by Particle Bombardment I", ed. R. Behrisch, Chap. 4, P.145 (Springer-Verlag Berlin Heidelberg, 1981).

[3] J. Tersoff, Phys. Rev. B **43**, 9377 (1991).

[4] P.N. Keating, Phys. Rev. **145**, 637 (1966).

[5] D.J. Srolovitz, Acta Metall. **37** 621 (1989).

[6] B.J. Spencer, P.W. Voorhees, and S.H. Davis, Phys. Rev. Lett. **67**, 3696 (1991).

[7] M. Copel, M.C. Reuter, E. Kaxiras, and R.M. Tromp, Phys. Rev. Lett. **63**, 632 (1989).

[8] M. Horn-von Hoegen, F.K. LeGoues, M. Copel, M.C. Reuter, and R.M. Tromp, Phys. Rev. Lett. **67** 1130 (1991).

[9] D.J. Eaglesham and M. Cerullo, Appl. Phys. Lett. **58**, 2276 (1991).

[10] D.J. Eaglesham and M. Cerullo, Phys. Rev. Lett. **64**, 1943 (1990).

[11] Y. Koide, S. Zaima, N. Ohshima, and Y. Yasuda, Jpn. J. Appl. Phys. **28**, 690 (1989).

[12] Y.-W. Mo, D.E. Savage, B.S. Swartzentruber, and M.G. Lagally, Phys. Rev. Lett. **65**, 1020 (1990).

[13] C.-H. Choi, L. Hultman, and S.A. Barnett, J. Vac. Sci. Technol. A **8**, 1587 (1990).

[14] C.-H. Choi, R. Ai, and S.A. Barnett, Phys. Rev. Lett. **67**, 2826 (1991).

[15] M-A. Hasan, J. Knall, S.A. Barnett, A. Rockett, J.-E. Sundgren, and J.E. Greene, J. Vac. Sci. Technol. A **5**, 1883 (1987).

[16] S. Nikzard and H.A. Atwater, Mat. Res. Soc. Symp. Proc. **223** (1991).

[17] J.E. Macdonald, A.A. Williams, R. van Silfhout, J.F. van der Veen, M.S. Finney, A.D. Johnson, and C. Norris, "Kinetics of Ordering and Growth at Surface", ed. M.G. Lagally, P. 473 (Plenum Press, New York, 1990).

[18] G.J. Whaley, P.I. Cohen, Mat. Res. Soc. Symp. Proc. **160**, 35 (1990).

[19] A.A. Williams, J.M.C. Thornton, J.E. Macdonald, R.G. van Silfhout, J.F. van der Veen, M.S. Finney, A.D. Johnson, and C. Norris, Phys. Rev. B **43**, 5001 (1991).

[20] G.L. Price, Phys. Rev. Lett. **66**, 469 (1991).

[21] E. Chason, J.Y. Tsao, K.M. Horn, and S.T. Picraux, J. Vac. Sci. Technol. B **7**, 332 (1989).

[22] E. Chason, J.Y. Tsao, K.M. Horn, S.T. Picraux, and H.A. Atwater, J. Vac. Sci. Technol. A **8** 2507 (1990).

[23] P. Bedrossian, J.E. Houston, J.Y. Tsao, E. Chason, and S.T. Picraux, Phys. Rev. Lett. **67**, 124 (1991).

[24] G.E. Crook, L. Daweritz, and K. Ploog, Phys. Rev. B **42**, 5126 (1990).

Chapter 6
Effect of Low Energy Ion Bombardment on the Misorientation of Ge Films on Si (001)

6.1 Introduction

It is known that growth in lattice-mismatched heteroepitaxial systems can induce a misorientation between an epitaxial film and the substrate. Several reported systems are $Ga_xIn_{1-x}As$ on GaAs [1-3] GaAs on Si [4], CdTe on InSb [5], $In_xGa_{1-x}As$ on InP [6], Si_xGe_{1-x} on Si [7], $CoSi_2$ on Si [8, 9], ZnSe on Ge [10], and $GaAs_{1-x}Sb_x/GaAs$ superlattices on GaAs [11]. The misorientations are found to depend on the substrate orientation [1], surface preparation [5], lattice misfit [6], substrate miscut angle [1, 8, 9], and film thickness [10]. In most cases, the misorientation angle is tilted toward the surface normal for films with lattice constants larger than that of the substrate and is tilted away from the surface normal for films with lattice constant smaller than that of the substrate. By tilting the growth planes of the film with respect to the corresponding substrate planes, the lattice constant difference between the film and the substrate is reduced which thereby, reduces the misfit strain. Misorientation between a film and substrate may influence optical and electrical properties. Optical properties of InGaAs epitaxial films grown on a GaAs substrate cut 2° off (001) towards (110) have been shown to be better than that of films grown on exactly cut GaAs (001) substrate [12]. In the growth of a terraced superlattice, the misorientation angle breaks the symmetry of the growth direction, thus, the optical and electrical properties are changed [13].

Despite all the research on this subject, the misorientation formation mechanism is still unclear, especially for the misorientation formation on a relaxed heteroepitaxial structure. In an attempt to understand the nature of the misorientation formation, we employed low energy ion bombardment during epitaxial growth and examined the effect of ion bombardment on the misorientation evolution for Ge films grown on

Si(001).

6.2 Experimental Observations

The growth system is described in Chapter 3. Ge films 5-30 nm thick were grown on Si(001), with or without Ge buffer layers, with concurrent Ar^+ bombardment, then 200-350 nm thick Ge films were subsequently grown on top of the IAMBE Ge films. The purpose of the thermally grown thick Ge film is to increase the X-ray diffraction intensity while minimizing the broadening effect of the X-ray diffraction peak contributed from other defects created by the ion beam in the thin IAMBE grown Ge film. The growth temperature was varied in the range of 250°C to 500°C. The ion-to-atom flux ratio was varied in the range of 0.05-0.3. The misorientation between a film and its substrate is determined using the procedures described in chapter 2. The growth conditions and the results measured from (004) diffraction of almost all of the samples using Cu-$K_{\alpha 1}$ radiation are listed in Table 6-I, where T is the growth temperature. All the films were grown at a growth rate of 0.1 nm/s, except for samples $D30$ and $D31$ which were grown at a rate of 0.05 nm/s and 1.7 nm/s respectively; E_i is the ion energy, t_i is the thickness of the IAMBE Ge films, t_b is the Ge film thickness grown thermally before the IAMBE Ge film (buffer layer thickness), t_T is the total thickness of Ge film include t_i and t_b as shown in Fig. 6.1, 4° miscut represents the angle cut off (001) towards (100) and has a deviation within 0.2° from sample to sample, $\epsilon_\perp$ is the perpendicular strain of the films relative to the substrate lattice constant, and φ is the misorientation angle between the film (001) axis and substrate (001) axis. All the samples were bombarded with the incoming ion beam angle at about 45° with respect to the surface normal except sample $D36$ for which the angle was normal to the sample surface. Figure 6.2 shows the substrate peak position of a miscut sample ($D10$) and the peak separation between the (004) diffraction peak of the Ge film and the (004) diffraction peak of the substrate as a function of azimuthal angle. The peak separation and the miscut are of opposite sign,

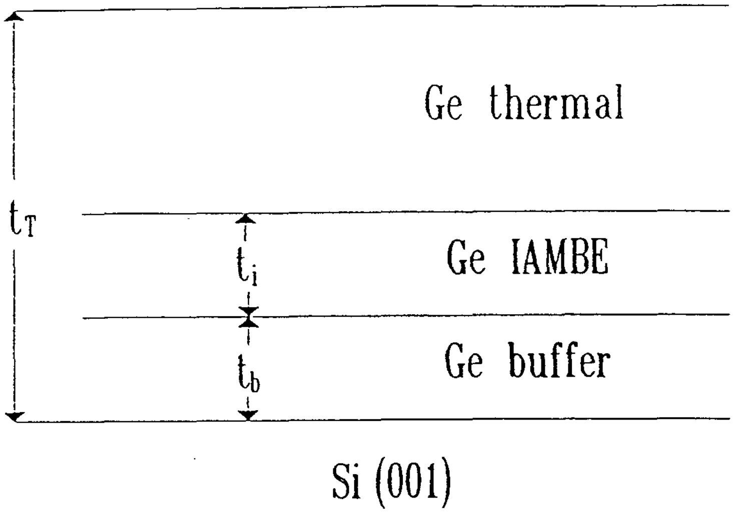

Figure 6.1 Schematics of samples configuration. t_i is the thickness of a Ge film grown with low energy ion bombardment, t_b is the thickness of a layer grown prior to the IAMBE film, and t_T is the total thickness of a Ge film.

which indicates that the Ge film is tilted toward the Si surface normal. Figure 6.3 shows the peak separation as a function of azimuthal angle for sample ($D19$) which was thermally grown without ion bombardment and sample ($D30$), which was grown at the same condition as the thermally grown one, except the first 30 nm was grown with concurrent ion bombardment (200 eV Ar^+, $J_i/J_a = 0.15$). A significant increase in the misorientation angle for the IAMBE grown film is observed. Figure 6.4 shows the dependence of the misorientation angle on the ion-atom flux ratio. A monatomic increase in misorientation was observed as the ion-atom flux ratio increases. The growth temperature dependence of the misorientation is shown in Fig. 6.5. The film-substrate misorientation increases as the growth temperature decreases. These behaviors are similar to that of the strain modification by ion-assisted molecular beam epitaxial (IAMBE). The full-width half-maximum (FWHM) of the diffraction peaks increase as the temperature decreases as shown in Fig. 6.6 and the perpendicular strain of the films relative to the substrate lattice constant, $\epsilon_\perp$, is also shown in Fig.

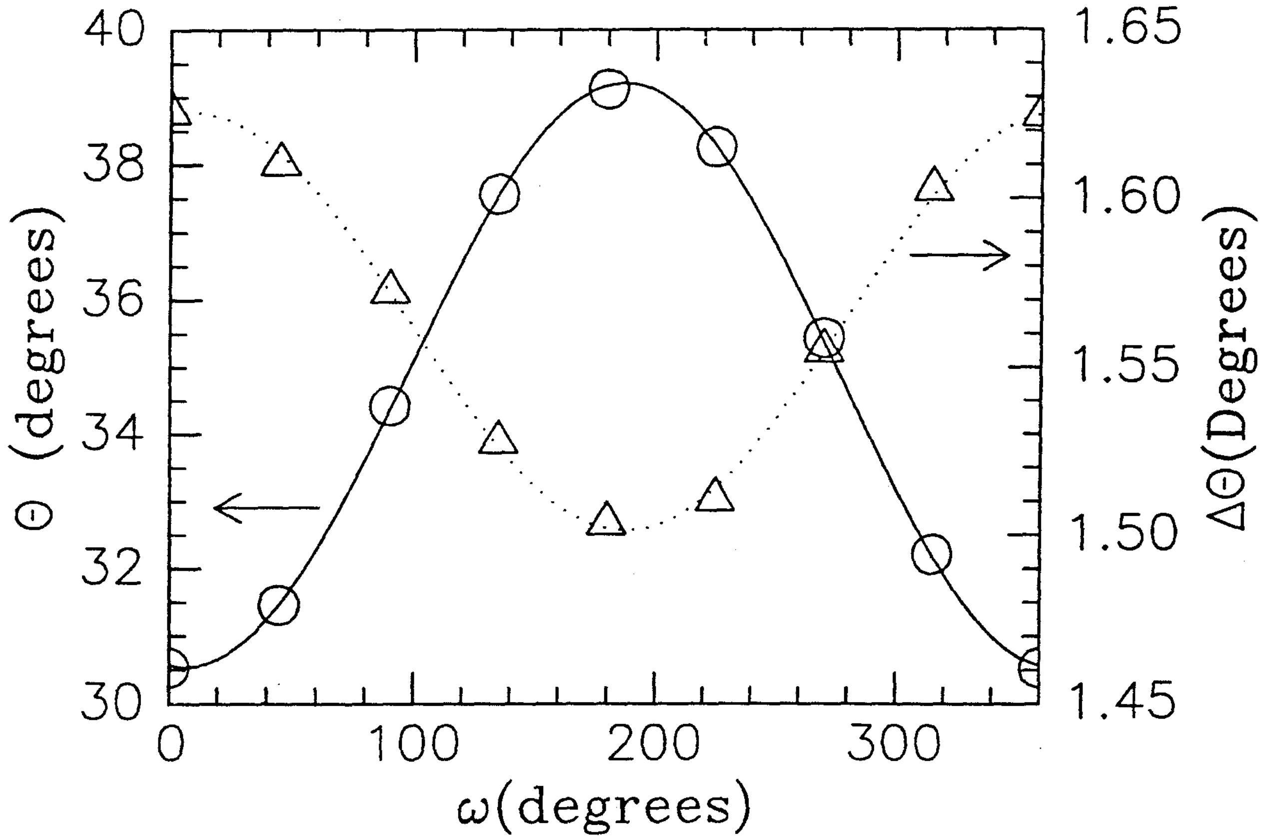

Figure 6.2 The substrate peak position with respect to the surface plane, θ, of a miscut sample ($D10$) and the peak separation, $\Delta\theta$, between the (004) diffraction peak of the Ge film and (004) diffraction peak of the substrate as a function of azimuthal angle, ω. The solid and dotted lines are a fitting of a sine function. Note that the Ge film is tilted toward the Si surface normal.

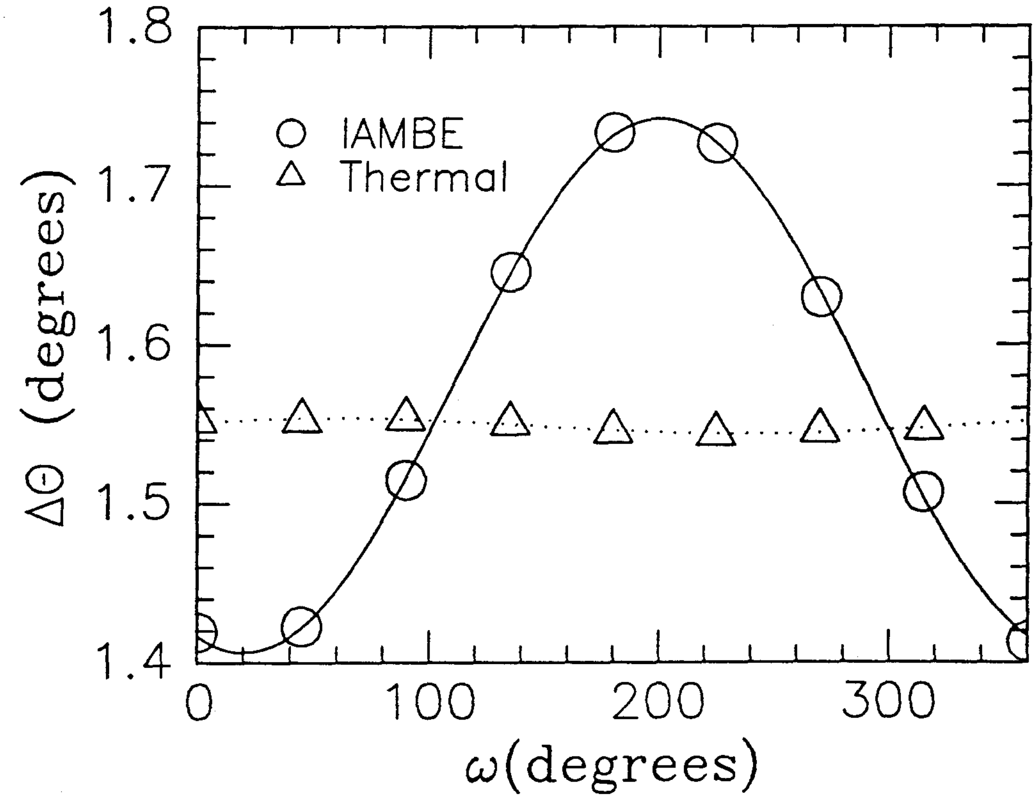

Figure 6.3 The peak separation, $\Delta\theta$ as a function of azimuthal angle for sample ($D19$) which was thermally grown without ion bombardment and sample ($D30$) which was grown at the same condition as the thermally grown one (500°C, 0.1 nm/s) except the first 30 nm was grown with concurrent ion bombardment (200 eV Ar^+, J_i/J_a = 0.15).

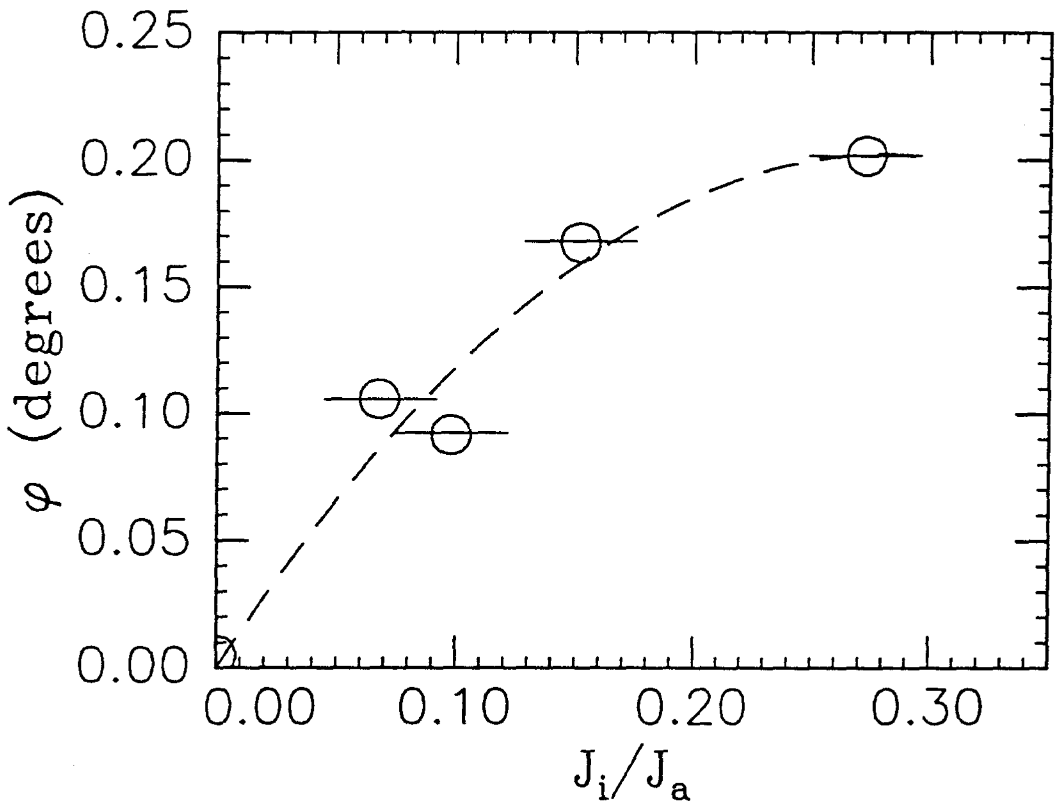

Figure 6.4 The dependence of the misorientation angle on the ion-to-atom flux ratio. The Ge films were grown at 500°C and the first 30 nm of all the films were bombarded with 200 eV Ar^+. The dashed line is a guide to the eyes.

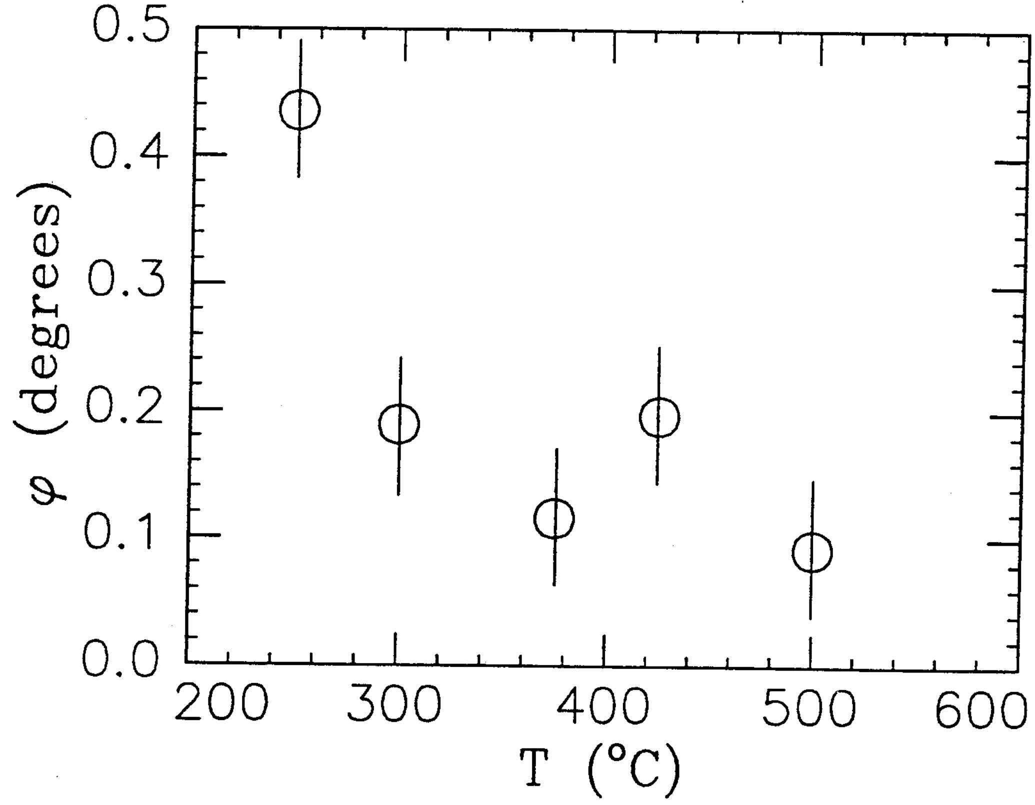

Figure 6.5. The growth temperature dependence of the misorientation. The Ge films were grown at different growth temperature with 200 eV Ar^+ at a fixed ion-atom flux ratio, $J_i/J_a = 0.1$. Error bars indicate the uncertainty introduced by possible variation in J_i/J_a.

6.6. The increase in the FWHM of the diffraction peak of the film suggests an increase of the threading dislocation density of the film. The perpendicular strain in the films relative to the substrate lattice constant increases as growth temperature decreases which indicates a decreasing extent of relaxation. Further annealing of the films at high temperatures (500-800°C) show the films relaxed toward the bulk Ge lattice constant, the FWHM of the film diffraction peaks decrease, and the misorientation of the films does not change significantly. The annealing data are summarized in the Table 6-II.

6.3 Mechanisms for Misorientation Formation by IAMBE

The formation of a misoriented film during growth is thought to be a mechanism for misfit accommodation [4]. Phenomenological models for misorientation formation have proposed that : (i) in a coherent film, the lattice constant in the growth direction of an epitaxial layer matches in the corner of a surface step and increases linearly until reaching its strained value at the edge of the next step [11], (ii) in a relaxed or partially relaxed film, the net Burgers vector perpendicular to the surface of the dislocations is not zero [3, 7], and (iii) for very thick films, the development of macroscopic substrate curvature as film thickness increases is considered to be a factor for misorientation formation [10]. Figure 6.7 shows schematics of the first two models. For a coherent heteroepitaxial system with bulk lattice constants a_s for the substrate and a_f for the film, the lattice constant in the growth direction for the strained films, a_{fs}, is

$$a_{fs} = a_f + \frac{2C_{12}}{C_{11}}(a_f - a_s), \tag{1}$$

where C_{11} and C_{12} are the elastic constants of the films. From Fig. 6.7(a), we can see the misorientation angle, φ, of the film with respect to the growth planes is given by

$$\varphi = (1 + 2\frac{C_{12}}{C_{11}})(a_f - a_s)/L. \tag{2}$$

In the extreme case of misorientation produced by the non-zero Burgers vector perpendicular to the surface, the misfit strain, ϵ, is accommodated by one parallel set

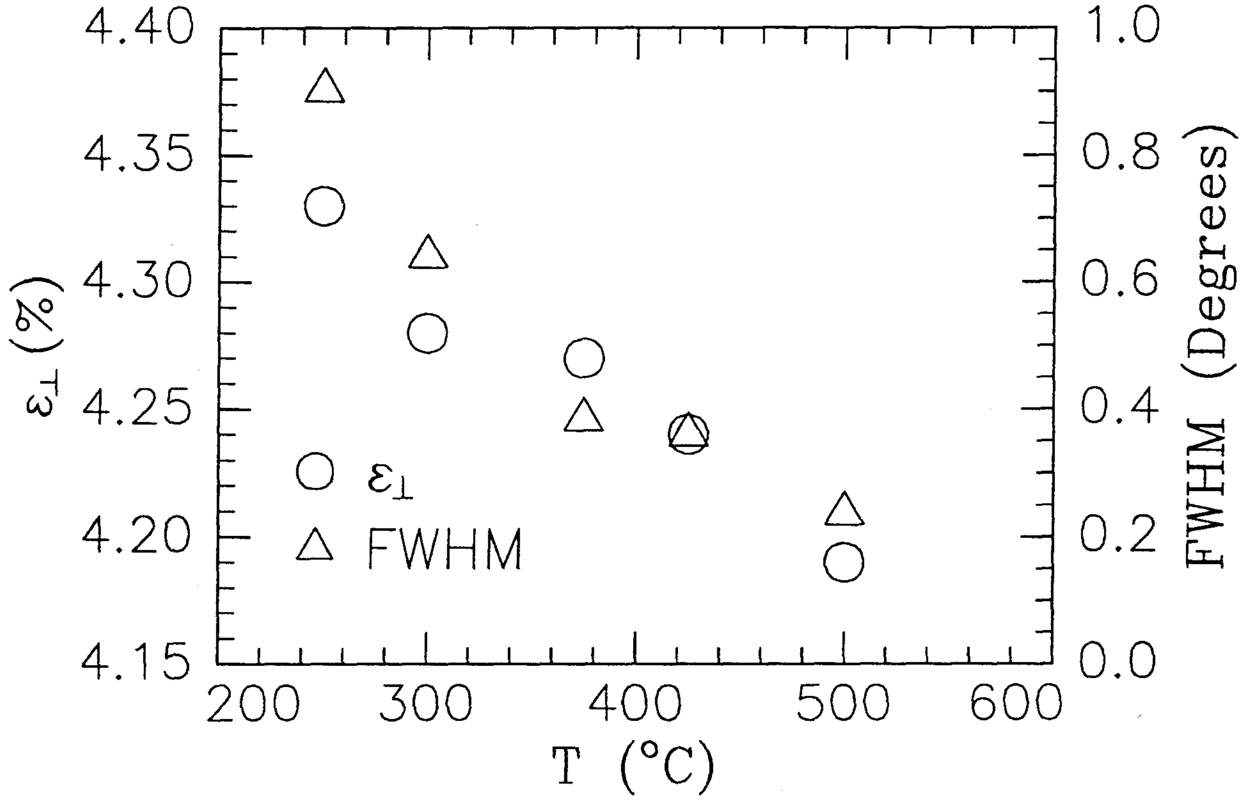

Figure 6.6 The full width at half maximum (FWHM) of the diffraction peaks and the perpendicular strain of the films relative to the substrate lattice constant, $\epsilon_\perp$ as a function of growth temperature. Samples are the same as Fig. 6.5.

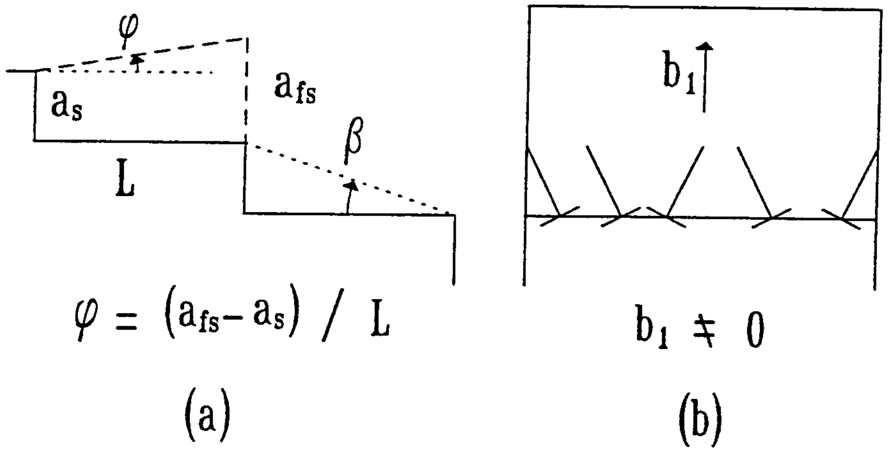

Figure 6.7 (a) model for the misorientation produced by coherent film, a_s is the substrate lattice constant, a_{fs} is the lattice constant in the growth direction for the strained film, and L is the terrace length. (b) model for the misorientation produced by unequal population of two types of dislocations. The net Burgers vector perpendicular to the surface will produce a misorientation between the film and substrate.

of the threading dislocations with Burgers vector component perpendicular to the surface, b_1, and parallel to the surface, b_2. The misorientation can then be expressed as

$$\varphi = b_1/p = \frac{b_1}{b_2}\epsilon, \tag{3}$$

where p is the average spacing between dislocations. Improvements to the geometrical model have been proposed by Beanland and Pond [14]. The model takes into account the parallel strain of the film which is a further extension of the simple model for a coherent film. At the same time, the dependence of the glide forces for different glide systems on a miscut sample is also considered to explain the preferential alignment of the dislocations.

A finite misorientation produced by threading dislocations implies an asymmetric morphology for dislocations. Fox and Jesser [15] have investigated the asymmetric misfit dislocation morphology of $GaAs_{0.95}P_{0.05}$ on GaAs and considered four possible causes, (i) substrate misorientation, (ii) thickness gradient of the epitaxial layer, (iii) different nucleation barriers for the formation of different arrays of dislocations, and (iv) difference Peierls barriers in moving the different arrays of dislocations. The conclusion is that the asymmetric morphology is due to the difference in Peierls barriers between two types of dislocations, (i) the dislocations on 111 Ga planes and (ii) the dislocations on the 111 As planes. It is clear that this conclusion is applicable to compound semiconductors only. Since the Ge films grown in this experiment have thicknesses well above the critical thickness for the dislocation generation, the films are essentially relaxed or at least partially relaxed, which indicates that the possible mechanism for the misorientation formation is also due to the dislocation configuration.

The effect of low energy ion bombardment during molecular beam epitaxial growth can be summarized as following:

1. *The misorientation increases as the buffer Ge film thickness decreases.*
2. *The misorientation increases as IAMBE film thickness increases.*
3. *The misorientation increases as the ion-atom flux ratio increases.*
4. *The misorientation increases as the growth temperature decreases (both IAMBE and thermally grown films).*
5. *The misorientation does not change significantly upon post growth annealing.*

The dependence of the misorientation on the Ge buffer layer thickness indicates that the coherency strain driving force for misorientation is depleted continuously as the Ge buffer layer thickness increases. This point agrees well with the suggestion that the misorientation formation is a misfit strain accommodation mechanism.

As the buffer layer thickness increases, the degrees of relaxation of the Ge films increases. Thus, ion bombardment has a smaller effect on the further increasing of the misorientation angle in thick thermally grown films. It is interesting to see that even after 50-100 nm growth of buffer layer at 300°C, the IAMBE films still have a finite, although small, effect on the misorientation angle of the film.

Hull et al., [17] have investigated the misfit strain relaxation due to keV ion implantation and conclude that upon thermal annealing, the points defects produced by ion implantation increase the nucleation sites for dislocations which enhance the strain relaxation rate. Bulk displacements and surface displacements are two basic effects that are produced by low energy ion beams. The comparison between the behavior of bulk defects as discussed in Chapter 3 and the misorientation shows that growth temperature dependence and ion-to-atom flux ratio dependence have similar trends while the annealing dependence does not. However, the latter does not exclude the possibility of the effect of bulk defects on the misorientation formation, since the bulk displacements can increase the dislocation nucleation sites. Two possible explanations are plausible : (i) the annealing may not have strong effects on the existing dislocations whose mobilities are impeded by the defects, and (ii) the mobile bulk defects can interact to form dislocation loops to enhance the strain relaxation rate [17]. It is important to consider surface defects as well as bulk defects.

In the case of surface defects, Bedrossian et al., [18] have observed reflection high energy electron diffraction (RHEED) oscillations during layer-by-layer sputtering of Si (001) with 200-250 eV Xe^+ ions in temperature range of 350-470°C. At higher substrate temperatures, the RHEED oscillation disappears which indicates that the vacancy-like defects on the surface have high enough mobility to move to the ledges which result in ledge retraction. The ledge is a sink for surface defects (adatom or surface vacancy). From these experiments we can conclude that the concentration of surface defects decrease (being annihilated at the step ledge) as growth temperatures increase. It is obvious that the number of surface defects increases as the ion-atom flux ratio increases. These two trends in fact are correlated with that of the misorientation. Arguments similar to those made for the post-growth annealing independent phenomena for the bulk defects can also be applied to the surface defects, if the surface defects are also postulated to be generation sites for dislocations.

We can estimate the efficiency of enhancing or retarding rate by applying Olsen's model [3] for misorientation formation due to a preferential alignment of dislocations. Assume that the growth direction is (001) and consider two kinds of 60° dislocations, (I) a dislocation with the Burgers vector component perpendicular to the surface on the direction (001), and (II) a dislocation with the Burgers vector component perpendicular to the surface on the direction $(00\bar{1})$. Assume that there are N_I dislocations per unit area in the interface for type I and N_{II} dislocations per unit area in the interface for type II. b_1 is the Burgers vector component perpendicular to the interface and b_2 is the Burgers vector component parallel to the interface. So the net misorientation, φ, can be expressed as

$$\varphi = b_1|N_I - N_{II}| \tag{4}$$

and the strain relieved by threading dislocations is

$$\alpha\epsilon = b_2(N_I + N_{II}), \tag{5}$$

where ϵ is the misfit strain and α is the fraction of misfit strain accommodated by threading dislocations. α is a factor which depends on the dislocation mobility. The relation between misfit strain and misorientation is

$$\frac{\varphi}{\alpha\epsilon} = \frac{b_1|N_I - N_{II}|}{b_2(N_I + N_{II})}. \tag{6}$$

When these two sets of dislocations have an equal number of dislocation, there will be no misorientation between the film and the substrate. For a typical wafer there is always a finite miscut. The sign of $(N_I - N_{II})$ determines the tilting direction toward the substrate normal or away from the substrate normal. For a perfectly cut crystal, which has no step on the surface, a driving force for misorientation does not exist, then there will be no misorientation between film and substrate. Eaglesham and Cerullo [19] have shown that, for Ge films grown at 200°C on Si, 72% of the dislocations are 60° type and accommodate only 16% of the misfit strain. We estimate the component of misorientation angle, φ, enhanced or retarded by low energy ion beam for films grown at 250°C is 0.25°. Hence the fraction of the strain accommodated by the threading dislocations is about 15% of the 4.2% misfit strain ($\alpha = 0.15$). For a 60° type dislocation, b_1/b_2 is approximately 0.707/0.5. Thus the ratio between type I dislocations to type II dislocations is 3. Here we should state that it is difficult to verify the amount of strain accommodated by threading dislocations. We directly quote the value given by Eaglesham and Cerullo [19] without considering the effect of point defects which impede the dislocation motion and lead to a greater percentage of strain accommodated by threading dislocations than that in the thermally grown samples. In this case, the ratio between type I and type II threading dislocations will decrease. In an extreme case, where all of the misfit strain is accommodated by the threading dislocations, i.e., $\alpha = 1$, the ratio of type I to type II dislocations is only 1.16. More threading dislocations in IAMBE films are indicated by the general trend that the larger the misorientation angle the wider the FWHM (not including annealed samples). The cross section transmission electron micrographs for samples listed above show no clearly preferential alignment, which is not surprising when most of the misfit strain is accommodated by the threading dislocations. This clearly suggests that the misorientation angle will increase as the growth temperature decreases which is also a general trend from the above observations. We can also estimate the percentage of strain relaxed by the threading dislocations for thermally grown samples. For samples grown at 500°C ($D19$) and 300°C ($D9$), the misorientation angles are about 0.005° and 0.127° respectively and we assume that the ratio of type I to type II dislocations is 1.16. We will have $\alpha = 2\%$ for sample $D19$ and $\alpha = 52\%$ for sample $D9$. The value for 300°C growth is much higher than the value reported by Eaglesham and Cerullo [19]. The reason is due to the miscut of the wafer, which will enhance the asymmetry of these two types of dislocations [1, 8, 9, 11, 14]. The amplification effects of misorientation by low energy ion bombardment is less important at low growth temperatures, where the dislocations are immobile but will become significant at high growth temperature where the dislocations are mobile.

6.4 Conclusions

Two factors are identified to be responsible for the misorientation formation in a incoherent film-substrate system , (i) the substrate miscut, which produces different glide forces on different sets of dislocations, (ii) the mobilities of the dislocations which determine the relative amount of misfit strain accommodated by the misfit dislocations and threading dislocations, which infer that the misorientation depends on the general parameters that determine the dislocation kinetics in the initial growth stage.

The misorientation angles between films and substrates are also shown to be controllable by low energy ion bombardment during molecular beam epitaxial growth. The effect of low energy (200 eV) ion bombardment at high ion-atom flux ratios (0.05-0.3) shows that the bulk defects play an important role in misorientation formation. The bulk defects in the IAMBE films impede the dislocation motion, which greatly increases the portion of misfit strain accommodated by threading dislocations. It is, however, not completely clear whether the beam-induced surface defects cause the formation of a specific set of threading dislocations to be preferred. The bulk defects along with the finite miscut of the wafer which produce different glide forces for different glide systems is sufficient to explain all the data above, except one sample bombarded with normal incident ion beam which may have almost a 0° miscut. However, the role of bulk defects in misorientation formation is clear and is to amplify the unequal glide forces on different glide systems due to wafer miscut. Further studies of the incident ion angle on the misorientation can further clarify whether the surface defects play an important role in the misorientation formation.

Sample	T (°C)	J_i/J_a	E_i (eV)	t_i (nm)	t_b (nm)	t_T (nm)	Miscut (deg.)	$\epsilon_\perp$ %	φ (deg.)
$D9$	300	0.00	0	0	0	350	≈ 4	4.12	0.1272
$D10$	500	0.00	0	0	0	350	≈ 4	4.16	0.0620
$D19$	500	0.00	0	0	0	250	≤ 0.2	4.13	0.0051
$D4$	300	0.15	200	5	0	350	≈ 4	4.26	0.1494
$D3$	300	0.15	200	10	0	350	≈ 4	4.30	0.2535
$D5$	300	0.15	200	30	0	350	≈ 4	4.04	0.2402
$D8$	300	0.15	200	10	50	350	≈ 4	4.29	0.1840
$D12$	300	0.15	200	10	100	350	≈ 4	4.35	0.1864
$D14$	300	0.15	200	10	0	350	≈ 4	4.16	0.2572
$D13$	300	0.15	200	30	0	350	≈ 4	4.13	0.2285
$D18$	500	0.01	200	30	0	350	≤ 0.2	4.12	0.0916
$D29$	500	0.15	200	30	0	250	≤ 0.2	4.19	0.1675
$D30$	500	0.27	200	30	0	250	≤ 0.2	4.15	0.2016
$D31$	500	0.07	200	30	0	250	≤ 0.2	4.19	0.1058
$D32$	425	0.10	200	30	0	250	≤ 0.2	4.24	0.1966
$D33$	375	0.10	200	30	0	250	≤ 0.2	4.27	0.1159
$D34$	300	0.10	200	30	0	250	≤ 0.2	4.28	0.1893
$D35$	250	0.10	200	30	0	250	≤ 0.2	4.33	0.4356
$D36$	500	0.10	200	30	0	250	≤ 0.2	4.18	0.0049

Table 6-I Sample growth conditions and results. T is the growth temperature, J_i/J_a is the ion-atom flux ratio, E_i is the ion energy, t_i is the thickness of the IAMBE Ge films, t_b is the Ge film thickness grown before IAMBE Ge film, t_T is the total thickness of Ge film include t_i and t_b, 4° miscut represents the angle cut off (001) towards (100), $\epsilon_\perp$ is the perpendicular strain of the films relative to the substrate lattice constant, and φ is the misorientation angle between film (001) axis and substrate (001) axis.

Sample	T_a (°C)	$\epsilon_\perp(\%)$	φ	FWHM
$D19$	500	4.12	0.0051	0.2080
$D19$	600	4.10	0.0049	0.1651
$D19$	700	4.06	0.0056	0.1395
$D19$	800	3.99	0.0060	0.1314
$D31$	500	4.20	0.1063	0.2491
$D31$	600	4.12	0.1050	0.1616
$D31$	800	4.00	0.0937	0.1364
$D33$	500	4.23	0.1003	0.2363
$D33$	600	4.13	0.1184	0.1497
$D33$	700	4.09	0.0906	0.1259
$D33$	800	4.00	0.0754	0.1322
$D34$	500	4.21	0.1970	0.3216
$D34$	600	4.12	0.1954	0.1712
$D34$	700	4.09	0.1873	0.1391
$D34$	800	4.00	0.1778	0.1150
$D35$	500	4.20	0.4072	0.3870
$D35$	600	4.11	0.3847	0.1913
$D35$	700	4.08	0.4423	0.1524
$D35$	800	3.99	0.4262	0.1467

Table 6-II Annealing Data. The X-ray source is Cu-$K_{\alpha 1}$. All measurements are using (004) diffraction of the samples. All annealing times are 30 min. T_a is the annealing temperature, $\epsilon_\perp$ is the perpendicular strain of the films relative to the substrate lattice constant, φ is the misorientation angle between film (001) axis and substrate (001) axis. $\Delta\theta_a$, φ and the full width half maximum (FWHM) are in unit of degrees.

References

[1] H. Nagai, J. Appl. Phys. **45**, 3789 (1974).

[2] P. Maigne and A.P. Roth, Semicond. Sci. Technol. **1**, 1 (1992).

[3] G.H. Olsen and R.T. Smith, Phys. Stat. Sol. **A31**, 739 (1975).

[4] S.K. Ghandhi and J.A. Ayers, Appl. Phys. Lett. **53**, 1024 (1988).

[5] I.B. Bhat, K. Patel, N.R. Taskar, J.E. Ayers, and S.K. Ghandhi, J. Cryst. Growth **88**, 23 (1988).

[6] Y. Kawamura and H. Okamoto, J. Appl. Phys. **50**, 4457 (1979).

[7] G. Bai, Ph.D. thesis, California Institute of Technology (1991).

[8] G. Bai, M.-A. Nicolet, T. Vreeland, Jr., Q. Ye, and K.L. Wang, Appl. Phys. Lett. **55**, 1874 (1989).

[9] G. Bai, D.N. Jamieson, M.-A. Nicolet, and T. Vreeland, Jr., Mat. Res. Soc. Symp. Proc. **102**, 259 (1988).

[10] J. Kleiman, R.M. Park, and H.A. Mar, J. Appl. Phys. **64**, 1201 (1988).

[11] D.A. Neumann, H. Zabel, and H. Morkoc, J. Appl. Phys. **64** 3024 (1988).

[12] A.P. Roth, M.A. Sacilotti, R.A. Masut, D. Morris, J. Young, C. Lacelle, E. Fortin, and J.L. Brebner, Can. J. Phys. **67** 330 (1989).

[13] D.A. Neumann, H. Zabel, and H. Morkoc, Appl. Phys. Lett. **43**, 59 (1983).

[14] R. Beanland and R.C. Pond, Int. Symp. on Struct. Prop. Disloc. Semicond., Oxford, Inst. Phys. Conf. Ser. **104**, 455 (1989).

[15] B.A. Fox and W.A. Jesser, J. Appl. Phys. **68**, 2739 (1990).

[16] B.A. Fox and W.A. Jesser, J. Appl. Phys. **68**, 2801 (1990).

[17] R. Hull, J.C. Bean, J.M. Bonar, G.S. Higashi, K.T. Short, H. Temkin, and A.E. White, Appl. Phys. Lett. **56**, 2445 (1990).

[18] P. Bedrossian, J.E. Houston, J.Y. Tsao, E. Chason, and S.T. Picraux, Phys. Rev. Lett. **67**, 124 (1991).

[19] D.J. Eaglesham and M.Cerullo, Appl. Phys. Lett. **58** 2276 (1991).

Appendix A
Schematic Electrical Connections of the High Resolution X-Ray Diffractometer Built at Caltech

A schematic of the overall system configuration was shown in Chapter 1, Fig. 1.1. The main control unit is a 80286-based IBM-compatible computer. The computer controls 5 DC motors with encoders and one Canon rotary encoder combined with encoder interpolator through two DC8 motor control cards. One stepping motor was controlled by the computer through RS232-COM2 port and the COM1 port was used as I/O for X-ray signals detected by a photomultiplier tube. In the following schematic drawings, the name of each component is included. Figure A.1 shows the overall electrical connections of the system. Figure A.2(a) shows the electrical connections for one of the DC8 motor control cards with extra current amplifier. Figure A.2(b) shows the connections of the Cannon encoder, interpolator, power supply, and DC8 card. Figure A.2(c) shows the connections between the detector and the computer. These four schematics only give an overall ideal of the system connections. For detailed information about the components and connections, see the documentation of the system.

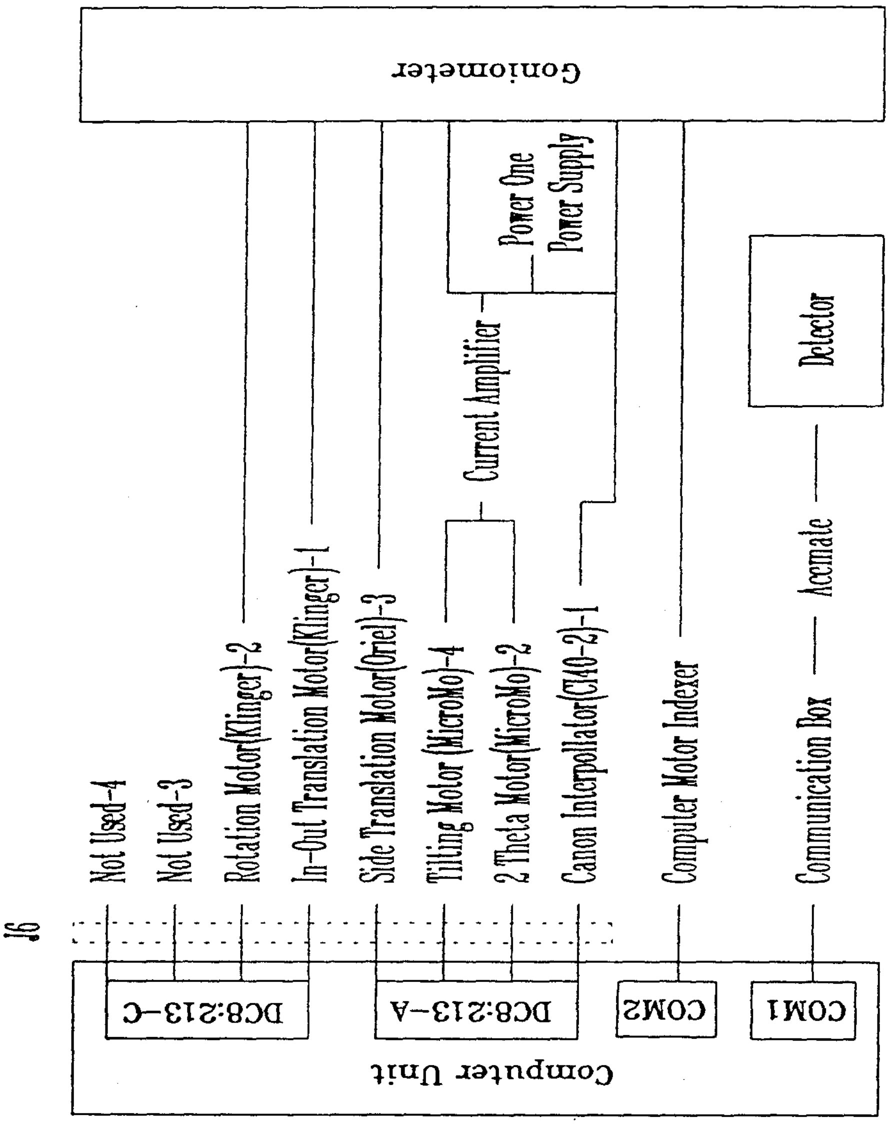

Figure A.1 The overall electrical connections for the high-resolution X-ray diffractometer built at Caltech.

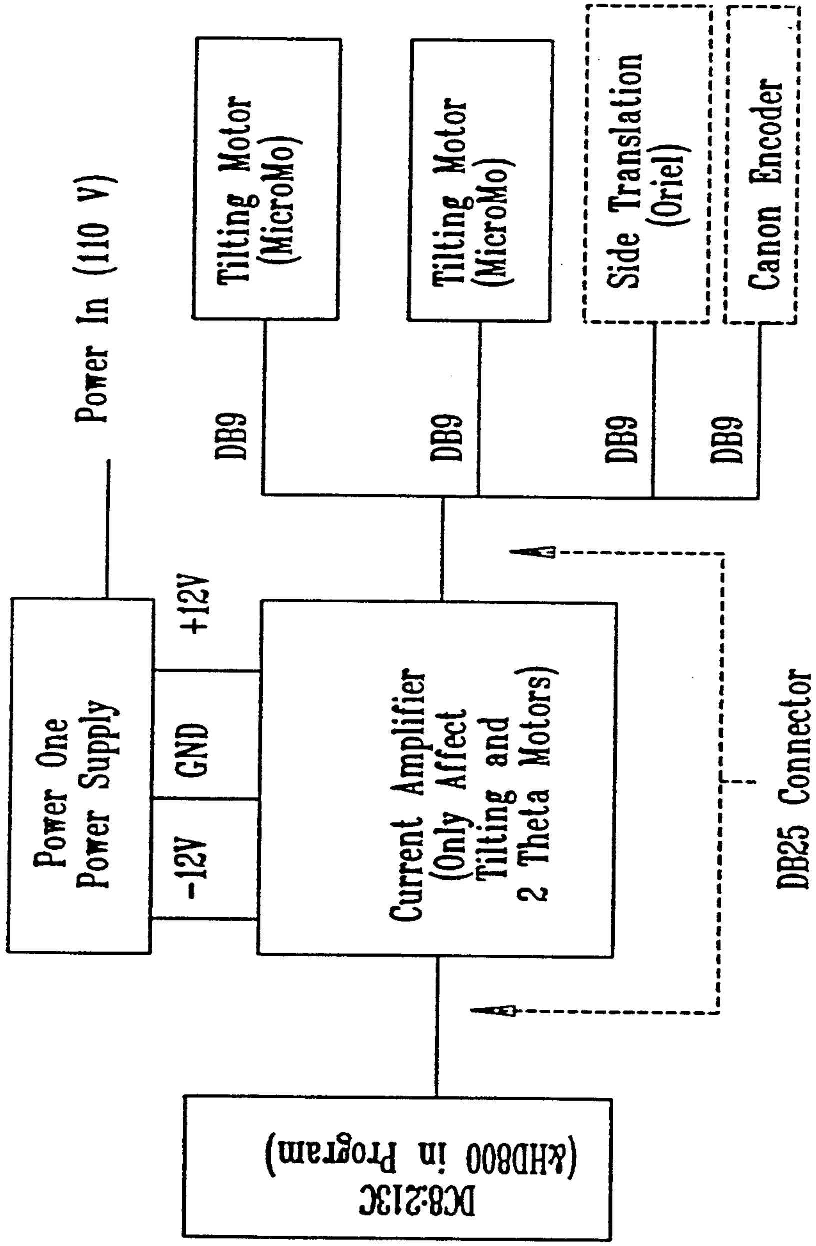

Figure A.2(a) The electrical connections for DC8 motor control card with the extra current amplifier.

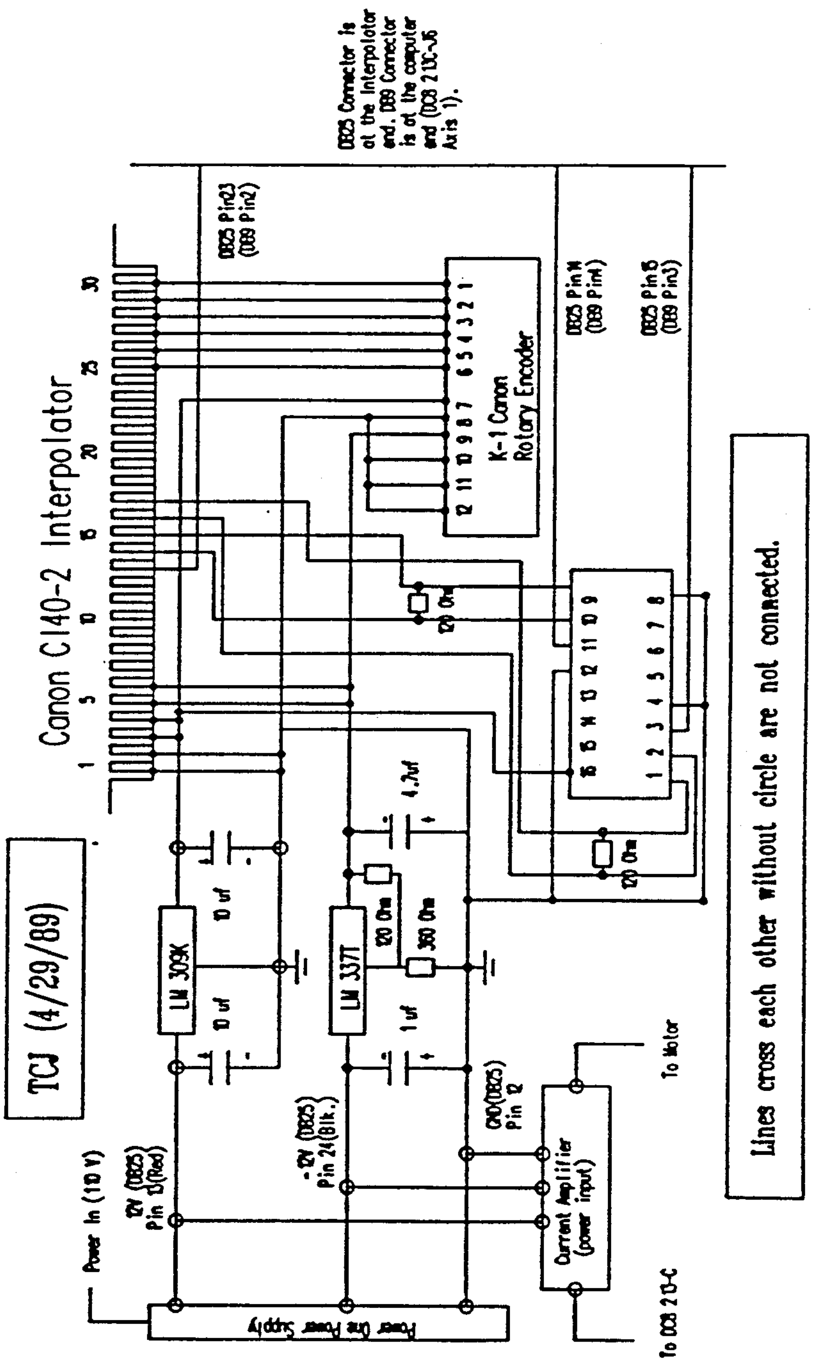

Figure A.2(b) The connections between the Canon encoder, interpolator, DC8 motor control card, and power supply.

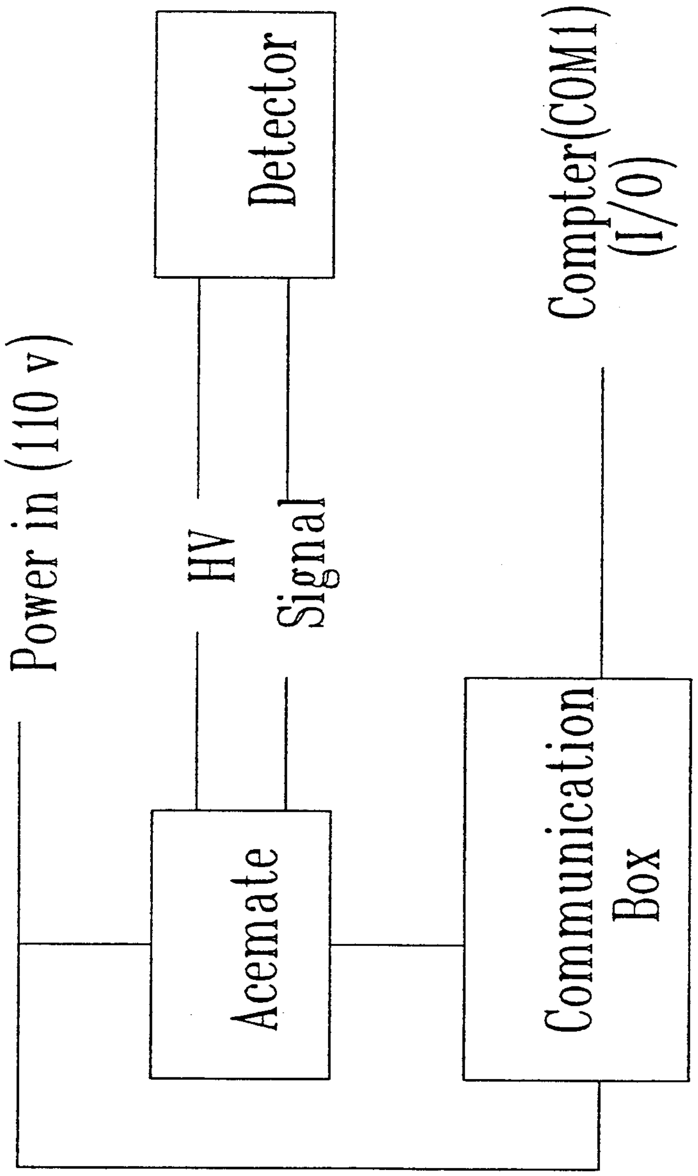

Figure A.2(c) Detector to computer connections.

Appendix B
Si Wafer Cleaning Procedure for Molecular Beam Epitaxy Application

For a Si wafer just obtained from a vender, the following procedure can be used to obtain (2x1) reconstruction pattern on Si (100) surfaces.

- Dip the wafer in 95 H_2O : 5 HF solution for several minutes until the solution does not wet the Si wafer. If this can not be done, you should go through the typical RCA cleaning procedure first.
- Chemically oxidize the Si wafer in 3 H_2O : 1 H_2O_2 : 1 HCl solution at 70-80°C.
- Let the wafer stay in the above solution for 30 s, take the wafer out and dip it into 18 MΩ de-ionized water and then dip the wafer into 95 H_2O : 5 HF solution for a few seconds.
- Repeat the above procedure for 3 or 4 times, during this step, you don't have to change the solutions.
- Leave the wafer in 3 H_2O : 1 H_2O_2 : 1 HCl solution at 70-80°C until the H_2O_2 is not decomposing anymore.
- Take the wafer out and dip it into 18 MΩ de-ionized water while you re-prepare the dilute HF solution again and have the sample holder ready.
- Take the wafer out of the 18 MΩ de-ionized water and dip it into new 95 H_2O : 5 HF solution for 30-60 s. Slowly take the wafer out of the dilute HF solution without any solution droplet on the polished side.
- Make sure the back side of the wafer is also dry by putting the wafer on a lint-free tower.

- Mount the wafer to the sample holder and take it to the load-lock of the system as soon as possible.
- After you successfully transfer the sample holder to the chamber. Turn the heater to about 300°C for at least one hour (pre-bake).
- After pre-baking the wafer, turn the heater further to 550°, the (2x1) reconstruction should show up.

The purpose of the pre-bake is to remove hydrocarbon contamination on the Si surface. The time necessary to remove all of the hydrocarbon contamination is not known for the system in Watson 247. The contamination can be seen from cross-section transmission electron microscopy for a typical 1 hr pre-bake in the system. However, the carbon contamination does not affect the Si buffer layer growth. Thus, for structure studies, proper thickness of Si buffer layer growth is necessary.